Spin Dynamics in Ferroic Materials

Inauguraldissertation

zur

Erlangung der Wünde eines Doktors der Philosophie

vorgelegt der

Philosophisch-Naturwissenschaftlichen Fakultät

der Universität Basel

von

Michele Buzzi

aus Italien

Villigen PSI, 2015

Genehmigt von der Philosophisch-Naturwissenschaftlichen Fakultät

auf Antrag von

Fakultätsverantwortlicher: Prof. Dr. Frithjof Nolting

Korreferent: Prof. Dr. Theo Rasing

Basel, den 23. Juni 2015

Prof. Dr. Jörg Schibler
Dekan

Nature uses only the longest threads to weave her patterns, so that each small piece of her fabric reveals the organization of the entire tapestry

Richard P. Feynman

Contents

Chapter 1

Introduction

In today's world, the so called "smart"-devices are all around us, from the phone tucked in our pocket to the wifi-connected digital camera we carry on travels. These devices are the result of the continuous effort to miniaturise electronic components and to improve their performance. In 1975 Gordon E. Moore predicted that the complexity of the integrated circuits used in commercial devices would double every year since their introduction [1]. As the device functionalities become more complex, the necessity of manipulating and storing information increases.

In the case of long term data storage, information is encoded in a non-volatile change of a material property such as magnetisation in ferromagnetic memories. The discovery in the 1980s of spin transport dependent phenomena and of giant magnetoresistance (GMR) by Albert Fert and Peter Grünberg [2] gave rise to the field of *spintronics* which has had strong impact on magnetic recording. In particular, GMR allowed for the production of extremely sensitive magnetic field sensors that boosted the sensitivity of hard disk recording heads allowing for an increase in the density of the recorded information. Although the current areal density of recorded information in magnetic hard drives has reached 1 Tb/inch^2 (corresponding to a bit size of $25 \times 25\,\mathrm{nm}^2$), the continuously increasing demand for miniaturisation asks for even higher storage densities. However, as the size of the magnetic bit gets smaller one reaches the superparamagnetic limit. Beyond this limit thermal fluctuations have enough energy to cause the magnetisation of the magnetic bit to randomly flip, erasing the recorded information. One way to overcome this problem is to employ materials with stronger coercivity. Although, the higher magnetic anisotropy

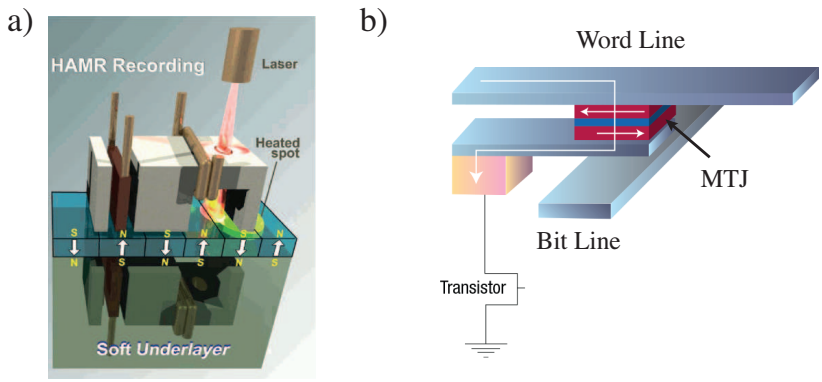

Figure 1.1: (a) Picture showing a writing head for Heat Assisted Magnetic Recording (HAMR) (from Mark Lutwyche of Seagate Research) (b) MRAM cell based on tunnel magnetoresistance. Image adapted from [4]

of these materials allows for stabilising smaller magnetic bits, the increase in coercivity makes it harder to write information as the magnetic field of the current hard disk writing heads is not strong enough. To overcome this problem, a novel solution, known as heat assisted magnetic recording (HAMR) has been proposed [3]. In HAMR, the magnetic write head carries a laser diode that locally heats up the bit to be written in order to temporarily decrease its coercivity. The HAMR recording head is shown in figure figure 1.1a.

Tunnel magnetoresistance (TMR), is a magneto-transport effect that occurs between two ferromagnetic layers separated by an insulator layer which is thin enough for the electrons to tunnel through it [5]. Figure 1.1b shows a typical magnetic random access memory (MRAM) cell based on the TMR effect. When the top and the bottom magnetic layers are magnetised parallel or antiparallel with respect to each other the resistance of the device is, respectively, low or high. The low or high resistance state of the junction corresponds to the "0" or "1" state of the bit. The information in the MRAM cell is typically encoded by letting a strong current through the word line and causing a reorientation of the top magnetic layer. Different methods, such as spin transfer torque, have been proposed but their energy requirements are too high for use in everyday applications [6]. TMR effects up to 1100% have been recently reported [7], making this technology extremely interesting for the development of non volatile memory devices.

It is now clear that in both cases of hard disks and MRAMs the storage of information requires the switching of the magnetisation in a ferromagnetic layer. As the miniaturisation of the magnetic bits progresses, writing information with the use of a magnetic field becomes increasingly problematic both for energy dissipation and for speed reasons. In this context, investigating novel paths to magnetisation switching that combine reliability, speed, and energy efficiency is of primary importance.

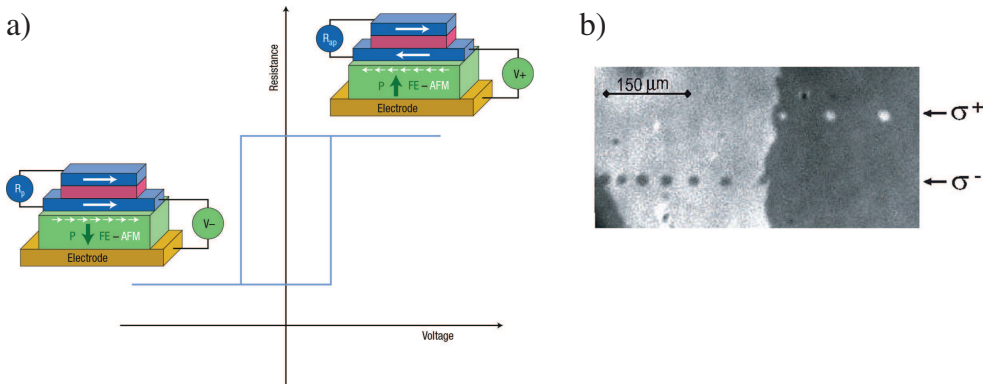

Figure 1.2: (a) Concept of a magnetoelectric MRAM cell. The application of a voltage to the multiferroic layer (green) induces a magnetisation reorientation in the free ferromagnetic layer of the MRAM cell. Adapted from [8]. (b) All optical switching of a GdFeCo layer. 40 fs long circularly polarised laser pulses landed on the sample at different location and caused a local reversal of the magnetisation. Adapted from [9].

In order to drastically lower the power consumption of storage devices, it has been proposed recently that magnetoelectric multiferroic materials, that are both ferromagnetic and ferroelectric, can be employed as constituents of magnetoelectric MRAM cells (see chapter 2 and [8] for more details). Due to the coupling of their electric and magnetic properties the application of an electric field may be used to manipulate directly the magnetisation state of the free layer of a traditional MRAM cell with negligible current consumption (Fig. 1.2a).

Currently, the speed at which information can be processed is significantly higher than the speed at which information can be recorded in magnetic storage devices. Recent experiments have shown that switching by the sole application of ultrashort magnetic field pulses becomes unreliable for pulse durations below 2 ps [10]. Beaurepaire et al. [11] discovered in 1996 that ultrashort laser pulses cause a quenching of the magnetisation of a magnetic material on a sub-ps time scale. This discovery fuelled the interest of researchers in investigating whether ultrafast laser pulses could be employed for magnetisation switching. In 2007, Stanciu et al. [9] discovered that by illuminating a thin layer of $Gd_{22}Fe_{74.6}Co_{3.4}$ with 40-fs circularly polarised laser pulses the magnetisation can be locally reversed as shown in figure 1.2b. The origin of this effect is still debated, but it seems strongly correlated with ultrafast demagnetisation as will be described in chapter 3.

Although much has been achieved in the field of magnetoelectric multiferroics and ultrafast manipulation of magnetisation, much remains to be investigated to exploit the full capability of these discoveries. In this framework, this thesis focused on the following aspects: by using state-of-the-art x-ray magnetic microscopy techniques we have investigated the mechanisms of strain-mediated magnetoelectric coupling at the nanoscale as

well as the effect of lateral confinement on ultrafast magnetisation switching in GdFeCo micro- and nanostructures. Furthermore, we developed and employed a novel experimental technique to ascertain if stochastic contributions are present in ultrafast demagnetisation processes of ferromagnetic thin films. This thesis is organised as follows:

Chapter 2 gives a phenomenological overview on how magnetic properties of matter can be manipulated by the application of electric fields, setting the background for the experiments described in chapter 6. After a phenomenological introduction of the concept of magnetoelectric coupling and single phase multiferroic materials, the concept of artificial multiferroic is presented and the most recent discoveries in this field are discussed.

Chapter 3 discusses how magnetic materials can be modified by the excitation with femtosecond laser pulses, setting the background for the experiments described in chapters 7 and 8. After describing the relevant time scales in magnetism and the interaction mechanisms of ultrashort laser pulses with a magnetic system, the latest investigations in ultrafast magnetism are presented.

Chapter 4 describes the samples and the sample fabrication methods used for the measurements presented in this thesis.

Chapter 5 describes how one can produce high resolution images of magnetic domains using x-ray photoemission electron microscopy and how a commercial photoemission electron microscope has been modified to allow for the application of *in situ* electric fields. This experimental technique has been used for the measurements presented in chapters 6 and 7.

Chapter 6 presents the results of two experiments that explore strain-mediated magnetoelectric coupling in micro- and nanopatterned artificial multiferroics. We give the first experimental proof of a uniform 90° magnetisation rotation in a Ni nanoisland, induced by the application of an electric field. Because the rotation of the magnetisation is complete, the corresponding magnetoelectric coupling coefficient is among the highest measured so far.

Chapter 7 describes the result of an experiment that aimed at observing ultrafast magnetisation switching using a single linearly polarised femtosecond laser pulse in GdFeCo nanostructures.

Chapter 8 presents a novel experimental set-up that makes it possible to perform single-shot time-resolved measurements of an ultrafast process. Using this set-up we were able to probe in a single pump-probe event, the demagnetisation process of a cobalt thin layer, showing for the first time that no stochastic contribution are present in the early time period of ultrafast demagnetisation.

References

[1] G. E. Moore. Cramming more components onto integrated circuits. *Electronics*, 114-117, 1965.

[2] A. Fert. Nobel lecture: Origin, development, and future of spintronics*. *Rev. Mod. Phys.*, 80:1517–1530, 2008.

[3] B. C. Stipe, T. C. Strand, C. C. Poon, H. Balamane, T. D. Boone, J. A. Katine, J.-L. Li, V. Rawat, H. Nemoto, A. Hirotsune, O. Hellwig, R. Ruiz, E. Dobisz, D. S. Kercher, N. Robertson, T. R. Albrecht, and B. D. Terris. Magnetic recording at 1.5 pb m^{-2} using an integrated plasmonic antenna. *Nat. Photon.*, 4(7):484–488, 2010.

[4] C. Chappert, A. Fert, and F. N. Van Dau. The emergence of spin electronics in data storage. *Nat. Mater.*, 6(11):813–823, 2007.

[5] M. Julliere. Tunneling between ferromagnetic films. *Physics Letters A*, 54(3):225 – 226, 1975.

[6] A. D. Kent and D. C. Worledge. A new spin on magnetic memories. *Nat. Nano.*, 10(3): 187–191, 2015.

[7] S. Ikeda, J. Hayakawa, Y. Ashizawa, Y. M. Lee, K. Miura, H. Hasegawa, M. Tsunoda, F. Matsukura, and H. Ohno. Tunnel magnetoresistance of 604diffusion in cofebmgo-cofeb pseudo-spin-valves annealed at high temperature. *Applied Physics Letters*, 93 (8):082508, 2008.

[8] M. Bibes and A. Barthelemy. Multiferroics: Towards a magnetoelectric memory. *Nat. Mater.*, 7(6):425–426, 2008.

[9] C. D. Stanciu, F. Hansteen, A. V. Kimel, A. Kirilyuk, A. Tsukamoto, A. Itoh, and Th. Rasing. All-optical magnetic recording with circularly polarized light. *Phys. Rev. Lett.*, 99: 047601, 2007.

[10] I. Tudosa, C. Stamm, A. B. Kashuba, F. King, H. C. Siegmann, J. Stohr, G. Ju, B. Lu, and D. Weller. The ultimate speed of magnetic switching in granular recording media. *Nature*, 428(6985):831–833, 2004.

[11] E. Beaurepaire, J. C. Merle, A. Daunois, and J. Y. Bigot. Ultrafast spin dynamics in ferromagnetic nickel. *Phys. Rev. Lett.*, 76:4250–4253, 1996.

CHAPTER 2

Manipulating magnetism with electric fields

This chapter gives an overview on how magnetic properties of matter can be manipulated by the application of electric fields, setting a ground for the experiments described in chapter 6. It starts with a short phenomenological introduction on the concept of magnetoelectric coupling and continues with the discussion of how multiferroic materials can potentially show stronger magnetoelectic coupling. This is followed by the introduction of the concept of artificial multiferroic materials in which single ferroic materials can be coupled together to obtain a magnetoelectric coupling[1].

2.1 Magnetoelectric Coupling

Magnetoelectric coupling refers to a cross coupling between electric and magnetic fields in a medium. In 1894, its existence was first predicted by Pierre Curie in materials that simultaneously break time and space reversal symmetry [4]. However it was experimentally discovered only many years later, in Cr_2O_3 [5].

One can describe the free energy of a material as a function of the applied magnetic and electric field as:

[1] This chapter follows from the descriptions given in the following recent reviews: [1, 2, 3]

$$F(\vec{E},\vec{H}) = -\vec{P}_s \cdot \vec{E} - \vec{M}_s \cdot \vec{B} - \frac{\epsilon_0}{2}\sum_{ij}\chi^E_{ij}E_{0i}E_{0j} \tag{2.1}$$

$$-\frac{1}{2\mu_0}\sum_{ij}\chi^M_{ij}B_{0i}B_{0j} - \frac{1}{\mu_0}\sum_{ij}\alpha_{ij}E_{0i}B_{0j} + \cdots$$

where $\vec{P}_s$ and $\vec{M}_s$ are the spontaneous electric and magnetic polarisation, χ^E_{ij} and χ^M_{ij} are the magnetic and electric susceptibilities and α is the linear magnetoelectric coupling. From 2.1 one can derive the magnetic and electrical polarisations:

$$P_i = -\left(\frac{\partial F}{\partial E_i}\right)_B = P_{si} + \epsilon_0\sum_j \chi^E_{ij}E_j + \frac{1}{\mu_0}\sum_j \alpha_{ij}B_j + \cdots \tag{2.2}$$

$$M_i = -\left(\frac{\partial F}{\partial B_i}\right)_E = M_{si} + \mu_0\sum_j \chi^M_{ij}B_j + \frac{1}{\mu_0}\sum_j \alpha_{ij}E_j + \cdots \tag{2.3}$$

This set of equations shows that the magnetoelectric coupling allows one to modulate the magnetic polarisation of a material by applying an electric field as well as modulating its electric polarisation by applying a magnetic field. Materials that show this effect are termed magnetoelectric materials.

Manipulating the magnetisation of a material by the application of an external electric field is a fascinating topic, not only for the potential for applications in producing low power consumption spintronic devices [6] but also on a more fundamental level. Magnetism arises from the spin moment of the electron. Its coupling to the electron charge is typically weak as it originates from a perturbative effect, the spin-orbit coupling. In fact, in most materials the coupling between electric and magnetic properties is weak. In magnetoelectric materials, however, this coupling is found to be significant and the quest for materials showing even stronger coupling led to novel and exciting results such as the improper ferroelectricity in $TbMnO_3$ and flexomagnetoelectric interactions [7, 8].

Cr_2O_3 shows one of the highest coupling coefficients measured so far $\alpha_{zz} = 4.17\,\mathrm{ps\,m^{-1}}$. Yet, the effect of the application of an electric field on the magnetic structure of Cr_2O_3 is modest. From 2.3 it is possible to estimate that flipping one of the spins in the Cr_2O_3 unit cell would require an electric field of the order of $2\times10^3\,\mathrm{GV\,m^{-1}}$, approximately 1000 times stronger than the crystal field [9].

It is possible to demonstrate that in single-phase materials the magnetoelectric coefficient has an upper bound determined by the product of magnetic and electric susceptibilities [10]:

$$\alpha_{ij} \leq \sqrt{\epsilon_0 \mu_0 \chi^m_{ii} \chi^e_{jj}} \tag{2.4}$$

This inequality shows that stronger magnetoelectric couplings may be expected in materials with high dielectric and magnetic susceptibilities such as those that show a coexistence of a long range electric and magnetic order. This result has stimulated researchers to synthesise and characterise new materials that are at the same time ferromagnetic and ferroelectric. These materials are known as magnetoelectric multiferroics as described in the following.

2.2 Multiferroics and Magnetoelectric Materials

2.2.1 Ferroic Materials and Ferroic Orders

A ferroic material is a material that possesses a long range order of a certain microscopic property giving rise to a spontaneous macroscopic property, also identified as order parameter. Being able to induce changes in the order parameter by the application of one or more external fields is a necessary requirements for a ferroic material. Up to now four ferroic orders are known: ferromagnetism, ferroelectricity, ferroelasticity[2] and ferrotoroidicity. Each of these order is related to a symmetry breaking as summarised in table 2.1. This thesis focuses on ferroelectricity and ferromagnetism; more details about the other mentioned ferroic orders can be found in [11, 12].

Ferroic Order	Order Parameter	Space Invariant	Time Invariant
Ferroelasticity	Strain	Yes	Yes
Ferroelectricity	Polarisation	No	Yes
Ferromagnetism	Magnetisation	Yes	No
Ferrotoroidicity	Toroidal Moment	No	No

Table 2.1: Ferroic orders and symmetry breaking.

Ferromagnetic materials are characterised by the presence of a spontaneous magnetisation that can be switched by an applied magnetic field. The magnetisation must be stable and the switching process follows a hysteresis curve. The same type of long range order is present in antiferromagnetic materials where the magnetic moments are aligned antiparallel to each other and cancel completely within the magnetic unit cell.

Ferroelectric materials show a spontaneous electrical polarisation that can be switched by the application of an external electric field. The switching happens between two stable polarisation states and follows a hysteresis curve.

[2]The presence of a spontaneous stress arises by a change in the crystal symmetry, i.e. a symmetry breaking is present despite the material being time and space invariant

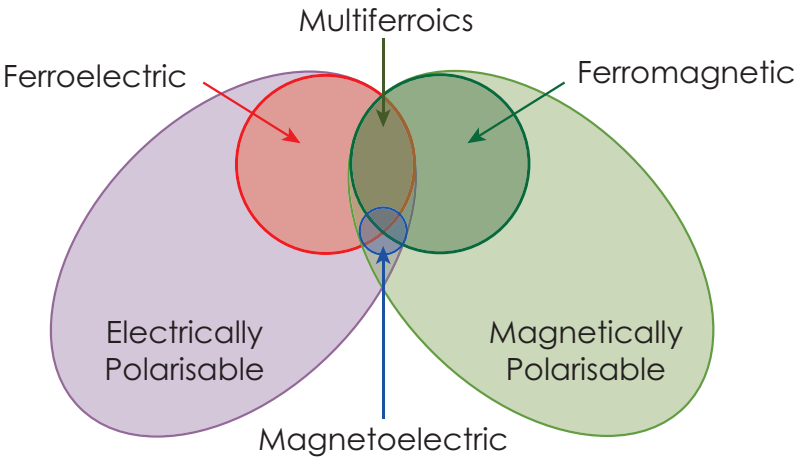

Figure 2.1: Relationship between magnetoelectric materials and multiferroics. Adapted from [2]

Ferrimagnetic materials, similarly to antiferromagnets, show an antiparallel alignment of the magnetic moments in the magnetic unit cell. However, in ferrimagnets, the opposing magnetic moments have different magnitude or their alignment is not perfectly collinear, generating a net magnetisation that can be switched by the application of an external magnetic field as in the case of a ferromagnet.

2.2.2 Multiferroics and Magnetoelectric Materials

One generally identifies a material as multiferroic if it shows the coexistence of multiple ferroic orders in one single phase. In a multiferroic, the ferroic orders may or may not be coupled, meaning that their coexistence is not a sufficient condition for the presence of a coupling between the order parameters. In the following the term multiferroic will be used to indicate materials which are both ferroelectric and ferromagnetic.

Figure 2.1 clarifies the relationship between ferromagnetic, ferroelectric, magnetoelectric and multiferroic materials. Ferromagnets and ferroelectrics are a subset of the magnetically and electrically polarisable materials respectively. Magnetically polarisable materials also comprises antiferromagnets and paramagnets. Similarly, paraelectrics are also classified as electrically polarisable materials. Magnetoelectric coupling is likely to happen when the material is both electrically and magnetically polarisable (blue set). Materials that belong to the blue set and simultaneously show ferromagnetism or ferroelectricity are identified as magnetoelectric multiferroic.

The known number of single phase magnetoelectric multiferroics is relatively small, as a consequence of the fact that the requirements for the existence of ferroelectricity and ferromagnetism in oxides are almost mutually exclusive [13]. For example, in ABO_3 per-

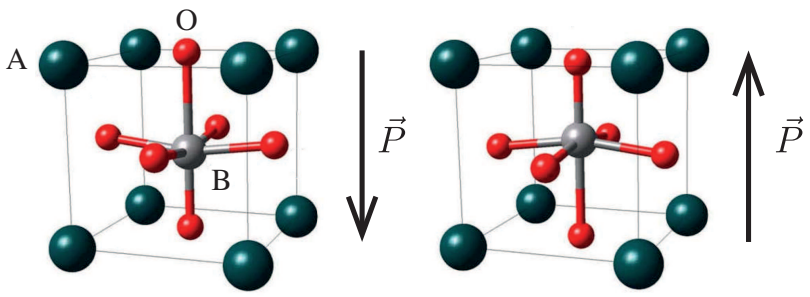

Figure 2.2: Dipole moment in a ABO_3 perovskite. Adapted from [14]

ovskites, the development of a strong spontaneous dipole moment is related to the displacement of the B cation from its central position in the BO_6 oxygen cage (Fig. 2.2). This distortion is stabilised by the hybridisation of the lowest unoccupied 3d levels of the B cation with the oxygen 2p levels which is favoured when the B cation is in a d^0 state. This condition is clearly in contrast with the presence of magnetism that requires partially filled d-orbitals.

In most known multiferroics, ferroelectricity coexists with antiferromagnetism and ferrimagnetism as in the case of bismuth ferrite or the rare earth manganites [15, 16]. $BiFeO_3$ is one of the most intensively studied single phase multiferroics. It is a ferroelectric antiferromagnet with a Néel temperature $T_N \approx 640$K and a ferroelectric Curie temperature $T_C \approx 1100$K. It has one of the highest spontaneous electrical polarisations measured so far $P_s \approx 130\,\mu C\,cm^{-2}$ [17], and a complex magnetic structure that is at the origin of a residual magnetic moment. Despite this, it has a relatively small magnetoelectric coupling coefficient [18]. More details about single phase multiferroics can be found in [1, 19, 20].

2.3 Artificial Multiferroics

Multiferroicity and magnetoelectric coupling can also be achieved artificially, for example, by tailoring the interface between two different constituent materials, typically a ferroelectric and a ferromagnet in such a way as to induce a coupling between the two order parameters. The focus of research is moved from tailoring the material structure to favour the coexistence of ferroelectricity and ferromagnetism (as in the case of single phase multiferroics), to tailoring the interface between two constituent materials to achieve a strong magnetoelectric coupling. So far, three interfacial coupling mechanisms between the individual components have been exploited to induce a magnetoelectric coupling in composite material: strain, exchange, and charge coupling. A detailed explanation of the mechanisms is given in the following[3].

[3]This section follows from the descriptions given in the following recent reviews: [21, 22]

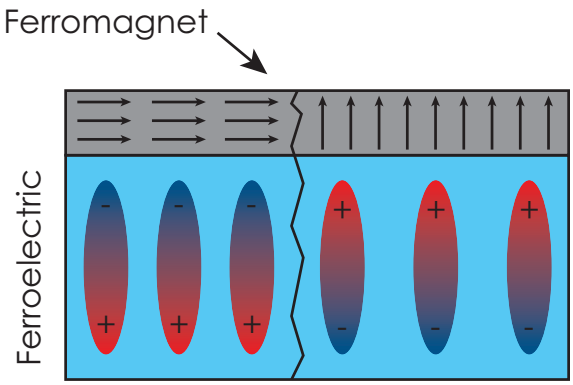

Figure 2.3: Sketch of a strain coupled artificial multiferroic in which structural distortions generated by the ferroelectric cause a modification in the magnetic anisotropy of the ferromagnetic layer. Adapted from [22].

2.3.1 Strain Mediated Artificial Multiferroics

Strain-coupled artificial multiferroics are typically realised by interfacing a magnetostrictive ferromagnetic layer and a ferroelectric with high converse piezoelectric activity as shown in figure 2.3. In ferromagnets, the magnetoelastic effect creates an additional contribution to the magnetic anisotropy, which is proportional to the deformation to which the ferromagnet is subjected to. When the ferromagnet is elastically coupled to the ferroelectric, deformations can be induced in the ferromagnet by applying an electric field to the ferroelectric via the converse piezoelectric effect. As a result, the magnetic properties of the ferromagnet are manipulated by the application of an electric field.

Strain-mediated magnetoelectric coupling has been investigated and optimised since the 1970s. However, in absence of a good control over the interfaces, the elastic couplings were poor and the magnetoelectric coupling values at frequencies far from mechanical resonances were low. Recently, advances in sample growth techniques have allowed the synthesis of artificial multiferroics with optimal elastic coupling between the constituent phases such as magnetostrictive nanopillars in a ferroelectric matrix [23] or thin ferromagnetic layers deposited directly on ferroelectric crystals [24, 25]. In this context, the experiments described in chapter 6 show how strain mediated magnetoelectric coupling can be exploited to obtain a non-volatile control of the magnetic configuration in Ni nanodots, leading to one of the highest magnetoelectric coupling coefficients measured so far.

Complex oxides can also be employed as ferromagnetic constituents. In this case the piezoelectric strain can induce more dramatic changes involving the atomic and electronic structures as observed in different studies involving $La_{0.3}Sr_{0.7}MnO_3$ [26], $La_{0.3}Ca_{0.7}MnO_3$ [27] and $Pr_{0.4}Ca_{0.6}MnO_3$ [28]. For a more comprehensive overview see

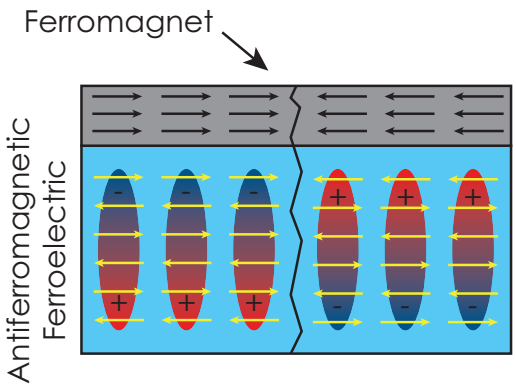

Figure 2.4: Sketch of an exchange coupled artificial multiferroic in which a single-phase multiferroic and a soft ferromagnetic layer are coupled together. The exchange interaction at the interface is used as a mechanism to modify the magnetic properties of the latter and generate a magnetoelectric coupling. Adapted from [22].

[21].

Recently, it has been proposed that strain pulses can induce 180° magnetisation reorientations [29]. However, the strain threshold needed to induce stable magnetic reorientations is above 0.1%, even in the case of sub-100 nm structures. Thus, it is still an open question whether such large strain pulses can be compatible with the high reliability required for the application in MRAM cells.

2.3.2 Exchange Mediated Artificial Multiferroics

Exchange-coupled artificial multiferroics are typically realised by coupling a soft ferromagnetic layer (CoFe, NiFe) and an antiferromagnetic multiferroic ($BiFeO_3$, $LuMnO_3$, $YMnO_3$) as shown in figure 2.4. The interaction of a ferromagnetic layer with an antiferromagnet has been extensively studied since the discovery of exchange-bias in 1956 [30]. Exchange-bias arises from the pinned uncompensated magnetic moments at the interface between the ferromagnetic layer and the antiferromagnet. Their effect is to create a unidirectional anisotropy (exchange anisotropy) that causes a shift in the hysteresis curve of the ferromagnet. The direction of the shift can be defined by applying a magnetic field in a certain direction while cooling the system through the Néel temperature. For a more detailed review on exchange-bias see for example [31].

In antiferromagnetic ferroelectrics, as for example in $BiFeO_3$ and rare earth manganites, the antiferromagnetic order can be manipulated directly by the application of an external electric field, causing a reorientation of the antiferromagnetic vector or the switching of antiferromagnetic domains [32, 33]. This allows for the modification of the exchange-bias direction by the application of an electric field without the need of

temperature cycling. Interfaces based on $BiFeO_3$, rare earth manganites, such as $LuMnO_3$ and $YMnO_3$, and magnetoelectric materials such as Cr_2O_3 have been investigated leading to important results [34, 35, 36, 37].

In the context of electric field induced magnetisation reorientations in magnetic nanostructures, the interface CoFe / $BiFeO_3$ has been extensively investigated. Thanks to its canted antiferromagnetic magnetic structure, $BiFeO_3$ has a residual net magnetic moment that can couple directly to the magnetisation of the CoFe islands. By carefully tailoring the $BiFeO_3$ ferroelectric domain structure, a reproducible electric field induced switching of its antiferromagnetic domain structure was achieved. As a consequence, the application of electric fields induced a deterministic 180° switching of the exchange coupled CoFe magnetic element [38].

Finally, it is important to note that while different models have been formulated to explain the details of exchange mediated magnetoelectric coupling, the ultimate understanding of the details of the effect is still matter of intense research. For more details see [39].

2.3.3 Charge Mediated Artificial Multiferroics

Charge-coupled artificial multiferroics are typically realised by coupling a ferromagnetic layer and ferroelectrics with polarisation perpendicular to the interface plane as shown in figure 2.5. In charge mediated artificial multiferroics, the bound charge at the ferroelectric interface modulates the charge carrier density in the ferromagnetic layer through charge screening. The geometry of the structure is analogous to field effect devices using ferroelectric dielectrics and allows for large modulations in the charge carrier density at the interface [40]. Such modulations can be employed to generate important modifications in every electronic-driven phenomenon in solid state such as transport, magnetism and orbital ordering.

Modifications of the charge carrier density in ferromagnetic metals normally cause a shift in the Fermi energy. This is responsible for a change in the spin imbalance of the system leading to a direct change in the saturation magnetisation of the ferromagnetic layer [41]. The occupation of 3d orbitals can also be affected by differences in the charge carrier density, leading to changes in the magnetic anisotropy of the material via spin-orbit coupling [41, 42]. Recently, investigations of interfaces involving 3d metals on ferroelectrics have confirmed theoretical predictions and demonstrated sizeable changes in magnetic anisotropy with the application of external electric fields [43, 44].

More radical changes can be expected when the ferromagnetic constituent is a mixed valence complex oxide, such as $La_{1-x}Sr_xMnO_3$ (LSMO). Typically, mixed valence complex oxides show a rich phase diagram as a function of chemical doping with the presence of competing ground states [45]. Ferroelectric field effects can be employed to alter

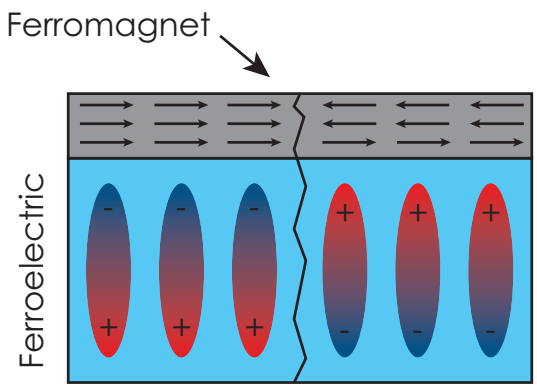

Figure 2.5: Sketch of an charge coupled artificial multiferroic in which the screening of the ferroelectric polarisation at the interface induces a charge accumulation/depletion at the interface that affects the magnetic interactions in the ferromagnet. Adapted from [22].

the charge doping of the ferromagnetic oxide layer and drive it through the boundary separating two different ground states. Recent investigations on LSMO / $PbZr_{0.2}Ti_{0.8}O_3$ have demonstrated that the magnetic ground state of the interfacial manganite layer can be altered from ferromagnetic in the charge depletion state to antiferromagnetic in the charge accumulation state [46].

As the charge mediated effect is related to the accumulation of charge at the interface between the ferromagnet and the ferroelectric, charge mediated magnetoelectric coupling is a strictly interfacial effect limited by the Thomas-Fermi screening length in the ferromagnetic constituent, which varies, depending on the material, from few angstroms to ≈1 nm. While very strong magnetoelectric coupling coefficients can be obtained for ultrathin films, it is still under debate how this coupling mechanism can be extended to thicker films as required in data storage applications.

In this chapter I discussed the possibility of manipulating magnetisation with the application of external electric fields, setting the background for the experiments presented in chapter 6. In the next chapter I will address the possibility of manipulating magnetisation at an ultrafast pace using ultrashort laser pulses.

References

[1] M. Fiebig. Revival of the magnetoelectric effect. *Journal of Physics D: Applied Physics*, 38(8):R123, 2005.

[2] W. Eerenstein, N. D. Mathur, and J. F. Scott. Multiferroic and magnetoelectric materials. *Nature*, 442(7104):759–765, 2006.

[3] C. A. F. Vaz, J. Hoffman, C. H. Ahn, and R. Ramesh. Magnetoelectric coupling effects in multiferroic complex oxide composite structures. *Advanced Materials*, 22(26-27): 2900–2918, 2010.

[4] P. Curie. Sur la symétrie dans les phénomènes physiques, symétrie d'un champ électrique et d'un champ magnétique. *J. Phys. Theor. Appl.*, 3:393–415, 1894.

[5] D. N. Astrov. Magnetoelectric effect in chromium oxide. *Journal of Experimental and Theoretical Physics*, 13(4):729, 1961.

[6] M. Bibes and A. Barthelemy. Multiferroics: Towards a magnetoelectric memory. *Nat. Mater.*, 7(6):425–426, 2008.

[7] T. Kimura, T. Goto, H. Shintani, K. Ishizaka, T. Arima, and Y. Tokura. Magnetic control of ferroelectric polarization. *Nature*, 426(6962):55–58, 2003.

[8] A. P. Pyatakov and A. K. Zvezdin. Flexomagnetoelectric interaction in multiferroics. *The European Physical Journal B*, 71(3):419–427, 2009.

[9] T. H. O'Dell. *The Electrodynamics of Magneto-Electric Media*. North-Holland Publishing Company, 1970.

[10] W. F. Brown, R. M. Hornreich, and S. Shtrikman. Upper bound on the magnetoelectric susceptibility. *Phys. Rev.*, 168:574–577, 1968.

[11] E. K. H. Salje. Ferroelastic materials. *Annual Revew of Materials Research*, 42:265–283, 2012.

[12] B. B. Van Aken, J.-P. Rivera, H. Schmid, and M. Fiebig. Observation of ferrotoroidic domains. *Nature*, 449(7163):702–705, 2007.

[13] N. A. Hill. Why are there so few magnetic ferroelectrics? *The Journal of Physical Chemistry B*, 104(29):6694–6709, 2000.

[14] Materials Design. Ferroelectric properties of $BaTiO_3$. Application Note.

[15] G. Catalan and J. F. Scott. Physics and applications of bismuth ferrite. *Advanced Materials*, 21(24):2463–2485, 2009.

[16] L. Bernd. Hexagonal manganites – $RMnO_3$: Class i multiferroics with strong coupling of magnetism and ferroelectricity. *ISRN Condensed Matter Physics*, 2013:43, 2013.

[17] J. X. Zhang, Q. He, M. Trassin, W. Luo, D. Yi, M. D. Rossell, P. Yu, L. You, C. H. Wang, C. Y. Kuo, J. T. Heron, Z. Hu, R. J. Zeches, H. J. Lin, A. Tanaka, C. T. Chen, L. H. Tjeng, Y.-H. Chu, and R. Ramesh. Microscopic origin of the giant ferroelectric polarization in tetragonal-like $bifeo_3$. *Phys. Rev. Lett.*, 107:147602, 2011.

[18] M. Tokunaga, M. Azuma, and Y. Shimakawa. High-field study of strong magnetoelectric coupling in single-domain crystals of $BiFeO_3$. *Journal of the Physical Society of Japan*, 79(6):064713, 2010.

[19] W. Prellier, M. P. Singh, and P. Murugavel. The single-phase multiferroic oxides: from bulk to thin film. *Journal of Physics: Condensed Matter*, 17(30):R803, 2005.

[20] G. Lawes and G. Srinivasan. Introduction to magnetoelectric coupling and multiferroic films. *Journal of Physics D: Applied Physics*, 44(24):243001, 2011.

[21] C. A. F. Vaz. Electric field control of magnetism in multiferroic heterostructures. *Journal of Physics: Condensed Matter*, 24(33):333201, 2012.

[22] C. A. F. Vaz and U. Staub. Artificial multiferroic heterostructures. *J. Mater. Chem. C*, 1 (6731), 2013.

[23] H. Zheng, J. Wang, S. E. Lofland, Z. Ma, L. Mohaddes-Ardabili, T. Zhao, L. Salamanca-Riba, S. R. Shinde, S. B. Ogale, F. Bai, D. Viehland, Y. Jia, D. G. Schlom, M. Wuttig, A. Roytburd, and R. Ramesh. Multiferroic $BaTiO_3$-$CoFe_2O_4$ nanostructures. *Science*, 303(5658):661–663, 2004.

[24] T. Nan, Z. Zhou, M. Liu, X. Yang, Y. Gao, B. A. Assaf, H. Lin, S. Velu, X. Wang, H. Luo, J. Chen, S. Akhtar, E. Hu, R. Rajiv, K. Krishnan, S. Sreedhar, D. Heiman, B. M. Howe, G. J. Brown, and N. X. Sun. Quantification of strain and charge co-mediated magnetoelectric coupling on ultra-thin Permalloy/PMN-PT interface. *Sci. Rep.*, 4(3688), 2014.

[25] C. Zhang, F. Wang, C. Dong, C. Gao, C. Jia, C. Jiang, and D. Xue. Electric field mediated non-volatile tuning magnetism at the single-crystalline Fe/PMN−PT interface. *Nanoscale*, 7:4187–4192, 2015.

[26] J. Heidler, C. Piamonteze, R. V. Chopdekar, M. A. Uribe-Laverde, A. Alberca, M. Buzzi, A. Uldry, B. Delley, C. Bernhard, and F. Nolting. Manipulating magnetism in $La_{0.7}Sr_{0.3}MnO_3$ via piezostrain. *Phys. Rev. B*, 91:024406, 2015.

[27] A. Alberca, N. M. Nemes, F. J. Mompean, N. Biskup, A. de Andres, C. Munuera, J. Tornos, C. Leon, A. Hernando, P. Ferrer, G. R. Castro, J. Santamaria, and M. Garcia-Hernandez. Exotic magnetic anisotropy map in epitaxial $La_{0.7}Ca_{0.3}MnO_3$ films on $BaTiO_3$. *Phys. Rev. B*, 84:134402, 2011.

[28] Q. X. Zhu, W. Wang, S. W. Yang, X. M. Li, Y. Wang, H.-U. Habermeier, H. S. Luo, H. L. W. Chan, X. G. Li, and R. K. Zheng. Coaction and competition between the ferroelectric field effect and the strain effect in $Pr_{0.5}Ca_{0.5}MnO_3$ film / PMN-PT crystal heterostructures. *Applied Physics Letters*, 101(17):172906, 2012.

[29] J. J. Wang, J. M. Hu, J. Ma, J. X. Zhang, L. Q. Chen, and C. W. Nan. Full 180° magnetization reversal with electric fields. *Sci. Rep.*, 4(7507), 2014.

[30] W. H. Meiklejohn and C. P. Bean. New magnetic anisotropy. *Phys. Rev.*, 102:1413–1414, 1956.

[31] J. Nogués and I. K. Schuller. Exchange bias. *Journal of Magnetism and Magnetic Materials*, 192(2):203–232, 1999.

[32] T. Zhao, A. Scholl, F. Zavaliche, K. Lee, M. Barry, A. Doran, M. P. Cruz, Y. H. Chu, C. Ederer, N. A. Spaldin, R. R. Das, D. M. Kim, S. H. Baek, C. B. Eom, and R. Ramesh. Electrical control of antiferromagnetic domains in multiferroic $BiFeO_3$ films at room temperature. *Nat. Mater.*, 5(10):823–829, 2006.

[33] P. G. Radaelli, L. C. Chapon, A. Daoud-Aladine, C. Vecchini, P. J. Brown, T. Chatterji, S. Park, and S-W. Cheong. Electric field switching of antiferromagnetic domains in YMn_2O_5: A probe of the multiferroic mechanism. *Phys. Rev. Lett.*, 101:067205, 2008.

[34] L. W. Martin, Y.-H. Chu, M. B. Holcomb, M. Huijben, P. Yu, S.-J. Han, D. Lee, S. X. Wang, and R. Ramesh. Nanoscale control of exchange bias with bifeo3 thin films. *Nano Letters*, 8(7):2050–2055, 2008.

[35] V. Skumryev, V. Laukhin, I. Fina, X. Martí, F. Sánchez, M. Gospodinov, and J. Fontcuberta. Magnetization reversal by electric-field decoupling of magnetic and ferroelectric domain walls in multiferroic-based heterostructures. *Phys. Rev. Lett.*, 106:057206, 2011.

[36] S.-H. Lim, M. Murakami, S.E. Lofland, A.J. Zambano, L.G. Salamanca-Riba, and I. Takeuchi. Exchange bias in thin-film $(Co/Pt)_3$ / Cr_2O_3 multilayers. *Journal of Magnetism and Magnetic Materials*, 321(13):1955 – 1958, 2009.

[37] V. Laukhin, V. Skumryev, X. Martí, D. Hrabovsky, F. Sánchez, M. V. Garc´-Cuenca, C. Ferrater, M. Varela, U. Lüders, J. F. Bobo, and J. Fontcuberta. Electric-field control of exchange bias in multiferroic epitaxial heterostructures. *Phys. Rev. Lett.*, 97: 227201, 2006.

[38] J. T. Heron, J. L. Bosse, Q. He, Y. Gao, M. Trassin, L. Ye, J. D. Clarkson, C. Wang, Jian Liu, S. Salahuddin, D. C. Ralph, D. G. Schlom, J. Iniguez, B. D. Huey, and R. Ramesh. Deterministic switching of ferromagnetism at room temperature using an electric field. *Nature*, 516(7531):370–373, 2014.

[39] V. Garcia, M. Bibes, and A. Barthélémy. Artificial multiferroic heterostructures for an electric control of magnetic properties. *Comptes Rendus Physique*, 16(2):168 – 181, 2015.

[40] J. Hoffman, X. Pan, J. W. Reiner, F. J. Walker, J. P. Han, C. H. Ahn, and T. P. Ma. Ferroelectric field effect transistors for memory applications. *Advanced Materials*, 22(26-27): 2957–2961, 2010.

[41] C.-G. Duan, J. P. Velev, R. F. Sabirianov, Z. Zhu, J. Chu, S. S. Jaswal, and E. Y. Tsymbal. Surface magnetoelectric effect in ferromagnetic metal films. *Phys. Rev. Lett.*, 101: 137201, 2008.

[42] M. K. Niranjan, C.-G. Duan, S. S. Jaswal, and E. Y. Tsymbal. Electric field effect on magnetization at the Fe/MgO (001) interface. *Applied Physics Letters*, 96:222504, 2010.

[43] L. Shu, Z. Li, J. Ma, Y. Gao, L. Gu, Y. Shen, Y. Lin, and C. W. Nan. Thickness-dependent voltage-modulated magnetism in multiferroic heterostructures. *Applied Physics Letters*, 100(2):022405, 2012.

[44] A. Mardana, Stephen Ducharme, and S. Adenwalla. Ferroelectric control of magnetic anisotropy. *Nano Letters*, 11(9):3862–3867, 2011.

[45] Y. Tokura, Y. Tomioka, H. Kuwahara, A. Asamitsu, Y. Moritomo, and M. Kasai. Origins of colossal magnetoresistance in perovskite-type manganese oxides (invited). *Journal of Applied Physics*, 79(8):5288–5291, 1996.

[46] C. A. F. Vaz, J. Hoffman, Y. Segal, J. W. Reiner, R. D. Grober, Z. Zhang, C. H. Ahn, and F. J. Walker. Origin of the magnetoelectric coupling effect in $PbZr_{0.2}Ti_{0.8}O_3$ / $La_{0.8}Sr_{0.2}MnO_3$ multiferroic heterostructures. *Phys. Rev. Lett.*, 104:127202, 2010.

CHAPTER 3

Manipulating magnetism with light

This chapter discusses how magnetic materials can be modified by the excitation with femtosecond laser pulses setting the background for the experiments described in chapters 7 and 8. It starts by describing the relevant time scales in magnetism and continues with a general description of the effects of an ultrashort laser pulse on a magnetic system. The two cases of ultrafast laser induced demagnetisation and magnetisation reversal are then considered[1].

3.1 Relevant time scales in magnetism

The time evolution of magnetisation happens over timescales that span from thousands of years, as in the case of magnetic viscosity [3], to few femtoseconds, as in the case of exchange interaction. Magnetic processes that happen on time scales down to few nanoseconds are related to the propagation of ferromagnetic domain walls in micro and nanostructures [4]. Precessional motions, coherent magnetisation rotations and vortex core dynamics happen on timescales ranging from 1 ns to 100 ps [5, 6, 7]. Elementary interactions in magnetism are related to a shorter time scale varying from 1 fs to 100 ps. More specifically, the time scale related to the exchange interaction varies between 1 fs and 100 fs, while spin-orbit coupling has a longer time scale varying between 100 fs to 10 ps. The recent development of intense lasers capable of producing light pulses with femtosecond duration and the optimisation of conversion schemes for generating strong

[1] This chapter follows from the description given in the following recent reviews: [1, 2]

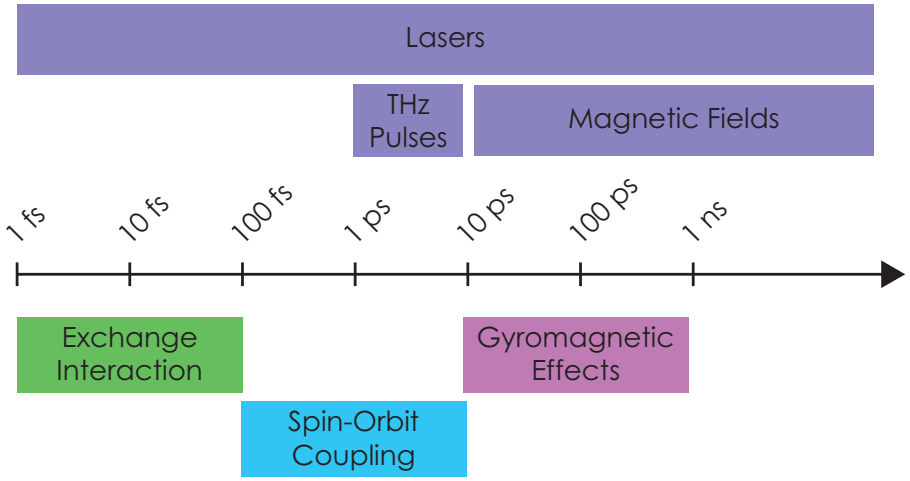

Figure 3.1: Time scales in magnetism and matching excitation sources.

pulses in the THz regime, allowed one to excite magnetic systems at time scales that relate directly to the elementary interactions responsible for magnetism. The study of how the magnetisation reacts to external stimuli on a time scale shorter than 100 ps is commonly termed "ultrafast magnetism". Figure 3.1 shows a summary of the fundamental timescales in magnetism alongside with possible excitations.

3.2 Interaction of magnetic materials with ultrashort optical pulses

Magnetism is related to the spin and orbital angular momenta of the electrons. Femtosecond optical pulses excite the system on a timescale comparable to the exchange interaction and shorter than that of the spin-orbit interaction. As a consequence, the magnetic system is left in a strongly non-equilibrium state where spin-orbit coupling, magnetic anisotropies, and the exchange interaction must be considered as a function of time. Traditional thermodynamical and micro-magnetic approaches are no longer valid, thus it is interesting to investigate how changes in the magnetic properties of the system are related to energy and angular momentum exchange between the thermodynamic reservoirs of the system. A pump laser pulse can excite the magnetic system in three possible ways: through (i) thermal effects, (ii) non-thermal effects requiring the absorption of pump photons, and (iii) non-thermal effects that do not require the absorption of pump photons. A brief description is given next.

Thermal effects: The energy of the incoming laser pulse is absorbed by the system producing a magnetisation change that follows the change in the spin temperature. The energy of the incoming laser pulse is delivered to the electrons and the lattice. Their thermalisation with electron-electron, electron-phonon, and electron-spin processes determines the time scale at which the magnetisation varies. For itinerant ferromagnets electron-electron processes can be very fast, in the sub-100fs regime.

Non-thermal effects involving the absorption of pump photons: These effects involve the direct excitation of electronic states that are responsible for determining intrinsic properties of the material, such as the exchange constants or the magnetocrystalline anisotropy. While the rate of change in the intrinsic properties is limited only by the characteristics of the pump pulse, the magnetisation of the system will react at a speed which is limited by the subsequent Landau Lifshitz Gilbert dynamic.

Non-thermal effects not requiring the absorption of pump photons: In this case the process is based on coherent stimulated Raman scattering [1]. The incoming circularly polarised photons cause a spin flip process in the ground state of the material with the help of spin-orbit coupling. This mechanism is limited by the timescale associated with the spin-orbit coupling and it can be as fast as 20 fs in the case of materials with high spin-orbit coupling.

The next sections will focus on ultrafast demagnetisation and ultrafast magnetisation reversal that are mainly related to thermal effects. More details about the other processes can be found in [1].

3.3 Ultrafast Demagnetisation

3.3.1 Experimental Observations

Ultrafast demagnetisation upon femtosecond excitation was first measured by Beaurepaire et al. in 1996 on a Ni thin layer using 60 fs pump and probe laser pulses [8]. The measurement was carried out by recording hysteresis loops using the linear magneto-optic Kerr effect (MOKE) for different pump-probe delays. It was found that the magnetisation dropped by 40% within the first picosecond, much faster than what could be expected from the spin-lattice relaxation time. These results were further supported by magnetic second harmonic generation and two-photon photoemission measurements [9, 10].

The extremely fast response of the magnetisation to femtosecond laser pulses raised questions about the interpretation of the experimental observations. Indeed, it was

Element	Structure	τ_d (fs)	$\Delta M/M$	Method
Co	15 nm film	160 - 240	10%-50%	Optical MOKE [15]
Co	$Co_{0.5}Pd_{0.5}$ 15 nm	220±20	≈50%	fs-XMCD [16]
Fe	7 nm film	50 - 75	8% - 30%	Optical MOKE [17]
Fe	10 nm film	98±26	18%	XUV T-MOKE [18]
Ni	10 nm film	157±9	40%	XUV T-MOKE [18]
Ni	17 nm film	130±40	≈100%	fs-XMCD [19]
Ni	10 nm film	74±4	2%	Optical MOKE [20]
Gd	10 nm film	760±250	30%	fs-XMCD [21]
Tb	10 nm film	740±250	50%	fs-XMCD [21]

Table 3.1: Measured demagnetisation time constants for selected experiments on different magnetic systems.

demonstrated both experimentally and theoretically, that care must be taken when considering second harmonic generation or MOKE measurements in the first few hundreds of femtosecond, as they can be strongly affected by reflectivity changes due to state blocking effects and dichroic bleaching [11, 12]. These uncertainties triggered the development of complementary techniques that benefit from resonantly enhanced magnetic contrast mechanisms, such as magneto-optic Kerr effect in the extreme ultraviolet, and x-ray magnetic circular dichroism. Experiments carried out with these techniques confirmed the earlier observations using non resonant magneto-optic effects [13, 14].

Ultrafast demagnetisation processes have been studied in a variety of thin layers of magnetic elements and alloys. Table 3.1 shows a list of the measured demagnetisation time constants from different experiments for selected magnetic elements. Typically the demagnetisation times from different experiments are compared on the basis of the laser fluence at the sample position. However, light absorption strongly depends on the layer stack of the sample making particularly difficult to estimate the amount of energy absorbed by the magnetic system from the laser pulse. A better parameter when comparing different experiments is the amount of magnetisation quenching $\Delta M/M$ observed in the measurement, which is proportional to the absorbed energy. Although some discrepancies in the reported demagnetisation times remain even after taking this parameter into account, the overall agreement of the data obtained in different experiments improves. It is possible to observe that while transition metal ferromagnets demagnetise on a time scale varying between 70 fs to 200 fs, rare earths ferromagnets react on a longer time scale. This can be related to the fact that the energy from the infrared laser pulse is absorbed mainly by the 5d electrons and not by the 4f electrons, which are the ones mainly responsible for magnetism [22]. In this respect, it would be interesting to investigate how the demagnetisation time for rare earths ferromagnets varies when the system is pumped at resonance with one of the $N_{6,7}$ absorption edges in the deep ultraviolet.

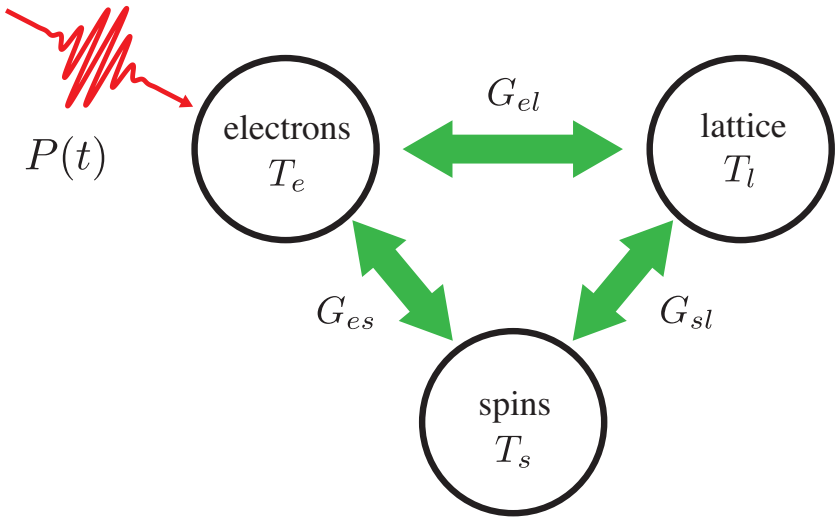

Figure 3.2: Schematic representation of the three reservoirs (electrons, spins and lattice) involved in the three temperature phenomenological model.

In addition, the role of the polarisation state of the pump pulses was investigated. This information is important to discriminate whether or not a direct coupling between photons and spins is present. Dalla Longa et al. [20] studied the ultrafast demagnetisation of Ni using linearly and circularly polarised laser pulses. They have found that the polarisation of the incoming pump pulse does not influence the demagnetisation time constant. Recently, the effect of a magnetic domain structure was also examined by Vodungbo et al. in Co/Pd multilayers [23]. They observed that the magnetic domains show a local, rapid loss of magnetisation similar to what was observed in uniformly magnetised transition metal films. Most importantly, the magnetic domain structure remains almost unaffected by the demagnetisation process.

3.3.2 Mechanisms for Ultrafast Demagnetisation

The interpretation of the experimental data is typically performed in the framework of the phenomenological three temperature model [8]. In this model three different reservoirs are considered: the electrons, the lattice and the spins. These three reservoirs interact amongst themselves with couplings that have different microscopic origins (Fig. 3.2). Assuming that a certain degree of thermal equilibrium is present, one can assign a temperature to each reservoir. In the case of the electron reservoir, it is possible to define an electron temperature only when the Fermi-Dirac description of the electron system is valid, *i.e.* only after few tens of femtoseconds from the optical excitation [24].

The time evolution of the system temperatures is described by the following set of

coupled differential equations [8]:

$$C_e \frac{dT_e}{dt} = -G_{el}(T_e - T_l) - G_{es}(T_e - T_s) + P(t) \tag{3.1}$$

$$C_s \frac{dT_s}{dt} = -G_{es}(T_s - T_e) - G_{sl}(T_s - T_l) \tag{3.2}$$

$$C_l \frac{dT_l}{dt} = -G_{el}(T_l - T_e) - G_{sl}(T_l - T_s) \tag{3.3}$$

where C_e, C_s, C_l represents the specific heat of the electron, spin, and lattice reservoirs respectively. T_e, T_s, and T_l are the temperatures of the electron, spin, and lattice reservoirs; G_{el}, G_{es}, and G_{sl} are the electron-lattice, electron-spin and spin-lattice coupling constants respectively. $P(t)$ corresponds to the energy delivered to the system by the laser pulse. While this model has an analytical solution that allows for fitting the experimental data [25], the coupling constants obtained from the fitting are not related to the microscopic mechanisms involved in ultrafast demagnetisation.

Typically, laser-induced ultrafast demagnetisation can be seen as a three step process. Only the electron system has a response time which is fast enough to interact with the incoming photons. In the first step, hot electrons are created on a time scale of ≈ 1 fs; in the second step the electron system thermalises via electron-electron processes, and T_e increases within 50 fs to 500 fs. At last, electron-phonon processes start to heat up the lattice, increasing T_l within ≈ 1 ps.

The processes involving the spin reservoir are more complex. Considering that the magnetisation arises from the spin angular momentum, it is clear that, in order to satisfy angular momentum conservation, some of this angular momentum has to be taken away from the spin system as the magnetisation is quenched. Two channels are available for the dissipation of angular momentum from the spin system: the electrons and the lattice. The spin-lattice coupling is normally weak and considered to have a strength of the order of the magnetocrystalline anisotropy, leading to spin lattice relaxation times above 100 ps for transition metals. This timescale is clearly in contradiction with the sub-1 ps timescale generally observed in experiments and therefore suggests that there must be stronger coupling mechanisms between the spins and the two other reservoirs.

Direct interactions of the pump photons with the spin subsystem could lead to changes in magnetisation happening on a time scale only determined by the pulse rise time. Bigot et al. [26] indicated that ultrafast demagnetisation might be related to a novel relativistic quantum mechanical process. However, the effect is only observed during the overlap of the pump and the probe pulse as observed by Dalla Longa et al. [20], where the effect was interpreted as a consequence of optical coherence. It is important to note that if the angular momentum is modified by a direct interaction of the spins with the

photons, differences in the demagnetisation process should be observed when the pump pulse is linearly or circularly polarised. However, no difference was observed so far [20].

Spin-orbit coupling in ferromagnets is around 50 meV, with a corresponding time constant of ≈20 fs which is fast enough to explain the sub-1 ps drop in magnetisation observed in experiments. Due to spin-orbit coupling, electronic states in a solid are always a mixture of two spin states with a dominant spin-up or spin-down character. If an electron scatters with a phonon for example, there is a probability of a spin flip event. This type of scattering event is normally referred to as Elliott-Yafet spin flip [27]. Koopmans et al. [15] elaborated an extension of the three temperature model including an Elliott-Yafet spin-flip rate. Although this model reproduces the time evolution observed in ultrafast demagnetisation experiments, it is under debate whether the demagnetisation rates due to spin-flip scattering are large enough to explain experimental observations.

More recently, Battiato et al. [28] have proposed a new model that is not based on a transfer of angular momentum but on the transport of charge carriers out of the excited area (superdiffusive spin transport). In their model, a photon excites an electron from a d-band to sp-like bands having higher mobility. After the excitation, the electrons start moving out of the pumped area and due to different lifetime of majority and minority electrons, magnetisation is effectively pumped out of the probed area with the speed of electrons in sp-like bands which is ≈ 1 nm/fs. This model was successfully employed to reproduce the degree of demagnetisation as well as the time evolution of a previous experiment on a nickel film [14]. Although still under debate, a direct experimental proof of this model was observed in multilayer structures [29, 30, 31].

It is clear that although ultrafast demagnetisation is a heavily studied phenomenon both from an experimental and a theoretical point of view, a clear picture of its microscopic origin is still missing. In particular, all models that have been proposed up to now are based on data from pump-probe measurements. As it will be clearer in chapter 8, such type of measurements neglect eventual contributions from irreversible phenomena. To address their unexplored effect, we have developed a new experimental approach that allowed us to record in real time the laser induced demagnetisation process of ferromagnetic thin films. The concept and the results of this experiment are described in chapter 8.

3.4 Ultrafast Magnetisation Reversal

It is commonly accepted that the speed at which the magnetisation can be switched is limited by the magnetic precession time scale. Since magnetic switching may happen in half a precessional period, one could imagine that the switching can be arbitrarily fast and the limit is set only by the strength of the applied magnetic field pulse. However, it

was shown that magnetic switching becomes unreliable for magnetic field pulses shorter than 2 ps [32]. In parallel to this, Kimel et al. [33] discovered the possibility of employing the inverse Faraday effect to generate ultrashort magnetic field pulses by illuminating a magnetic dielectric with circularly polarised laser pulses.

More recently, Stanciu et al. [34] discovered that the magnetisation was deterministically reversed in a GdFeCo sample upon illumination with single 40 fs circularly polarised laser pulses. GdFeCo is a ferrimagnetic amorphous alloy that is employed in magneto-optical recording applications (see chapter 4). Time-resolved MOKE measurements confirmed that the magnetisation reversal happens without precessional motions and goes through a state where the magnetisation is fully quenched [35]. To investigate further on the origin of the ultrafast laser-induced magnetisation switching, time resolved XMCD measurements were performed on GdFeCo [36]. This experiment allowed to investigate separately the time evolution of the magnetisation in the Gd and Fe sublattices. It was observed that upon laser excitation, the Gd and the Fe demagnetise on very different time scales despite their antiferromagnetic coupling. More surprisingly, after the complete demagnetisation of the Fe, its magnetic moment remains aligned parallel to the one of Gd for ≈ 1 ps generating a transient ferromagnetic state. Although the experiment could not reconstruct the full relaxation to the reversed state, atomistic simulations confirmed that this transient ferromagnetic state relaxes deterministically to a stable state where the net magnetisation of the ferrimagnet has switched.

This discovery demonstrated that the different demagnetisation times of the rare earth and the transition metal sub-lattices had a key role in the ultrafast magnetisation reversal, and suggested that a strong link is present between this observation and ultrafast demagnetisation. Further theoretical efforts pointed out that ultrafast magnetisation reversal was related to an ultrafast heating of the magnetic system, that is to say, the process is purely thermal. This was experimentally confirmed by showing that 50 fs long linearly polarised laser pulses can also induce ultrafast magnetisation reversal in GdFeCo [37, 38].

The role of the polarisation of the incoming pump photons on the ultrafast switching in GdFeCo is still under debate. In this respect, Alebrand et al. have shown that a certain degree of circular polarisation is needed to achieve ultrafast magnetisation reversal [39]. Recently, Khorsand et al. [40] conducted a thorough study of the helicity dependence of ultrafast magnetisation reversal. They concluded that the differences in light absorption caused by magnetic circular dichroism can quantitatively explain the helicity dependence that was originally found in the first experiments and that ultrafast magnetisation reversal can indeed happen independently of the polarisation of the incoming light.

The link between ultrafast magnetisation reversal and laser-induced demagnetisation became even stronger after Graves et al. [41] investigated GdFeCo for pump fluences high enough to cause the overall demagnetisation of the sample. Using small angle x-ray scat-

tering they have shown that the sample is organised in nanoregions having different Gd contents and observed Gd spin reversal in the Gd-rich regions due to a non-local momentum transfer from the adjacent Fe-rich regions.

Laser-induced magnetisation reversal was also observed in different materials such as TbCo [42] and TbFe [43] ferrimagnetic alloy as well as ferrimagnetic multilayers [44]. Until recently, it was believed that ultrafast magnetisation reversal could happen only in ferrimagnetic systems. C-H. Lambert et al. [45] demonstrated all-optical control of magnetisation using femtosecond laser pulses in ferromagnetic multilayers. Although the authors suggest that the effect can be explained in the framework of non-thermal laser-induced effects, a complete characterisation involving time-resolved measurements is still missing.

Laser-induced magnetisation reversal may represent a new solution for applications in data recording. Up to now it has been investigated only in continuous layers while for application purposes patterned structures are beneficial. In this regard, chapter 7 describes an experiment that investigates how such switching works in GdFeCo nanostructures.

References

[1] A. Kirilyuk, A. V. Kimel, and Th. Rasing. Ultrafast optical manipulation of magnetic order. *Rev. Mod. Phys.*, 82:2731–2784, 2010.

[2] A. Kirilyuk and Th. Kimel, A. V. Rasing. Laser-induced magnetization dynamics and reversal in ferrimagnetic alloys. *Reports on Progress in Physics*, 76(2):026501, 2013.

[3] P. Gaunt. Magnetic viscosity and thermal activation energy. *Journal of Applied Physics*, 59(12):4129–4132, 1986.

[4] A. Bisig, M. Stärk, M.-A. Mawass, C. Moutafis, J. Rhensius, J. Heidler, F. Büttner, M. Noske, M. Weigand, S. Eisebitt, T. Tyliszczak, B. Van Waeyenberge, H. Stoll, G. Schütz, and M. Kläui. Correlation between spin structure oscillations and domain wall velocities. *Nat. Commun.*, 4, 2013.

[5] J. Raabe, C. Quitmann, C. H. Back, F. Nolting, S. Johnson, and C. Buehler. Quantitative analysis of magnetic excitations in landau flux-closure structures using synchrotron-radiation microscopy. *Phys. Rev. Lett.*, 94:217204, 2005.

[6] S. E. Stevenson, C. Moutafis, G. Heldt, R. V. Chopdekar, C. Quitmann, L. J. Heyderman, and J. Raabe. Dynamic stabilization of nonequilibrium domain configurations in magnetic squares with high amplitude excitations. *Phys. Rev. B*, 87:054423, 2013.

[7] F. Buttner, C. Moutafis, M. Schneider, B. Kruger, C. M. Gunther, J. Geilhufe, C. v. Korff Schmising, J. Mohanty, B. Pfau, S. Schaffert, A. Bisig, M. Foerster, T. Schulz, C. A. F.

Vaz, J. H. Franken, H. J. M. Swagten, M. Klaui, and S. Eisebitt. Dynamics and inertia of skyrmionic spin structures. *Nat. Phys.*, 11(3):225–228, 2015.

[8] E. Beaurepaire, J. C. Merle, A. Daunois, and J. Y. Bigot. Ultrafast spin dynamics in ferromagnetic nickel. *Phys. Rev. Lett.*, 76:4250–4253, 1996.

[9] J. Güdde, U. Conrad, V. Jähnke, J. Hohlfeld, and E. Matthias. Magnetization dynamics of ni and co films on cu(001) and of bulk nickel surfaces. *Phys. Rev. B*, 59:R6608–R6611, 1999.

[10] A. Scholl, L. Baumgarten, R. Jacquemin, and W. Eberhardt. Ultrafast spin dynamics of ferromagnetic thin films observed by fs spin-resolved two-photon photoemission. *Phys. Rev. Lett.*, 79:5146–5149, 1997.

[11] B. Koopmans, M. van Kampen, J. T. Kohlhepp, and W. J. M. de Jonge. Ultrafast magneto-optics in nickel: Magnetism or optics? *Phys. Rev. Lett.*, 85:844–847, 2000.

[12] P. M. Oppeneer and A. Liebsch. Ultrafast demagnetization in ni: theory of magneto-optics for non-equilibrium electron distributions. *Journal of Physics: Condensed Matter*, 16(30):5519, 2004.

[13] C. La-O-Vorakiat, E. Turgut, C. A. Teale, H. C. Kapteyn, M. M. Murnane, S. Mathias, M. Aeschlimann, C. M. Schneider, J. M. Shaw, H. T. Nembach, and T. J. Silva. Ultrafast demagnetization measurements using extreme ultraviolet light: Comparison of electronic and magnetic contributions. *Phys. Rev. X*, 2:011005, 2012.

[14] C. Stamm, T. Kachel, N. Pontius, R. Mitzner, T. Quast, K. Holldack, S. Khan, C. Lupulescu, E. F. Aziz, M. Wietstruk, H. A. Durr, and W. Eberhardt. Femtosecond modification of electron localization and transfer of angular momentum in nickel. *Nat. Mater.*, 6(10):740–743, 2007.

[15] B. Koopmans, G. Malinowski, F. Dalla Longa, D. Steiauf, M. Fahnle, T. Roth, M. Cinchetti, and M. Aeschlimann. Explaining the paradoxical diversity of ultrafast laser-induced demagnetization. *Nat. Mater.*, 9(3):259–265, 2010.

[16] C. Boeglin, E. Beaurepaire, V. Halte, V. Lopez-Flores, C. Stamm, N. Pontius, H. A. Durr, and J. Y. Bigot. Distinguishing the ultrafast dynamics of spin and orbital moments in solids. *Nature*, 465(7297):458–461, 2010.

[17] E. Carpene, E. Mancini, C. Dallera, M. Brenna, E. Puppin, and S. De Silvestri. Dynamics of electron-magnon interaction and ultrafast demagnetization in thin iron films. *Phys. Rev. B*, 78:174422, 2008.

[18] S. Mathias, C. La-O-Vorakiat, P. Grychtol, P. Granitzka, E. Turgut, J. M. Shaw, R. Adam, H. T. Nembach, M. E. Siemens, S. Eich, C. M. Schneider, T. J. Silva, M. Aeschlimann, M. M. Murnane, and H. C. Kapteyn. Probing the timescale of the exchange interaction in a ferromagnetic alloy. *Proceedings of the National Academy of Sciences*, 109(13): 4792–4797, 2012.

[19] C. Stamm, N. Pontius, T. Kachel, M. Wietstruk, and H. A. Dürr. Femtosecond x-ray absorption spectroscopy of spin and orbital angular momentum in photoexcited ni films during ultrafast demagnetization. *Phys. Rev. B*, 81:104425, 2010.

[20] F. Dalla Longa, J. T. Kohlhepp, W. J. M. de Jonge, and B. Koopmans. Influence of photon angular momentum on ultrafast demagnetization in nickel. *Phys. Rev. B*, 75: 224431, 2007.

[21] M. Wietstruk, A. Melnikov, C. Stamm, T. Kachel, N. Pontius, M. Sultan, C. Gahl, M. Weinelt, H. A. Dürr, and U. Bovensiepen. Hot-electron-driven enhancement of spin-lattice coupling in gd and tb $4f$ ferromagnets observed by femtosecond x-ray magnetic circular dichroism. *Phys. Rev. Lett.*, 106:127401, 2011.

[22] R. Carley, K. Döbrich, B. Frietsch, C. Gahl, M. Teichmann, O. Schwarzkopf, P. Wernet, and M. Weinelt. Femtosecond laser excitation drives ferromagnetic gadolinium out of magnetic equilibrium. *Phys. Rev. Lett.*, 109:057401, 2012.

[23] B. Vodungbo, J. Gautier, G. Lambert, A. B. Sardinha, M. Lozano, S. Sebban, M. Ducousso, W. Boutu, K. Li, B. Tudu, M. Tortarolo, R. Hawaldar, R. Delaunay, V. López-Flores, J. Arabski, C. Boeglin, H. Merdji, P. Zeitoun, and J. Lüning. Laser-induced ultrafast demagnetization in the presence of a nanoscale magnetic domain network. *Nat. Commun.*, 3:999, 2012.

[24] H.-S. Rhie, H. A. Dürr, and W. Eberhardt. Femtosecond electron and spin dynamics in Ni/W(110) films. *Phys. Rev. Lett.*, 90:247201, 2003.

[25] L. Guidoni, E. Beaurepaire, and J.-Y. Bigot. Magneto-optics in the ultrafast regime: Thermalization of spin populations in ferromagnetic films. *Phys. Rev. Lett.*, 89:017401, 2002.

[26] J.-Y. Bigot, M. Vomir, and E. Beaurepaire. Coherent ultrafast magnetism induced by femtosecond laser pulses. *Nat. Phys.*, 5(7):515–520, 2009.

[27] R. J. Elliott. Theory of the effect of spin-orbit coupling on magnetic resonance in some semiconductors. *Phys. Rev.*, 96:266–279, 1954.

[28] M. Battiato, K. Carva, and P. M. Oppeneer. Superdiffusive spin transport as a mechanism of ultrafast demagnetization. *Phys. Rev. Lett.*, 105:027203, 2010.

[29] D. Rudolf, C. La-O-Vorakiat, M. Battiato, R. Adam, J. M. Shaw, E. Turgut, P. Maldonado, S. Mathias, P. Grychtol, H. T. Nembach, T. J. Silva, M. Aeschlimann, H. C. Kapteyn, M. M. Murnane, C. M. Schneider, and P. M. Oppeneer. Ultrafast magnetization enhancement in metallic multilayers driven by superdiffusive spin current. *Nat. Commun.*, 3:1037, 2012.

[30] A. Eschenlohr, M. Battiato, P. Maldonado, N. Pontius, T. Kachel, K. Holldack, R. Mitzner, A. Föhlisch, P. M. Oppeneer, and C. Stamm. Ultrafast spin transport as key to femtosecond demagnetization. *Nat. Mater.*, 12(4):332–336, 2013.

[31] A. R. Khorsand, M. Savoini, A. Kirilyuk, and Th. Rasing. Optical excitation of thin magnetic layers in multilayer structures. *Nat. Mater.*, 13(2):101–102, 2014.

[32] I. Tudosa, C. Stamm, A. B. Kashuba, F. King, H. C. Siegmann, J. Stohr, G. Ju, B. Lu, and D. Weller. The ultimate speed of magnetic switching in granular recording media. *Nature*, 428(6985):831–833, 2004.

[33] A. V. Kimel, A. Kirilyuk, P. A. Usachev, R. V. Pisarev, A. M. Balbashov, and Th. Rasing. Ultrafast non-thermal control of magnetization by instantaneous photomagnetic pulses. *Nature*, 435(7042):655–657, 2005.

[34] C. D. Stanciu, F. Hansteen, A. V. Kimel, A. Kirilyuk, A. Tsukamoto, A. Itoh, and Th. Rasing. All-optical magnetic recording with circularly polarized light. *Phys. Rev. Lett.*, 99: 047601, 2007.

[35] K. Vahaplar, A. M. Kalashnikova, A. V. Kimel, S. Gerlach, D. Hinzke, U. Nowak, R. Chantrell, A. Tsukamoto, A. Itoh, A. Kirilyuk, and Th. Rasing. All-optical magnetization reversal by circularly polarized laser pulses: Experiment and multiscale modeling. *Phys. Rev. B*, 85:104402, 2012.

[36] I. Radu, K. Vahaplar, C. Stamm, T. Kachel, N. Pontius, H. A. Durr, T. A. Ostler, J. Barker, R. F. L. Evans, R. W. Chantrell, A. Tsukamoto, A. Itoh, A. Kirilyuk, Th. Rasing, and A. V. Kimel. Transient ferromagnetic-like state mediating ultrafast reversal of antiferromagnetically coupled spins. *Nature*, 472(7342):205–208, 2011.

[37] T. A. Ostler, J. Barker, R. F. L. Evans, R. W. Chantrell, U. Atxitia, O. Chubykalo-Fesenko, S. El Moussaoui, L. Le Guyader, E. Mengotti, L. J. Heyderman, F. Nolting, A. Tsukamoto, A. Itoh, D. Afanasiev, B. A. Ivanov, A. M. Kalashnikova, K. Vahaplar, J. Mentink, A. Kirilyuk, Th. Rasing, and A. V. Kimel. Ultrafast heating as a sufficient stimulus for magnetization reversal in a ferrimagnet. *Nat. Commun.*, 3:666, 2012.

[38] L. Le Guyader, S. El Moussaoui, M. Buzzi, R. V. Chopdekar, L. J. Heyderman, A. Tsukamoto, A. Itoh, A. Kirilyuk, Th. Rasing, A. V. Kimel, and F. Nolting. Demonstration of laser induced magnetization reversal in gdfeco nanostructures. *Applied Physics Letters*, 101(2):022410, 2012.

[39] S. Alebrand, A. Hassdenteufel, D. Steil, M. Cinchetti, and M. Aeschlimann. Interplay of heating and helicity in all-optical magnetization switching. *Phys. Rev. B*, 85:092401, 2012.

[40] A. R. Khorsand, M. Savoini, A. Kirilyuk, A. V. Kimel, A. Tsukamoto, A. Itoh, and Th. Rasing. Role of magnetic circular dichroism in all-optical magnetic recording. *Phys. Rev. Lett.*, 108:127205, 2012.

[41] C. E. Graves, A. H. Reid, T. Wang, B. Wu, S. de Jong, K. Vahaplar, I. Radu, D. P. Bernstein, M. Messerschmidt, L. Müller, R. Coffee, M. Bionta, S. W. Epp, R. Hartmann, N. Kimmel, G. Hauser, A. Hartmann, P. Holl, H. Gorke, J. H. Mentink, A. Tsukamoto, A. Fognini, J. J. Turner, W. F. Schlotter, D. Rolles, H. Soltau, L. Strüder, Y. Acremann, A. V. Kimel, A. Kirilyuk, Th. Rasing, J. Stöhr, A. O. Scherz, and H. A. Dürr. Nanoscale spin reversal by non-local angular momentum transfer following ultrafast laser excitation in ferrimagnetic gdfeco. *Nat. Mater.*, 12(4):293–298, 2013.

[42] S. Alebrand, M. Gottwald, M. Hehn, D. Steil, M. Cinchetti, D. Lacour, E. E. Fullerton, M. Aeschlimann, and S. Mangin. Light-induced magnetization reversal of high-anisotropy tbco alloy films. *Applied Physics Letters*, 101(16):162408, 2012.

[43] A. Hassdenteufel, B. Hebler, C. Schubert, A. Liebig, M. Teich, M. Helm, M. Aeschlimann, M. Albrecht, and R. Bratschitsch. Thermally assisted all-optical helicity dependent magnetic switching in amorphous fe100–xtbx alloy films. *Advanced Materials*, 25(22):3122–3128, 2013.

[44] S. Mangin, M. Gottwald, C-H. Lambert, D. Steil, V. Uhlíř, L. Pang, M. Hehn, S. Alebrand, M. Cinchetti, G. Malinowski, Y. Fainman, M. Aeschlimann, and E. E. Fullerton. Engineered materials for all-optical helicity-dependent magnetic switching. *Nat. Mater.*, 13(3):286–292, 2014.

[45] C-H. Lambert, S. Mangin, B. S. D. Ch. S. Varaprasad, Y. K. Takahashi, M. Hehn, M. Cinchetti, G. Malinowski, K. Hono, Y. Fainman, M. Aeschlimann, and E. E. Fullerton. All-optical control of ferromagnetic thin films and nanostructures. *Science*, 345 (6202):1337–1340, 2014.

CHAPTER 4

Sample Details and Fabrication Methods

Nowadays sample growth techniques such as molecular beam epitaxy, sputtering and pulsed laser deposition allow for the deposition of thin layers with atomically flat surfaces, growth of epitaxial oxides, and material stacks with sharp interfaces. In parallel to the advancements in sample growth, thanks to the continuous developments in electron beam lithography, it is now possible to define laterally confined structures down to few tens of nanometers. The combination of these techniques allows for the production of highly engineered samples, which is of extreme importance when studying interfacial coupling mechanisms and magnetic properties. This chapter introduces the samples and sample fabrication methods used for the measurements presented in the subsequent chapters. First, the description of how Ni and $La_{0.66}Sr_{0.33}MnO_3$ structures were defined on PMN – PT ferroelectric single crystals to study strain mediated magnetoelectric coupling. This is followed by a description of the nanostructuring process of GdFeCo ferrimagnetic alloys in order to study the role of patterning on all-optical switching. At last it is described how thin layers of 3d ferromagnetic metals were produced in order to study ultrafast demagnetisation dynamics.

4.1 Ni / PMN-PT multiferroic nanostructures

This section describes the constituting elements and the patterning process employed to prepare strain coupled Ni nanostructures on $Pb(Mg_{0.33}Nb_{0.66})O_3$-$PbTiO_3$ (PMN-PT) ferroelectric single crystals.

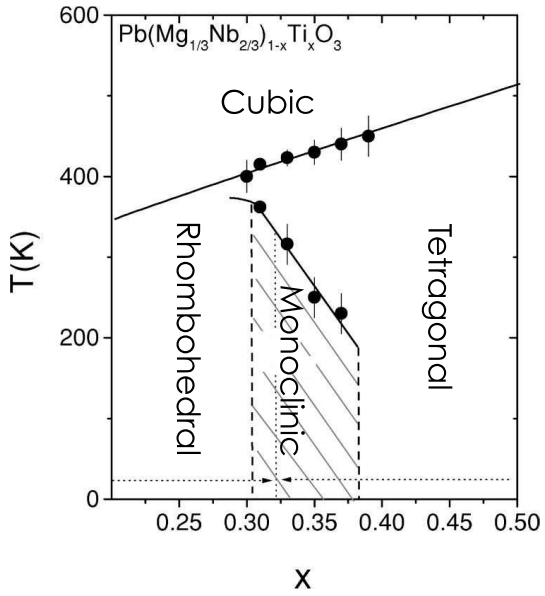

Figure 4.1: Phase diagram for the PMN-PT solid solution. Adapted from [5].

4.1.1 Nickel

Nickel is one of the only four elemental ferromagnets (Co, Fe, Ni, Gd) that is ferromagnetically ordered at room temperature. It is a 3d ferromagnet having a curie temperature of 627 K and a saturation magnetisation of $\mu_0 M = 0.64$ T. The single crystal structure is face centered cubic with a lattice constant of 3.499 Å. In its polycrystalline form, pure nickel exhibits a magnetostriction effect with a saturation magnetostriction coefficient $\lambda_p = -34$ppm [1]. This, together with its low magnetic anisotropy, makes Ni a good ferromagnetic constituent in strain mediated artificial multiferroics.

4.1.2 PMN-PT type ferroelectrics

PMN-PT is a relaxor ferroelectric material with remarkable dielectric and electromechanical properties at room temperature [2]. (1-x)PMN-xPT ferroelectrics are a solid solution of the relaxor ferroelectric $Pb(Mg_{0.33}Nb_{0.66})O_3$ (PMN) and the ferroelectric $PbTiO_3$ (PT). Figure 4.1 shows the phase diagram for the PMN-PT$_x$ solid solution. The shaded area highlights a region identified as morphotrophic phase boundary in which different crystal structures (rhombohedral, monoclinic and tetragonal) coexist as macrodomains inside the specimen. This coexistence is at the origin of the peculiar dielectric and piezoelectric properties of this ferroelectric [3]. More details about PMN-PT can be found here [4].

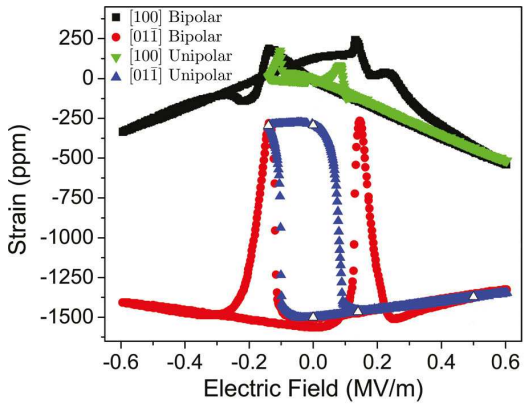

Figure 4.2: Strain vs. electric field curves measured with a strain gauge along the [100] and [01$\bar{1}$] crystallographic directions. Bipolar and unipolar refer to whether or not the ferroelectric polarisation is reversed during the electric field sweep. Adapted from [6].

The PMN-PT crystals employed in this work were grown using the modified Bridgman growth method by Atom Optics Co., LTD (Shanghai, China) and have a nominal composition of $x \approx 0.32$. For (011) cut crystals, x-ray diffraction measurements confirm that the main crystal structure of PMN-PT is rhombohedral with ⟨111⟩ polar axes. In (011) PMN-$PT_{0.32}$ crystals the reorientation process of the ferroelectric polarisation gives rise to a strong strain change at E =0.15 MV m^{-1} as shown by the red curve in figure 4.2. The blue curve in figure 4.2 shows that when the applied electric field is brought back to 0 MV m^{-1} at the point in which the strain change is maximum, the strain state of the system is not altered [6]. This strong and remanent strain change makes PMN-PT a perfect material for the production of strain-mediated artificial multiferroics.

4.1.3 Sample Fabrication

For the measurement presented in section 6.3 we have defined artificial multiferroic nanostructures using (011) PMN-$PT_{0.32}$ as a single crystal ferroelectric substrate and a patterned Ni thin film as a magnetostrictive ferromagnet. Figure 4.3 shows the processing steps for the preparation of the Ni / PMN-PT multiferroic nanostructures. First, a 50 nm Ti layer, used as a back contact, and a 50 nm Pt layer, used as a top contact and buffer layer, were deposited by dc sputtering. After patterning the polymethyl methacrylate (PMMA) resist layer to defining the nanostructures using electron-beam lithography, a 3 nm Ti / 10 nm Ni / 2 nm Pt trilayer was deposited by electron beam evaporation. The final Pt layer acts as a capping layer and prevents oxidation. The subsequent lift-off resulted in isolated magnetic nanostructures. It is important to mention that the choice of the correct buffer layer was crucial to ensure a proper growth of the Ni layer. Different buffer layers such

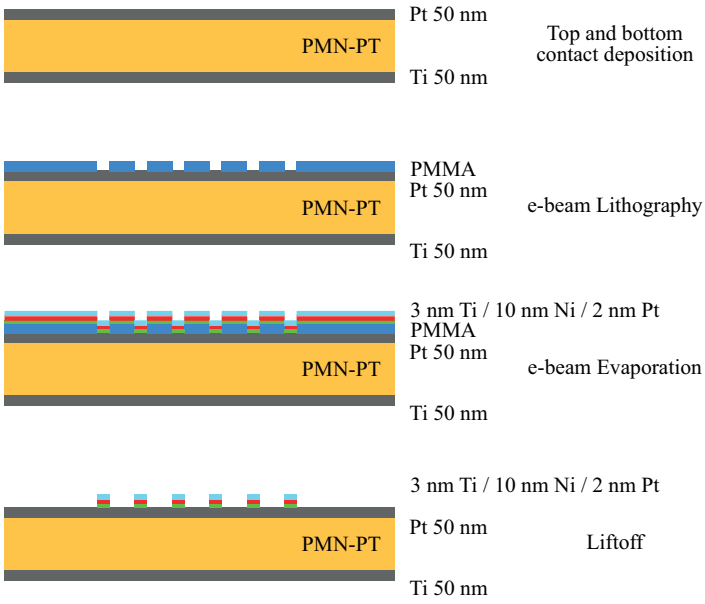

Figure 4.3: Processing steps for the preparation of Ni / PMT-PT artificial multiferroic nanostructures

as Cu and Ta were considered but their surface was too rough to preserve the magnetic properties of the Ni nanostructures.[1]

4.2 LSMO / PMN-PT multiferroic microstructures

To investigate how epitaxial growth affects strain mediated magnetoelectric coupling, $La_{0.66}Sr_{0.33}MnO_3$ microstructures were defined on (011) PMN-$PT_{0.32}$ single crystals ferroelectrics.

4.2.1 $La_{0.66}Sr_{0.33}MnO_3$ (LSMO)[2]

$La_{0.66}Sr_{0.33}MnO_3$ (LSMO) is a half-metallic mixed valence manganite of the type $RE_{1-x}M_xMnO_3$ where RE is a rare earth (in this case La) and M is an alkaline metal (in this case Sr). The system crystallises in the ABO_3 perovskite structure (Fig. 4.4a) where the La trivalent ions and the Sr divalent ions occupy the A site. The B site is at the centre of a BO_6 oxygen octahedron and is occupied by mixed valence Mn^{3+} and Mn^{4+} ions. The valence imbalance can be directly controlled by the doping level x. Increasing the fraction of the

[1]The sample fabrication was carried out by J. L. Hockel at the University of California-Los Angeles, USA.
[2]This section follows from the description given in [7]

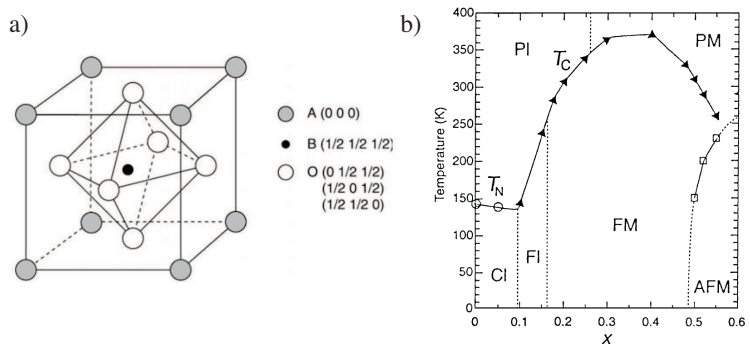

Figure 4.4: (a) ABO_3 perovskite structure. (b) $La_{1-x}Sr_xMnO_3$ phase diagram. PI, PM, and CI indicate the paramagnetic insulating,paramagnetic metallic, and spin-canted insulating states, respectively. FI and FM denote the ferromagnetic insulating and ferromagnetic metallic states, respectively. Adapted from [7, 8].

alkaline metal increases the fraction of Mn^{3+} ions leading to a very rich electronic phase diagram as a function of doping (Fig. 4.4b) [7].

The measurements presented in section 6.4 focus on the particular doping level of $x = 0.33$ corresponding to the highest T_c value and magnetisation. It is important to mention that magnetism in LSMO is governed by the exchange interactions between the Mn atoms. The interactions between two neighbouring Mn atoms are mediated by an O atom and are regulated by the overlap of the Mn 3d orbitals with the O 2p orbitals. This suggest that structural modifications like those obtained applying epitaxial strains or external pressures can lead to dramatic changes in the magnetic properties of the manganite making them an interesting candidate to evaluate the effects of strain mediated magnetoelectric coupling.

4.2.2 Sample Fabrication

Figure 4.5 shows the processing steps used here to define LSMO/PMN-PT artificial multiferroic microstructures. At first, 17 nm thick LSMO layers were grown on (011) PMN-$PT_{0.32}$ using pulsed laser deposition. The film was synthesised from a stoichiometric target using a laser fluence of 1.3 J cm^{-2} at a repetition rate of 0.5 Hz while the PMN-PT substrate was kept in a 300 mbar O_2 ambient environment at a constant temperature of 1000 K [9].

To define microstructures on the LSMO layer we have employed a combination of electron-beam lithography technique and ion-implantation. A 70 nm thick Cr mask layer was deposited by thermal evaporation and patterned using a standard electron beam lithography and lift-off process. The sample was then exposed to 60 keV Ar^+ ions for a dose of 8.3×10^{13} ions/cm^2 and 20 keV Ar^+ ions for a dose of 1.7×10^{13} ions/cm^2. The effect of the

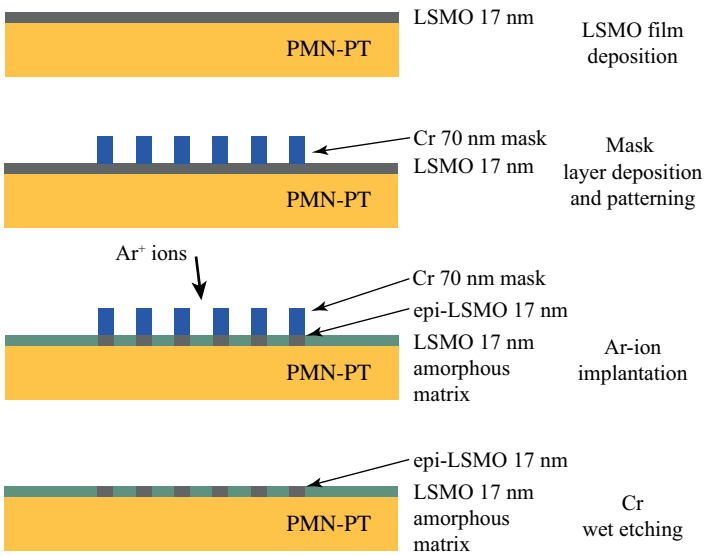

Figure 4.5: Processing steps for the preparation of LSMO / PMT-PT artificial multiferroic nanostructures

ion-implantation is to render the areas which are not protected by the Cr mask amorphous. As a result, ferromagnetic epitaxial LSMO microstructures are defined within a paramagnetic amorphous LSMO matrix. As a last step, the Cr mask is removed by wet etching in a commercial chromium etching solution. A more details description of the patterning process works is described in [10].[3]

4.3 GdFeCo nanostructured samples

4.3.1 GdFeCo

GdFeCo is a rare-earth/transition-metal amorphous alloy that was optimised by Sony in the 1990s for magneto-optical recording applications [11]. GdFeCo has a ferrimagnetic structure with two magnetic sublattices, M_{RE} and M_{TM}, corresponding to the rare earth and transition metal magnetic moments respectively. The M_{RE} and M_{TM} sublattices are antiferromagnetically coupled, while the intra-sublattice exchange interactions are ferromagnetic. GdFeCo is one of the few materials that show a perpendicular magnetic anisotropy in the amorphous state which makes it well suited for magneto-optical applications [12]. It also features the presence of a magnetisation compensation temperature

[3]The sample fabrication was carried out by Dr. C. A. F. Vaz at the Paul Scherrer Institut, Villigen, Switzerland. The LSMO layer was grown by Dr. R. V. Chopdekar at the University of California-Davis, USA.

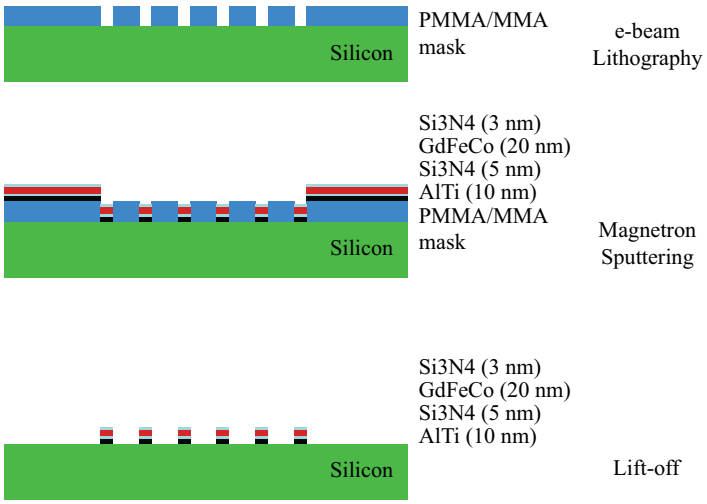

Figure 4.6: Processing steps for the preparation of GdFeCo nanostructures

T_M, where M_{RE} and M_{TM} sublattices have the same magnetisation value and cancel each other, resulting in a zero net magnetisation. $Gd_xFe_{1-x-y}Co_y$ can be prepered in a wide range of compositions, varying the Gd and Co content. Increasing the content of Co improves the Curie temperature T_c of the alloy. Variations in the Gd content lead to a shift in T_M with a consequent tuning of the coercivity and domain size of the material [13].

4.3.2 Sample Fabrication

Figure 4.6 shows the processing steps that lead to the creation of isolated GdFeCo nanostructures. First, a resist mask was prepared on a silicon wafer using electron beam lithography. To ensure proper lift off, the resist mask consisted of a multilayer structure of methyl-methacrylate and poly-methyl-methacrylate of varying thicknesses. After exposure and development, the following multilayer structure was deposited using a magnetron sputtering technique: AlTi (10 nm) / Si_3N_4 (5 nm) / $Gd_{24.5}Fe_{66.1}Co_{9.4}$ (20 nm) / Si_3N_4 (5 nm). The AlTi layer is used as a reflective and heatsink layer, the first Si_3N_4 layer serves the purpose of a buffer layer for the growth of GdFeCo, while the second Si_3N_4 layer acts as a capping layer to prevent oxidation. It is important to point out that the Si_3N_4 capping layer was chosen to be significantly thinner than what is used in optical pump-optical probe measurements [14] due to the surface sensitivity of X-PEEM measurements.[4]

[4]The sample fabrication was carried out by A. Weber at the Paul Scherrer Institut, Villigen, Switzerland. The thin films were grown by Dr. A. Tsukamoto and Prof. A. Itoh at the Nihon University, Chiba, Japan.

4.4 Ferromagnetic thin films

4.4.1 Sample growth details

For the measurements presented in chapter 8, continuous thin films of Co and Co/Ni multilayers were produced. Figure 4.7 shows the layer stack that was employed for the different samples. The substrate was chosen to be 525 µm thick silicon to obtain low surface curvature and best flatness. First, a Pd (30 nm) seed layer was deposited using dc sputtering. This is followed by the deposition of a 20 nm thick layer of Co or 20 repetitions of Co(0.2 nm) / Ni(0.2 nm) bilayers. To protect the magnetic layer from oxidation a 3 nm Al layer was grown as a last step. All the depositions were carried out at room temperature. The thickness of the magnetic layers was chosen to match the extinction length in the material at a wavelength of 800 nm in order to achieve a homogeneous pumping.[5]

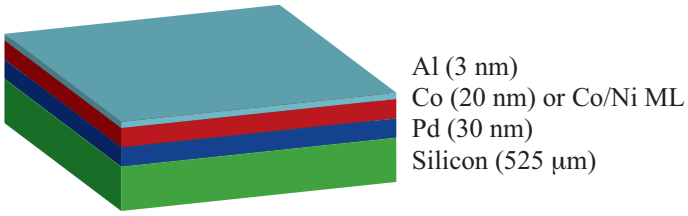

Figure 4.7: Layer stack of the Co and $[\text{Co}(0.2\text{ nm}) / \text{Ni}(0.2\text{ nm})]_{20}$ continuous thin films.

References

[1] S. Chikazumi. *Physics of Ferromagnetism.* Oxford University Press, 1997.

[2] H. Ursic, Z. M. Santo, and M. Kosec. $Pb(Mg_{0.33}Nb_{0.66})O_3$-$PbTiO_3$ (PMN-PT) material for actuator applications. *Smart Materials Research*, 2011(452901):6, 2011.

[3] Z. G. Ye and M. Dong. Morphotropic domain structures and phase transitions in relaxor-based piezo-/ferroelectric $(1-x)PbMg_{1/3}Nb_{2/3}O_3$–$(x)PbTiO_3$ single crystals. *Journal of Applied Physics*, 87(5):2312–2319, 2000.

[4] S. Zhang and F. Li. High performance ferroelectric relaxor-$PbTiO_3$ single crystals: Status and perspective. *Journal of Applied Physics*, 111(031301), 2012.

[5] B. Noheda, D. E. Cox, G. Shirane, J. Gao, and Z.-G. Ye. Phase diagram of the ferroelectric relaxor $(1-x)PbMg_{1/3}Nb_{2/3}O_3$–$(x)PbTiO_3$. *Phys. Rev. B*, 66:054104, 2002.

[5] The samples were grown by Dr. B. Vodungbo and Prof. J. Lüning at Sorbonne Universités, Paris, France.

[6] Tao W., P. Zhao, M. Bao, A. Bur, J. L. Hockel, K. Wong, K. P. Mohanchandra, C. S. Lynch, and G. P. Carman. Domain engineered switchable strain states in ferroelectric (011) $(1-x)PbMg_{1/3}Nb_{2/3}O_3$–$(x)PbTiO_3$ (PMN-PT, $x \approx 0.32$) single crystals. *Journal of Applied Physics*, 109(12):124101, 2011.

[7] A. M. Haghiri-Gosnet and J. P. Renard. CMR manganites: physics, thin films and devices. *Journal of Physics D: Applied Physics*, 36(8):R127, 2003.

[8] E. Dagotto, T. Hotta, and A. Moreo. Colossal magnetoresistant materials: the key role of phase separation. *Physics Reports*, 344(1–3):1–153, 2001.

[9] J. Heidler, C. Piamonteze, R. V. Chopdekar, M. A. Uribe-Laverde, A. Alberca, M. Buzzi, A. Uldry, B. Delley, C. Bernhard, and F. Nolting. Manipulating magnetism in $La_{0.7}Sr_{0.3}MnO_3$ via piezostrain. *Phys. Rev. B*, 91:024406, 2015.

[10] Y. Takamura, R. V. Chopdekar, A. Scholl, A. Doran, J. A. Liddle, B. Harteneck, and Y. Suzuki. Tuning magnetic domain structure in nanoscale $La_{0.7}Sr_{0.3}MnO_3$ islands. *Nano Letters*, 6(6):1287–1291, 2006.

[11] C. G. Stefanita. *Magnetism: Basics and Applications*. Springer Berlin Heidelberg, 2012.

[12] J. Daval and B. Bechevet. Rare earth transition metal alloys for magneto-optical recording. *Journal of Magnetism and Magnetic Materials*, 129(1):98–107, 1994.

[13] M. Ding and S. J. Poon. Tunable perpendicular magnetic anisotropy in GdFeCo amorphous films. *Journal of Magnetism and Magnetic Materials*, 339:51–55, 2013.

[14] A. R. Khorsand, M. Savoini, A. Kirilyuk, A. V. Kimel, A. Tsukamoto, A. Itoh, and Th. Rasing. Role of magnetic circular dichroism in all-optical magnetic recording. *Phys. Rev. Lett.*, 108:127205, 2012.

CHAPTER 5

Imaging of magnetic domains

This chapter describes the experimental methods that are employed in the measurements presented in chapters 6 and 7. It describes how one can produce high resolution images of magnetic domains using x-ray photoemission electron microscopy and how a commercial photoemission electron microscope has been modified to allow for the application of *in situ* electric fields.

5.1 High resolution imaging of magnetic domains

Imaging magnetic domain structures with sub-micrometre resolution had a key role in understanding magnetic interactions at a microscopic scale. Although, different methods are nowadays available to perform high resolution imaging of magnetic domains, this chapter focuses on x-ray photoemission electron microscopy combined with x-ray magnetic circular dichroism. This technique is particularly advantageous in the study of magnetic heterostructures due to its surface and chemical sensitivity. A complete review of the available magnetic imaging techniques can be found in [1].

5.1.1 Photo Emission Electron Microscopy[1]

Due to the high surface sensitivity of photoemission techniques, photoemission electron microscopy (PEEM) is a powerful technique that allows for full-field microspectro-

[1] This section follows from the description given in [2, 3]

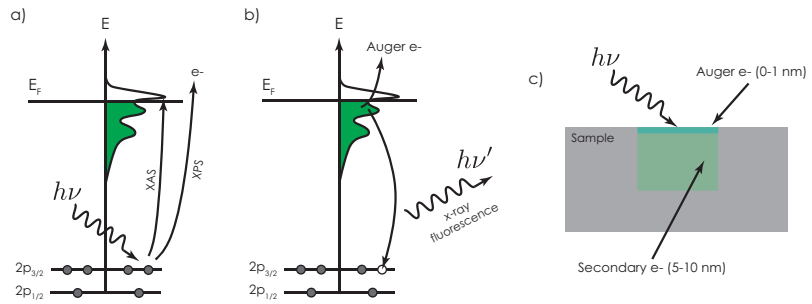

Figure 5.1: (a) Generation of the core hole upon absorption of a photon. (b) Filling of the core hole by a lower binding energy electron and release of the excess energy. (c) Typical escape depths for Auger and secondary electrons.

scopy of surfaces. Although different photoemission electron microscopes are nowadays available, this section focuses on the magnetic microscope designed by ELMITEC that has been employed for the measurements presented in the next chapters. A complete review about PEEM can be found in [4].

In PEEM, the sample under investigation is typically illuminated using UV or x-ray light and the contrast mechanism arises from local variations in the photoelectron yield. Upon absorption of a UV or x-ray photon, an electron from a core level can be ejected from the sample, as in the case of x-ray photoelectron spectroscopy (XPS), or it can be excited to unoccupied states above the Fermi energy as in the case of x-ray absorption spectroscopy (XAS) (Fig. 5.1a). The core hole is then filled by an electron with lower binding energy. The energy difference between the core level and the electron that occupied the core hole is removed by either emitting a photon (x-ray fluorescence) or by the emission of an Auger electron (Fig. 5.1b). Typically, only the Auger electrons generated close to the surface can leave the sample due to their very limited escape depth. Auger electrons can also thermalise by undergoing a series of electron-electron scattering processes that generate a cascade of lower energy secondary electrons having an larger escape depth of 5 nm to 10 nm (Fig. 5.1c). The energy of the electrons leaving the sample ranges from zero to the energy of the incoming photons minus the work function of the sample.

Figure 5.2 shows a schematic view of the commercial ELMITEC SPELEEM used for the experiments carried out in this work. The sample sits on a sample manipulator in Ultra High Vacuum and is illuminated by an x-ray beam at a grazing angle of 16°. The photoemitted electrons are accelerated by a strong electric field towards the objective lens. Their optical path is sketched by the purple line in Figure 5.2. The objective lens creates an image of the sample in the centre of the sector field. The transfer lens (TL) is then used to image the angular distribution of the photoelectrons at the field lens (FL) position, where a round aperture (contrast aperture) reduces the angular acceptance of the microscope

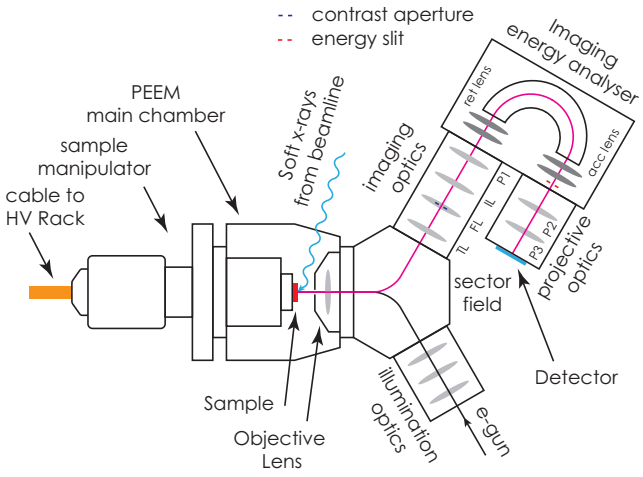

Figure 5.2: Schematic of the ELMITEC SPELEEM microscope.

in order to reduce aberrations. The combined action of FL, IL and the first projective lens (P1) magnifies the image captured by the objective. An imaging energy analyser is then used in combination with the energy slit to select the energy of the photoelectrons used for imaging. The energy slit also limits the energy acceptance of the microscope thereby reducing chromatic aberrations. After the energy analyser the image of the sample is projected, with a further magnification, on the detector using the second and third projector lenses (P2, P3). The detector is composed by a combination of a micro-channel plate and a phosphor screen used to convert the electron image to a photon image. The screen is then imaged by a low noise, high sensitivity charge-coupled-device camera (SensiCAM from PCO imaging).

The typical spatial resolution for PEEM with UV illumination is between 10 nm to 20 nm [5]. When the sample is illuminated with soft x-ray radiation, chromatic aberrations in the microscope are more pronounced and the average spatial resolution is between 30 nm to 50 nm. Instruments that include an electron mirror to correct for spherical and chromatic aberrations achieve better performances and can achieve imaging with a spatial resolution of 5.4 nm under UV illumination and 18 nm using soft x-ray illumination [6].

5.1.2 X-ray Magnetic Circular Dichroism[2]

X-ray Magnetic Circular Dichroism (XMCD) refers to the different x-ray absorption of left and right circularly polarised photons by a magnetic medium. This effect is commonly

[2]This section follows from the description given in [7, 8]

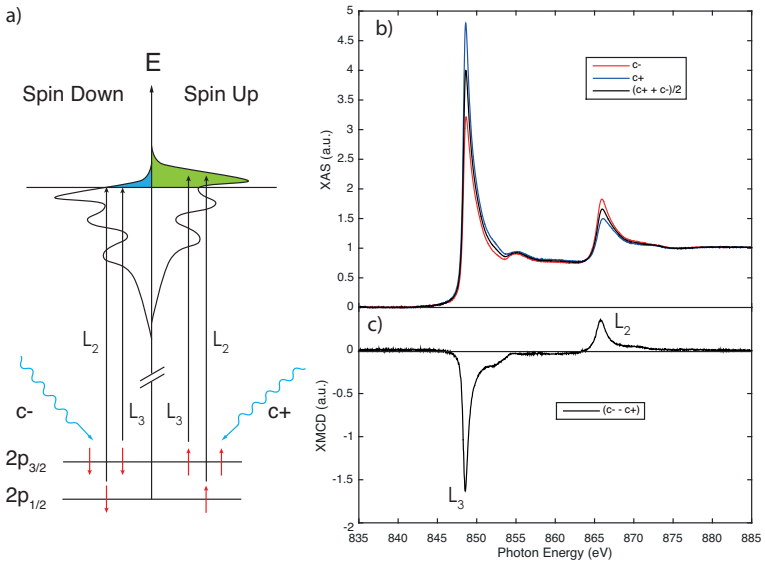

Figure 5.3: (a) Schematic representation of the two step model of XMCD. (b) X-ray absorption spectra for a Ni thin layer acquired with x-ray photons having positive (blue) and negative (red) helicity. (c) Difference spectra highlighting the XMCD effect at the L_3 and L_2 edge. Adapted from [8].

used to determine, in an element specific manner the spin and orbital momenta of an atomic species in a magnetic material. The element specificity arises from the resonant absorption of the incoming photon. Typically soft x-rays are used at resonance to the $L_{2,3}$ edges (corresponding to 2p to 3d transitions) in the case of 3d elements, or at resonance with the $M_{4,5}$ edges in the case of 4f magnetic systems. This choice allows to directly probe the electronic states responsible for magnetism, giving unprecedented sensitivity to the magnetic property of the material. Although a full quantum mechanical description is possible, the XMCD effect can be explained in a simpler picture as a two step process [9].

The first step involves the absorption of the incoming photon and the excitation of a photoelectron. Let us consider the case of a 3d ferromagnet. Due to the strong core-level spin-orbit coupling the 2p core states are split in two levels (Fig. 5.3a), one with total angular momentum $J = L + S = 3/2$ (L_3 edge) and one with $J = L - S = 1/2$ (L_2 edge). When an x-ray photon with positive (negative) helicity is absorbed, a photoelectron is generated and the photon can transfer its angular momentum $\hbar$ ($-\hbar$) to the orbital angular momentum of the photoelectron. Thanks to the spin-orbit coupling, part of the orbital angular momentum can be transferred to the spin momentum of the excited photoelectron creating a spin polarisation of the excited photoelectrons. It can be shown that at the L_3 edge incoming photons with positve helicity generate 62.5% spin-up electrons and 37.5% spin-down electrons. At the L_2 edge, the spin-orbit coupling is opposite and photons with

positive helicity generate 25% spin-up electrons and 75% spin-down electrons. [10]

In the second step, the excited photoelectron transitions to the empty 3d states. Due to the exchange interaction, the 3d band is spin-split (Fig. 5.3a) and acts as a detector for the spin polarised photoelectron. For a sample with a net magnetisation in the "up" direction, the spin-up holes outnumber the spin-down holes causing a preferential absorption of positive helicity photons at the L_3 edge and of negative helicity photons at the L_2 edge. The opposite holds if the sample has a net magnetisation in the "down" direction.

Figure 5.3b,c show a typical XMCD measurement for a uniformly magnetised Ni thin layer at the $L_{3,2}$ edges. The red and blue curves in figure 5.3b are x-ray absorption spectra acquired for negative and positive photon helicity respectively. Their difference is the XMCD spectrum shown in figure 5.3c. One can observe that the sign of the absorption peaks at the L_3 and L_2 edges is opposite, reflecting the different transition probabilities for the $2p_{3/2}$ and $2p_{1/2}$ core states.

5.1.3 X-ray PEEM (X-PEEM) for magnetic imaging

By employing circularly polarised photons and by tuning the photon energy to the appropriate edge for the material of interest it is possible to combine X-PEEM and the XMCD effect to produce element-specific, high resolution magnetic images. The magnetic contrast is obtained by acquiring one image using photons with positive helicity I_{c_+} and one using photons with negative helicity I_{c_-}. One defines the XMCD image as a pixel-wise calculation of:

$$\text{XMCD} = \frac{I_{c_+} - I_{c_-}}{I_{c_+} + I_{c_-}} \tag{5.1}$$

The contrast in the XMCD image is proportional to the dot product $\vec{M} \cdot \vec{k}$ where $\vec{M}$ is the local sample magnetisation and $\vec{k}$ is the propagation direction of the x-rays. As an example, figure 5.4b shows the I_{c_+}, I_{c_-} and XMCD images of a $5 \times 3\,\mu m^2$ magnetic element fabricated out of $Ni_{0.8}Fe_{0.2}$. The images were acquired at 708 eV (Fe L_3 edge). By analysing how the contrast varies in the XMCD image we can reconstruct the magnetisation configuration of the magnetic element, which in this case is a Landau flux closure state. The average spatial resolution achieved when using X-PEEM for magnetic imaging is approximately 50 nm.

X-PEEM can also produce compositional maps. The elemental contrast image is obtained by the pixel-wise calculation of the ratio between an image acquired at a photon energy resonant with an edge of the material of interest, and an image taken at a pre-edge energy. The contrast in the image is directly correlated to local variations in the composition of the sample.

X-PEEM can also be employed to acquire local, spatially-resolved, x-ray absorption

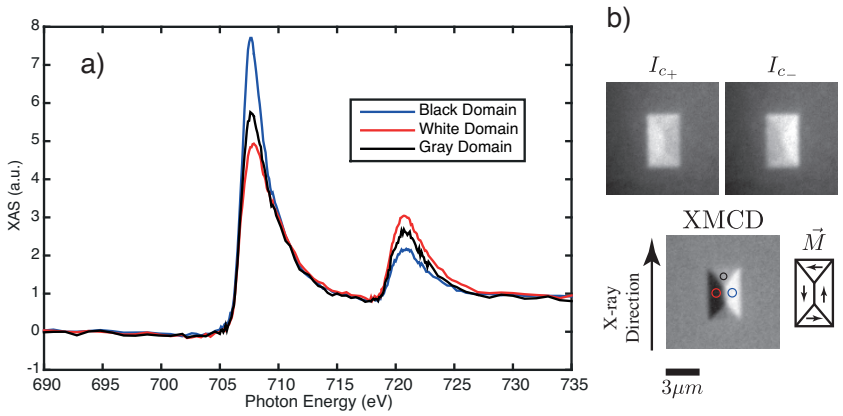

Figure 5.4: (a) X-ray absorption spectra obtained for the three different areas of interest defined in the XMCD image. (b) Images acquired with photons with positve (I_{c+}) and negative (I_{c-}) helicities at the Fe L_3 edge together with the calculated XMCD image and sketch of the magnetic domain pattern of the magnetic element.

spectra. By acquiring images at different photon energy one can define different areas of interest in the image from which it is possible to extract the x-ray absorption spectra. Figure 5.4a shows the result of a photon energy scan with positive helicity photons across the Fe $L_{2,3}$ edges for the three areas of interest defined on the XMCD image in figure 5.4b. The blue curve, corresponding to the area in which the magnetisation is parallel to the x-ray propagation direction, shows higher absorption at the L_3 edge while to the red curve that corresponds to the area in which the magnetisation is antiparallel to the x-ray propagation direction, in agreement to the expected response due to the XMCD effect.

Different PEEM microscopes are implemented at different beamlines in various synchrotron sources around the world such as the Advanced Light Source in Berkeley (USA), the Swiss Light Source in Villigen (CH), BESSY II in Berlin (D) and Elettra in Trieste (IT). In general the beamline layout is optimised for the implementation of the microscope and features a high photon yield monochromator as well as optics capable of producing a homogenous illumination of the sample, which is key for producing high quality images with PEEM.

Some of the experiments presented here were performed using the PEEM installed at the Surface/Interface: Microscopy (SIM) beamline of the Swiss Light Source [11, 12]. SIM delivers x-ray photons to the PEEM microscope using two APPLE-II undulators in a configuration that is particularly advantageous for magnetic microspectroscopy. As clarified above, to obtain an XMCD image one needs to record two images, one using photons with positive helicity and another using photons with negative helicity. Typically, the polarisation of the produced photon is switched by changing the shift of the magnetic arrays in

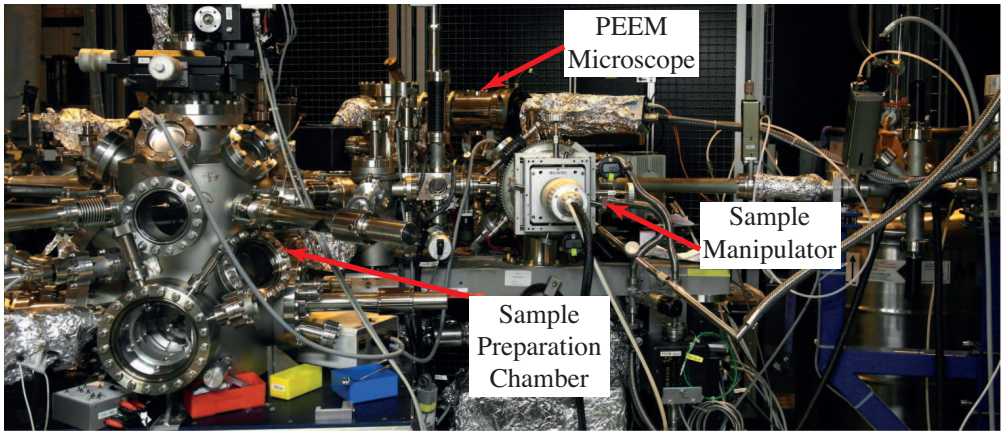

Figure 5.5: Picture of the ELMITEC SPELEEM installed at the SIM beamline of the Swiss Light Source.

the undulator, an operation that typically takes about 30 s to complete. This dead time can be significantly reduced by employing two undulators that are constantly setup to produce light with positive and negative helicity, respectively. One of the two undulators is tuned at the same energy as the monochromator while the other is not. In this way the photons produced by the de-tuned undulator are blocked while the ones produced by the tuned undulator reach the sample. Switching between the two polarisations only requires changing the energy to which the undulator is set. This is achieved by changing the gap distance between the magnetic arrays in the undulator and requires only few seconds.

Figure 5.5 shows a picture of the X-PEEM microscope installed at the SIM beamline of the Swiss Light Source. The system is equipped with a manipulator that allows for the precise positioning of the sample in the field of view of the microscope. In addition, the sample stage can be rotated around its axis by 360°, allowing for the acquisition of XMCD images at different azimuthal angles in order to reconstruct a complete three dimensional map of the magnetisation vector as described in section 7.2. A sample preparation chamber is connected to the microscope and allows for basic sample preparation steps in ultra high vacuum, such as Ar ion sputtering, annealing and deposition of metallic layers.

5.2 Generation of *in situ* electric fields in the PEEM

None of the commercially available photoemisson microscopes allows one to apply *in situ* stimuli such as electric fields during imaging, which is key for a complete investigation of magnetoelectric coupling in multiferroics. The set-up described in this section can be integrated in commercial SPELEEM microscopes and allows for the application of voltages

as high as 1 kV, enabling the investigation of a wide variety of multiferroic systems [3].

5.2.1 Intrinsic requirements for instrumentation

As mentioned earlier in section 5.1.1, in X-PEEM the sample under investigation is illuminated by x-ray photons. Upon absorption of the incoming photons, electrons with a kinetic energy greater than the work function of the sample are photo-emitted and collected by the objective lens of the microscope. A full-field magnified image of the illuminated area is then formed on the detector by means of a set of electron lenses. In order to make this possible, the photo-emitted electrons are accelerated by a constant acceleration voltage of typically −10 kV to −20 kV which is applied between the objective lens of the microscope and the sample.

In the ELMITEC SPELEEM microscope the objective lens is connected to earth ground and the accelerating voltage is directly applied to the sample. An additional bias identified as start voltage is also applied in order to define the centre energy of the photo-emitted electrons accepted by the energy analyser. As a result, the sample ground is biased with respect to earth ground by both the accelerating and the start voltage (Fig. 5.6). All equipment that, for experimental reasons, is electrically connected to the sample has to be referenced to the sample ground. To ease this task, the microscope control rack is equipped with an isolated 19" rack identified as high voltage rack which is biased to the accelerating voltage and that houses the start voltage power supply as well as the Sample Heating, LEEM and Energy Analyser controllers. The six electrical connections to the sample are terminated in this rack.

When a new instrument is integrated in the high voltage rack, two main aspects have to be considered. (i) The exchange of data for instrument control and/or data acquisition purposes has to happen via optical links to maintain the required electrical isolation. (ii) Due to the high electric field ($\approx 10\,\mathrm{kV\,mm^{-1}}$) present between the sample and the PEEM objective lens, arcing may occur, creating a risk of damage for all the instrumentation electrically connected to the sample if appropriate safety measures are not taken. To fulfil these requirements one needs to develop fully customised solutions or to carefully integrate commercial instruments with adequate protection.

To achieve our goal of applying *in situ* electric field stimuli during PEEM measurements, we have introduced the following modifications to the ELMITEC PEEM microscope: (i) A sample holder that allows for electrical connections to the sample; (ii) A computer controlled unit that can generate analog control voltages for driving commercial instruments; (iii) Integrated a commercial high voltage amplifier in the high voltage rack with adequate protection.

[3] Adapted from M. Buzzi, C. A. F. Vaz, J. Raabe and F. Nolting, *Rev. Sci. Inst.* **86** 083702 (2015) [13].

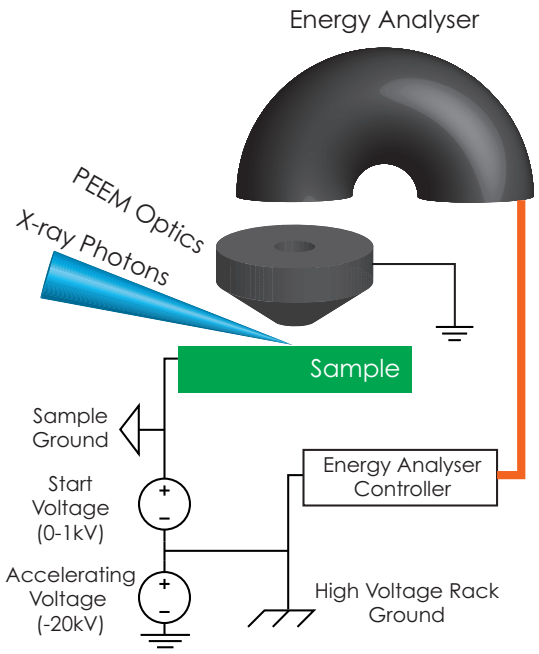

Figure 5.6: Simplified schematic of the ELMITEC PEEM microscope, highlighting the bias voltages necessary for the operation of the microscope. Adapted from [13].

5.2.2 Sample mounting and sample holder

During X-PEEM imaging it is important to take particular care in avoiding the presence of stray electric fields at the sample surface that may cause image aberrations. The standard ELMITEC sample holder clamps the sample against the metallic body of the sample holder using a round clip. While this type of sample holder is optimised for surface science experiments involving sample preparations at high temperature it is not suitable for the application of electric and magnetic fields. We adopted a stainless steel sample holder with four electrical contacts as shown in figure 5.7a. All of the contacts can be used to provide a constant bias voltage to the sample in order to generate an *in situ* electric field. The sample holder also allows for the installation of a small electromagnet that can generate magnetic fields up to 15 mT [14]. When the electromagnet is installed, only two contacts are available to apply bias voltages to the sample.

Artificial multiferroic samples based on single crystal ferroelectrics, such as schematically shown in figure 5.7b, are mounted directly on the top cover of the sample holder using four small drops of silver glue. This mounting technique ensures that the sample is held to the top cover with minimum residual stress and, at the same time, that the top electrode is connected to the sample ground. A Kapton^{TM} insulated copper wire is then glued using

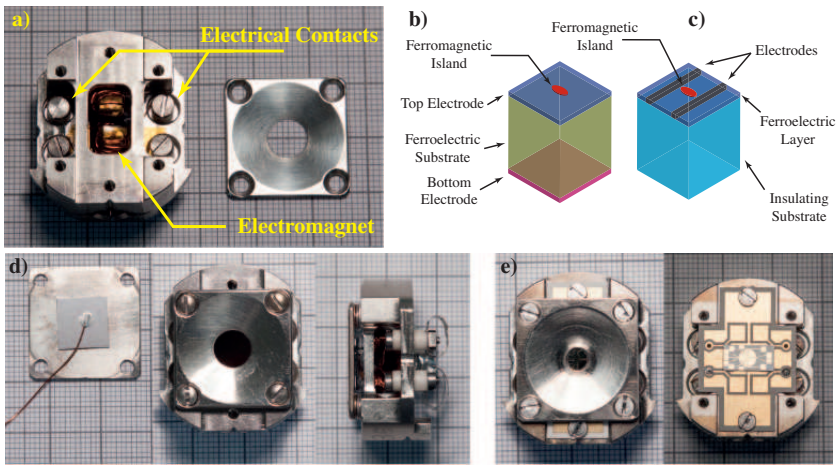

Figure 5.7: (a) Overall view of the sample holder used for PEEM measurements with *in situ* applied electric and magnetic field. (b) Typical structure for artificial multiferroic samples based on single crystal piezoelectrics. (c) Typical structure for thin film artificial multiferroics. Both the ferromagnetic and ferroelectric constituents are in the form of thin films. (d) Mounting procedure for artificial multiferroic samples based on single crystal piezoelectrics (e) Mounting procedure for thin film artificial multiferroic heterostructures. All the pictures are taken using millimeter paper as a background. Adapted from [13].

silver epoxy to the back electrode and then connected to one of the free electrical contacts on the sample holder. In this way the electric field across the sample is generated by applying a bias potential on the back electrode while keeping the top electrode at sample ground in order to avoid spurious electric fields that may cause image distortions. The top cover is fixed to the main body of the sample holder using four screws. A distance of ≈ 1 mm between the sample back electrode and the top part of the sample holder is kept by means of a combination of four spacers and four spring washers that allow to null the sample tilt prior to transferring the sample in vacuum. A side and top view of the fully assembled sample holder is shown in figure 5.7d.

In the case of thin film artificial multiferroics the ferroelectric and ferromagnetic layers are both in the form of thin layers deposited on an insulating substrate as shown in figure 5.7c. The connections to the electrodes for applying an electric field to the ferroelectric layer are achieved either via wire-bonding or by gluing thin gold wires with silver glue to the connection pads defined lithographically on the sample. The connecting wires are then terminated on a circuit board carrier (Fig. 5.7e) that is installed directly on the sample holder. The circuit board carrier is manufactured using a PTFE based laminate (Rogers RO-3003) characterised by a low outgassing rate under ultra high vacuum. The sample carrier board can then be connected to one of the free contacts of the sample holder. The top cover is put in place using spacers to maintain a gap of ≤ 0.3 mm with respect to the

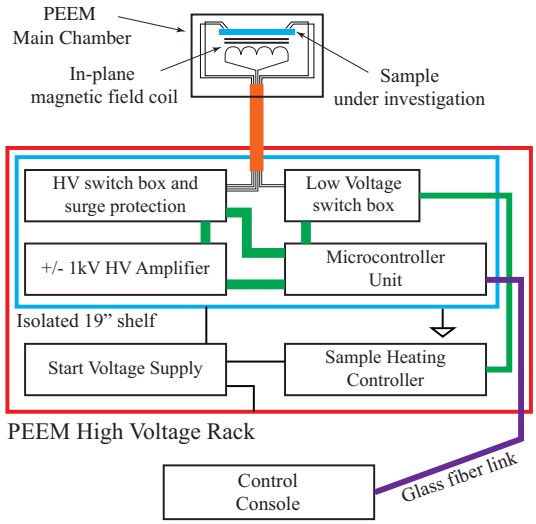

Figure 5.8: Block diagram of the set-up. The energy analyser and electron gun controller which are normally present in the microscope high voltage rack are not shown for sake of simplicity. A fiber-optic link ensures the communication between the microcontroller and an external computer. Adapted from [13].

sample surface. It is important to make sure that the top cover shadows all the bonding wires to the sample to avoid field emission effects that would lead to the destruction of the sample. Figure 5.7e shows a sample mounted using this method.

5.2.3 Control Unit

The reference ground for all the instruments electrically connected to the sample is the sample ground. It differs from the high voltage rack ground by the start voltage as shown in Figure 5.6. As most commercial instruments are not designed to withstand a voltage difference between their chassis ground and the input or output terminals of more than few hundreds volts, we have prepared an isolated 19" shelf that can be installed in the high voltage rack and connected to sample ground. A 100 VA toroidal isolation transformer is used to provide power to 3 different instruments.

Figure 5.8 shows a block diagram of the set-up. All the components are controlled by a home built control unit based on an Atmel ATmega 2560 micro-controller. All the required functions can be controlled by sending SCPI commands via a serial link on optical fibre. To generate the voltage required to apply electric fields at the sample position, the unit sets a ±10 V analog output which is connected to a bipolar high voltage amplifier (Trek 2210) that can supply up to ±1 kV. A small relay box built using high voltage reed relays routes the output of the high voltage amplifier to the contact on the sample holder.

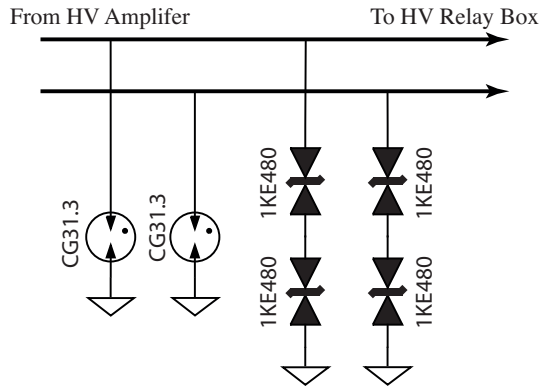

Figure 5.9: Schematic diagram for the surge protection circuit integrated in the high voltage switch box. Adapted from [13].

To prevent damage to the output stage of the high voltage amplifier in the event of a discharge between the sample and the PEEM objective lens we designed a surge protection circuit. We found that the best solution for a reliable protection circuit is to connect a combination of a 1 kV transient suppressor diode and a gas discharge tube to each output terminal of the high voltage amplifier. Figure 5.9 shows a detailed schematic the surge protection circuit.

The electromagnetic coil installed in the sample holder is driven using the constant current source integrated in the ELMITEC Sample Heater controller and a low voltage relay box allows for reversing the polarity of the magnetic field or through a home-built bipolar, ±3 A current amplifier. Typically, during an experiment the magnetic state of the sample is initialised using the electromagnet and then the electric field is swept in steps while acquiring images at each step to study how the application of the electric field affects the magnetic domain configuration.

References

[1] H. Hopster and H. P. Oepen, editors. *Magnetic Microscopy of Nanostructures*. NanoScience and Technology. Springer Berlin Heidelberg, 2005.

[2] E. Bauer. Photoelectron microscopy. *Journal of Physics: Condensed Matter*, 13(49): 11391, 2001.

[3] A. Locatelli and E. Bauer. Recent advances in chemical and magnetic imaging of surfaces and interfaces by xpeem. *Journal of Physics: Condensed Matter*, 20(9):093002, 2008.

[4] E. Bauer. *Surface Microscopy with Low Energy Electrons*. Springer-Verlag New York, 2014.

[5] Elmitec GmbH. PEEM III with analyzer. Website, April 2015.

[6] Th. Schmidt, A. Sala, H. Marchetto, E. Umbach, and H.-J. Freund. First experimental proof for aberration correction in XPEEM: Resolution, transmission enhancement, and limitation by space charge effects. *Ultramicroscopy*, 126(0):23 – 32, 2013.

[7] J. Stöhr. Exploring the microscopic origin of magnetic anisotropies with x-ray magnetic circular dichroism (xmcd) spectroscopy. *Journal of Magnetism and Magnetic Materials*, 200:470 – 497, 1999.

[8] G. van der Laan and A. I. Figueroa. X-ray magnetic circular dichroism: A versatile tool to study magnetism. *Coordination Chemistry Reviews*, 277–278(0):95 – 129, 2014.

[9] M. Sacchi and J. Vogel. *Magnetism and Synchrotron Radiation, Part I*, chapter Dichroism in X-ray Absorption, pages 87–108. Springer Berlin Heidelberg, 2001.

[10] J. Stöhr and H. C. Siegmann. *Magnetism: From Fundamentals to Nanoscale Dynamics*. Springer Berlin Heidelberg, 2006.

[11] U. Flechsig, F. Nolting, A. Fraile Rodriguez, J. Krempasky, C. Quitmann, T. Schmidt, S. Spielmann, and D. Zimoch. Performance measurements at the sls sim beamline. *AIP Conference Proceedings*, 1234(1):319–322, 2010.

[12] L. Le Guyader, A. Kleibert, A. Fraile-Rodriguez, S. El Moussaoui, A. Balan, M. Buzzi, J. Raabe, and F. Nolting. Studying nanomagnets and magnetic heterostructures with x-ray peem at the swiss light source. *Journal of Electron Spectroscopy and Related Phenomena*, 185(10):371 – 380, 2012.

[13] M. Buzzi, C. A. F. Vaz, J. Raabe, and F. Nolting. Electric field stimulation set-up for photoemission electron microscopes. *Rev. Sci. Inst.*, 86(083702), 2015.

[14] L. Heyne, M. Kläui, J. Rhensius, L. Le Guyader, and F. Nolting. In situ contacting and current-injection into samples in photoemission electron microscopes. *Review of Scientific Instruments*, 81(11):113707, 2010.

CHAPTER 6

Electric field induced magnetisation reorientations

This chapter deals with the results of two experiments that explore magnetoelectric coupling in micro- and nanopatterned strain mediated artificial multiferroics. This is followed by the discussion of the expected time scales in artificial multiferroics and the description of a preliminary experiment to probe ferroelectric switching on a sub-ns time scale[1].

6.1 Introduction

The continuously increasing demand for data storage systems that exhibit both high speed and low energy consumption has encouraged researchers to look for novel ways of manipulating and recording information. Magnetoelectric multiferroics, materials that show both a coexistence and a coupling of magnetic and ferroelectric ordering, are considered among the most promising materials for applications in spintronic devices due to the possibility of manipulating their magnetic state through the application of an electric field. However, single phase magnetoelectric multiferroic materials are rare [3] and, up to now, not suitable for the development of devices due to their low ordering temperatures or lack of strong magnetoelectric coupling. As described in section 2.3, one way of overcoming this limitation is to form a composite of two ferroic constituent materials,

[1] Parts of this chapter are adapted from: M. Buzzi, R. V. Chopdekar, J. L. Hockel, A. Bur, T. Wu, N. Pilet, P. Warnicke, G. P. Carman, L. J. Heyderman and F. Nolting, *Phys. Rev. Lett.* **111** 027204 [1], and M. Buzzi, C. A. F. Vaz, J. Raabe, F. Nolting, *Rev. Sci. Inst.* **86** 083702 (2015) [2].

such as a magnetostrictive ferromagnet and a piezoelectric ferroelectric, to obtain a strain-mediated artificial multiferroic.

In artificial multiferroics the choice of the ferroelectric and the ferromagnetic constituent has a key role in obtaining the desired magnetoelectric coupling. The discovery of non-volatile switchable strain states in (011) oriented 0.68 $Pb(Mg_{0.33}Nb_{0.66})O_3$ − 0.32 $PbTiO_3$ (PMN-PT) ferroelectric crystals makes this material a very interesting candidate for the ferroelectric constituent of strain-mediated artificial multiferroics [4]. Magnetostrictive metals, such as Ni, Co or CoFeB, or complex ferromagnetic oxides such as $La_{0.3}Sr_{0.7}MnO_3$ (LSMO) can be employed as a ferromagnetic constituent. Compared to magnetostrictive metals, complex oxides can display stronger variations of their magnetic properties when subjected to external stresses. It has been proven that changes in the epitaxial strain of $\approx \pm 1\%$ can affect significantly the orbital occupancy in LSMO [5] inducing strong variations in the magnetic anisotropy of the manganite layer [6]. The large, anisotropic piezostrain generated by (011) PMN – PT crystals has been already successfully employed to manipulate the magnetic anisotropy of continuous layers of LSMO [7], Fe_3O_4 [8], Ni [9] and CoFeB [10].

It has been proposed [11, 12] that electric field-induced magnetisation reorientations can play an important role in improving the performance of magnetic random access memories (MRAM) based on magnetic tunnel junctions [13]. At present, these devices permit facile read out of the encoded information via the tunnel magnetoresistance [14], but writing information to the device requires high magnetic fields or large current densities leading to a high energy consumption. Thus, employing magnetoelectric coupling for encoding information is of primary interest in order to build more efficient devices. Recently, an electric field-induced magnetisation reversal in CoFe / $BiFeO_3$ artificial multiferroic microstructures has been reported [15, 16]. However, the CoFe island is in a multi-domain magnetic state and the observed magnetic reorientation is only achieved with significantly different initial and final ferromagnetic domain configurations. For reproducible switching and device reliability it is desirable to induce a reorientation between two single domain states. It has been proposed that this can be achieved by manipulating the magnetic state of a single domain nanostructure by strain-driven magnetoelectric coupling [17]. A direct experimental proof, however, is still missing.

In the following, we present the first experimental proof of an electric field induced 90° uniform magnetisation reorientation in single-domain Ni elliptical nanostructures, which are strain coupled to a (011) PMN-PT ferroelectric crystal. The magnetisation in each Ni nanoisland rotates from the as-deposited in-plane easy axis defined by the shape anisotropy, to an in-plane orthogonal direction induced by the converse magnetoelectric interaction generated by piezoelectric strain. The initial and final magnetisation configurations are single domain as shown by X-PEEM measurements and as confirmed by micro-

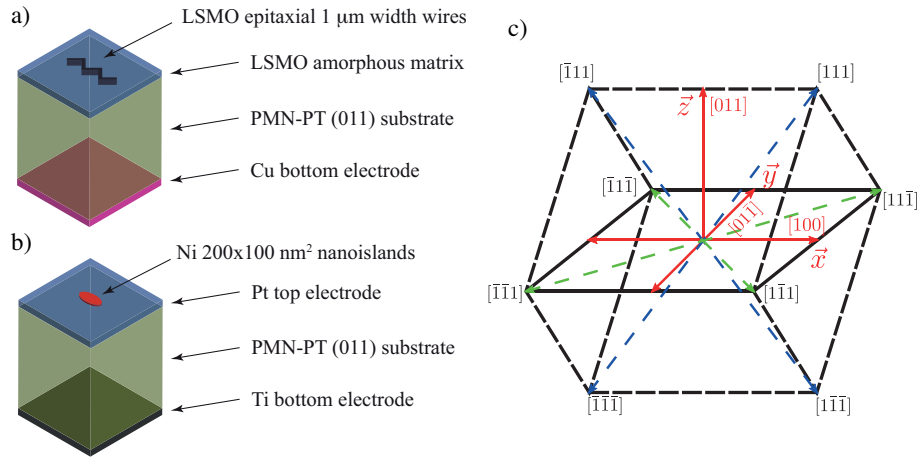

Figure 6.1: (a,b) Sketch of the finished sample structure with LSMO microwires and Ni nanoislands strain coupled to the PMN-PT ferroelectric substrate respectively. (c) Sketch of the rhombohedral crystal structure of PMN-PT highlighting out-of-plane (blue) and in-plane (green) equivalent polar axes. Adapted from [1] and [2]

magnetic simulations.

We will then present a preliminary experiment that investigates, in a similar manner, electric field induced changes in the magnetic domain structure of LSMO microwires also strain coupled to a (011) PMN-PT ferroelectric crystal. The observed changes suggest an electric field induced change in the magnetic anisotropy of the LSMO from a two-fold in-plane easy axis to a four-fold in-plane easy axis. However, different behaviours are observed in different areas of the sample suggesting the need of further optimisation of the patterning process.

6.2 Experimental Details

The samples employed for the two experiments described in this chapter consisted of Ni nanoislands (Fig. 6.1b) and $La_{0.33}Sr_{0.66}MnO_3$ microwires (Fig. 6.1a), lithographically defined on (011) oriented PMN-PT ferroelectric single crystals. The details about the growth and the patterning processes are given in chapter 4. The composition of PMN-PT used in this chapter is close to the morphotrophic phase boundary region of the niobate-titanate alloy [18] and its crystal structure is rhombohedral, with a ferroelectric polar axis along the ⟨111⟩ directions. Figure 6.1c shows a sketch of the crystal structure with [011] being the substrate normal direction.

The magnetic configuration of the nano- and micro-structures has been investigated by X-PEEM at the Surface/Interface: Microscopy (SIM) beamline of the Swiss Light Source

(SLS) [19]. Imaging of the magnetic state of the nanostructures was performed employing X-ray magnetic circular dichroism (XMCD), tuning the incoming photon energy to the Ni-L_3 edge ($\approx$ 852 eV) for the Ni nanoislands, and to the Mn-L_3 edge ($\approx$ 642 eV) for the LSMO microwires. The contrast in the XMCD image, as defined in chapter 5, is proportional to the scalar product $\vec{M}(\vec{r}) \cdot \vec{k}$, where $\vec{k}$ is the propagation vector of the incoming X-rays. In other words, the XMCD image shows black or white contrast in areas where magnetic moments have a component parallel or antiparallel to $\vec{k}$. To investigate the ferroelectric configuration of the PMN-PT ferroelectric crystals, Piezoresponse Force Microscopy (PFM) measurements have been performed at the NanoXAS beamline of the SLS [20].

All the samples were mounted as described in chapter 5. The electric field was applied across the PMN-PT crystal applying a bias voltage to the metallic bottom electrode and grounding either the Pt top electrode (for the Ni/PMN-PT heterostructure), or the amorphous LSMO matrix (for the LSMO/PMN-PT heterostructure). The source resistance of the voltage source was increased to 100 kΩ in order to limit the displacement current upon poling the ferroelectric crystal. This precaution was necessary to prolong the life of the crystal and avoid cracking.

6.3 Ni/PMN-PT artificial multiferroic nanostructures

To assess the as-grown magnetic configuration of the Ni nanostructures, we have performed investigations with no electric field applied to the sample. Figure 6.2 shows (a) a schematic of the experiment, (b) a sketch of a 4 by 3 array of 150×100 nm^2 ellipses with varying orientation, (c) the corresponding Ni elemental contrast and (d) the XMCD contrast image. The sample is imaged after applying a saturating magnetic field pulse of $\approx$ 0.3 T along the x-ray direction. The elemental contrast image, Figure 6.2c shows that Ni nanostructures are well isolated and can be clearly distinguished. If we assume that shape anisotropy is the dominant contribution to the overall magnetic anisotropy of the islands, the left column of the array of structures should have an expected magnetic easy-axis perpendicular to the X-ray direction, whereas the right column should have magnetisation oriented parallel to the X-ray direction. Indeed, the islands with long axis perpendicular to the X-ray propagation direction give in the XMCD image a grey contrast not distinguishable from the background that indicates that their magnetisation is perpendicular to $\vec{k}$. In comparison, the ellipses elongated along the X-ray $\vec{k}$ vector appear white since their magnetisation is uniformly aligned with $\vec{k}$ and thus have maximum XMCD. Thus, for 10 nm thick Ni 150×100 nm^2 islands the long axis then determines the easy magnetisation direction of the nanostructures due to the shape anisotropy.

To investigate the magnetoelectric interaction effects we have imaged the magnetisation configuration of an array of equally oriented 200×100 nm^2 ellipses while varying the

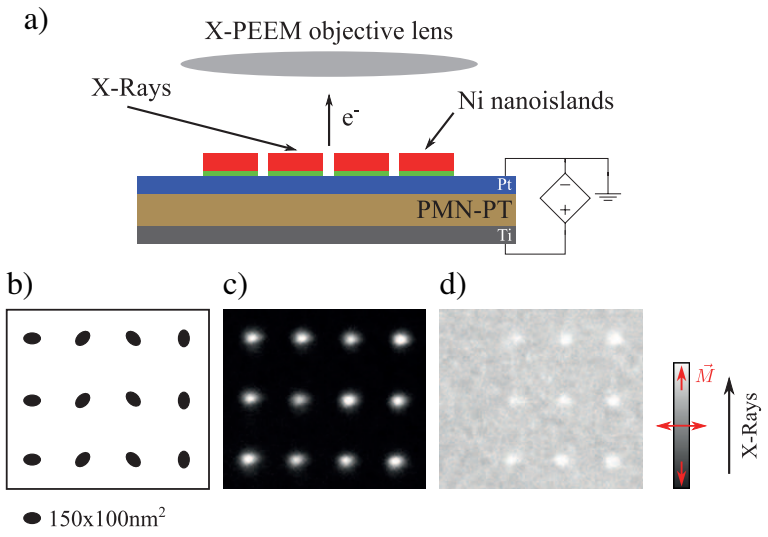

Figure 6.2: (a) Schematic of the experiment (not to scale). (b) Schematic of the imaged area with $150 \times 100\,\mathrm{nm}^2$ nanoislands in four different orientations, with the ellipse long axis at 90°, -45°, 45°, 0° with respect to the x-ray direction. (c) X-PEEM elemental contrast image, and corresponding (d) XMCD image at Ni L_3 edge after magnetic saturation of the sample. Adapted from [1]

applied electric field from $0\,\mathrm{MV\,m^{-1}}$ to $0.27\,\mathrm{MV\,m^{-1}}$ as shown in figure 6.3a, and plot the quantitative XMCD intensity as a function of the applied electric field in figure 6.3b for all the ellipses showing a permanent change during the electric field sweep. Before the experiment, the sample is initially poled at $-0.4\,\mathrm{MV\,m^{-1}}$ and magnetically randomised using a 50 Hz damped sinusoid magnetic field pulse with an amplitude varying from 30 mT to 0 mT. All the ellipses in the array have their long axis parallel to the $[01\bar{1}]$ direction of the ferroelectric crystal and parallel to the X-ray propagation direction. The XMCD image acquired at $0\,\mathrm{MV\,m^{-1}}$ shows that the islands appear uniformly magnetised either parallel (black) or antiparallel (white) to the long axis of the ellipses. We find that by increasing the applied electric field no changes are seen until the ferroelectric coercive electric field, $E_c = 0.15\,\mathrm{MV\,m^{-1}}$, is reached [4]. As we approach E_c, three different type of magnetic behaviour are observed, as highlighted in figure 6.3a. (i) For the ellipses circled in blue, the magnetic contrast from the nanoislands drops from the original value to zero, indicating that the magnetisation of the ellipses have rotated away from the long axis and now lie parallel to the ellipse short axis. By increasing the electric field up to $0.27\,\mathrm{MV\,m^{-1}}$, no changes in the magnetic configuration are observed. (ii) The ellipses highlighted with green triangles show a different behaviour. After undergoing the 90° reorientation at E_c, when the applied electric field is increased further the magnetisation relaxes back to one of the two equivalent directions parallel to the shape anisotropy easy axis. (iii) Finally, ellipses highlighted

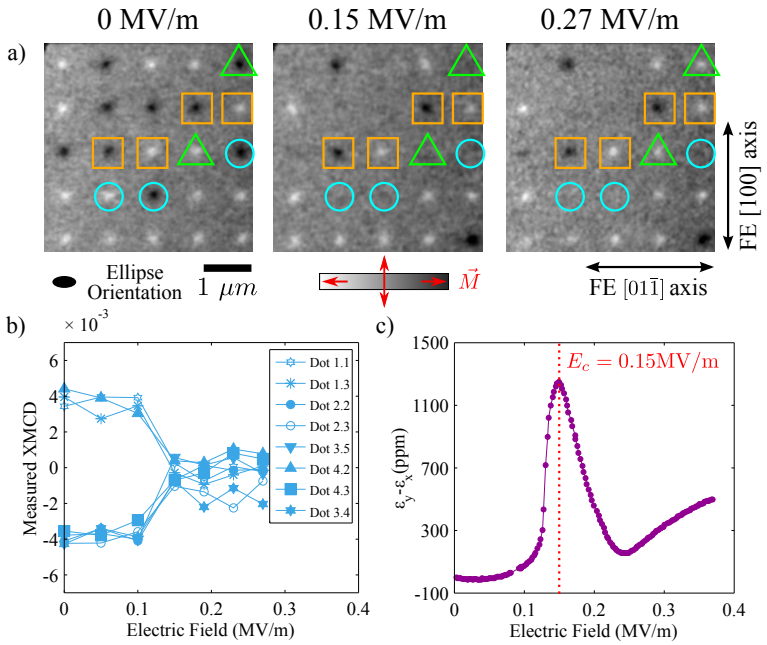

Figure 6.3: (a) Sequence of successive XMCD images of 200 × 100 nm^2 ellipse array recorded at the Ni-L_3 edge at different applied electric fields. (b) XMCD contrast as a function of the applied electric field curve for selected dots labeled in (row, column) format in panel (a). (c) In-plane strain vs. applied electric field curve measured with a strain gauge fixed on the sample after poling. Adapted from [1]

with orange squares do not show any change for any value of the applied electric field.

It can be excluded that the observed reduction of magnetic contrast which we observe at E_c is due to an imaging artefact as a result of the applied electric field since the orange-highlighted dots in the array do not show any change for any of the applied electric fields. Figure 6.3b shows that the drop in magnetic contrast observed when the applied electric field is equal to E_c can be correlated to the corresponding increase in the induced strain in the Pt film and magnetic nanostructures shown in figure 6.3c. We propose that the observed electric field-induced magnetisation reorientation can be explained by strain mediated magnetoelectric coupling which causes the magnetisation to reorient as a result of the competition of shape anisotropy and magnetoelastic contributions induced by the ferroelectric distortions. SEM measurements have shown that the different nanoislands have similar morphology and that variations in their aspect ratio are negligible. This, together with the observation that each of the nanoislands show the same magnitude of XMCD in the randomised state at 0 MV m^{-1}, suggests that the nanostructures should show an identical magnetic behaviour. Thus, the observation of these three different types of behaviour suggests that there are three different regimes of strain coupling. This can be ex-

plained, as follows, with a more detailed analysis which takes into account how the strain is generated in the magnetic nanostructures as the ferroelectric polarisation is reversed.

As shown in figure 6.2b the FE polarisation can be oriented along any of the 8 possible directions: 4 in the $(01\bar{1})$ plane (blue dashed lines, FE axis with a component along the surface normal) and 4 in the (011) plane (green dashed lines, FE axis fully in the plane of the sample). As already reported elsewhere [4] the polarisation reversal after poling along the [011] direction happens with two subsequent 71°-109° rotations starting from the equivalent two out-of-plane diagonals pointing in the poling direction. When the applied electric field is equal to E_c the polarisation rotates to lie along one of the four possible in-plane orientations, causing a strong expansion of the FE structure along the $[01\bar{1}]$ and [100] directions. By further increasing the electric field the FE polarisation will undergo the second 71°-109° rotation to an opposite out-of-plane diagonal completing the reversal and reducing the structural distortion to the value solely caused by electrostriction due to the applied electric field. If the electric field is then removed, the FE axis remains along the reversed [111] direction and the initial in-plane lattice dimensions are recovered.

Let us first analyse how the magnetic energy balance of a nanoisland changes when the ferroelectric polarisation is reversed. Figure 6.3c shows the in-plane strain vs. electric field curve measured by a strain gauge fixed to the Pt top contact on the PMN-PT crystal while switching the ferroelectric polarisation after poling along the [011] direction[2]. This situation corresponds to a nanoisland grown on an out-of-plane poled FE crystal. Since the Ni ellipses are polycrystalline, no magnetocrystalline anisotropy contributions are expected and the two competing terms are the shape anisotropy and the magnetoelastic energy due to the applied strain by the piezoelectric. As the strain generated by the PMN-PT ferroelectric crystal along the [100] and $[01\bar{1}]$ directions is anisotropic, the magnetoelastic energy term for Ni can be written as:

$$U_{me} = -(3/2)\lambda_p Y(\varepsilon_{01\bar{1}} - \varepsilon_{100})\cos^2(\theta_{01\bar{1}}) \tag{6.1}$$

where $\lambda_p = -34$ppm is the magnetostriction coefficient for polycrystalline nickel [21], $Y =$ 220GPa is the Young modulus of nickel [22], $(\varepsilon_{01\bar{1}} - \varepsilon_{100})$ the applied strain by the piezoelectric and $\theta_{[01\bar{1}]}$ the angle between the magnetisation and the $[01\bar{1}]$ direction of the FE. For an ellipse with the long axis oriented along $[01\bar{1}]$, positive values of $(\varepsilon_{01\bar{1}} - \varepsilon_{100})$ will act against shape anisotropy favouring a reorientation of the magnetisation to the [100]. According to finite elements magnetostatic calculations using the NMAG code [23], for the $200 \times 100\,\mathrm{nm}^2$ Ni nanostructures shown in figure 6.3a with 2:1 ratio between the long and short in plane axis, the magnetostatic energy barrier to be overcome for inducing the rotation to the short axis is $\approx 10\,\mathrm{kJ\,m^{-3}}$. When the polarisation of the FE is switched, the

[2]The strain-gauge measurements were performed by Tao Wu at the Department of Mechanical and Aerospace Engineering, University of California-Los Angeles, USA.

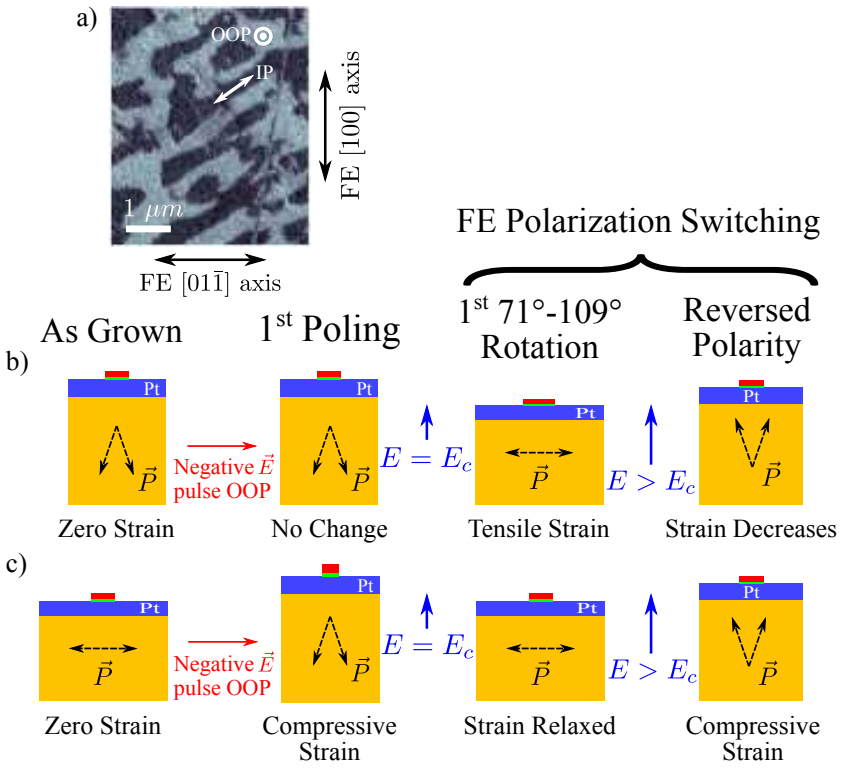

Figure 6.4: (a) PFM image of the out-of-plane piezoelectric response of the PMN-PT crystal. FE domain orientations are indicated by the out-of-plane (OOP) and in-plane (IP) white arrows in the image. (b,c) Strain behaviour, during FE polarisation reversal for a dot deposited on an out-of-plane and in-plane polarized FE domain respectively. Adapted from [1]

quantity $(\varepsilon_{01\bar{1}} - \varepsilon_{100})$ jumps to ≈ 1300 ppm. This generates a Ni magnetoelastic contribution of about 15 kJ m^{-3}, which is sufficient to overcome the magnetostatic energy barrier and to induce the 90° magnetisation reorientation.

The three different behaviours of the nanoislands described above can be understood by taking into account the underlying FE domain structure of the crystal when the Ni structures are deposited. This is supported by PFM measurements taken on an identical PMN-PT crystal (they could not be performed on the fully fabricated sample used for the PEEM experiment due to the presence of the Pt top electrode preventing retrieval of the PFM contrast). Figure 6.4a shows the presence of alternating in-plane and out-of-plane domains, with FE axis along any of the eight ⟨111⟩ type directions. The domain length scale is ≈1 μm which is comparable to the ellipse spacing in the array of figure 6.3a and is ≈5 times larger than the ellipse size. It is then reasonable to assume that a significant amount of nanoislands lay on a single FE domain, although adjacent ellipses may be on domains

with different FE orientations or even on top of a FE domain boundary between different FE orientations. Since the Ni ellipses are polycrystalline, the zero value of the Ni internal strain depends on the substrate distortion at the deposition time. Let us first consider the case presented in figure 6.4b of a nanostructure deposited on an out of plane FE domain. In this case, the Ni is deposited on an area of the FE in which the polarisation is already pointing out of the (011) plane and the first macroscopic poling, applying a field along [011] before the measurement, will not modify the distortion of the structure. When $E \approx E_c$, the first 71°/109° FE polarisation rotation to the in-plane polar axes will cause the FE structure to expand along the main in-plane directions. This generates a tensile strain in the Ni nanostructure which, as explained above, triggers the magnetisation reorientation. This single-step magnetisation reorientation is the behaviour shown by the blue-circled ellipses in figure 6.3a. In figure 6.4c, we consider a nanoisland deposited on an in-plane poled domain. The Ni is deposited on an area polarised in the (011) plane and the FE crystal underneath the ellipse is already elongated along the [100] and [01$\bar{1}$] directions. At the first poling along the [011] direction, the polarisation in this domain will rotate out-of-plane, causing a strong compressive strain in the Ni nanostructure which will act to favour further the easy axis induced by the shape anisotropy. Cycling the electric field will only relax the effective compressive strain in the magnetic ellipse and no reorientation will happen regardless of the applied electric field, which explains the magnetic behaviour shown by the ellipses marked by an orange square. Finally, let us now consider the case of the ellipses marked by a green triangle in which the magnetisation relaxes back to the shape anisotropy easy axis for $E > E_c$. After the strain maximum at E_c, the strain starts to decrease down to ≈ 200 ppm, as shown in figure 6.3c. In the case of the blue-circled ellipses the magnetoelastic contribution is sufficient to keep the magnetisation perpendicular to the shape anisotropy induced easy axis. However, if the local strain of the nanostructure is lower, for example because the nanoisland is lying on the boundary between two different FE domains, the strain mediated magnetoelectric coupling will be weaker and at $0.27\,\mathrm{MV\,m^{-1}}$ the magnetoelastic contribution might not be strong enough to prevent the relaxation back towards to the shape anisotropy easy axis.

To confirm the proposed interpretation we have carried out micromagnetic simulations using the NMAG code in the approximation of a uniformly applied strain to the $200 \times 100\,\mathrm{nm^2}$ ellipse elongated along the [01$\bar{1}$] direction of the ferroelectric. Islands grown on both out-of-plane and in-plane ferroelectric domains have been simulated. The initial spin configuration of the system at $0\,\mathrm{MV\,m^{-1}}$ is achieved by relaxing the magnetisation configuration starting from a randomly magnetised state in the absence of magnetoelastic anisotropy and applied magnetic field. As indicated by the X-PEEM measurement, the obtained equilibrium magnetisation configuration, shown in figure 6.5a upper left panel, is single domain and uniformly magnetised along the shape anisotropy-

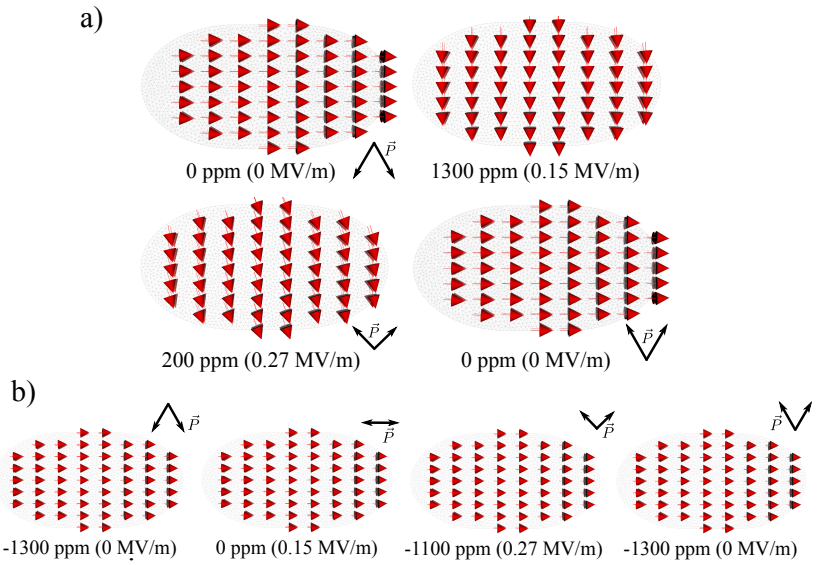

Figure 6.5: Simulated magnetization profiles at 0 MV/m, 0.15MV/m, 0.27 MV/m and back to 0 MV/m for a nanostructure deposited on (a) an out-of-plane (OOP) polarized FE domain and (b) on an in-plane (IP) polarized FE domain. Arrows schematically indicate the ferroelectric polarization directions of the PMN-PT crystal. Adapted from [1]

induced easy axis. The experimental electric field effect is simulated by varying the anisotropy constant according to the corresponding strain value for the electric field derived from figure 6.3c. The behaviour of the magnetisation parallel to the ellipse long axis as a function of the strain is then obtained and compared with the measured XMCD contrast. In order to match the experimental observations we have tuned the Ni saturation magnetisation M_s to 0.33 T ($\approx$ 55% of the bulk value). To ensure that the reduced M_s value is not caused by an oxidation of the Ni layer, we have carried out x-ray spectromicroscopy on individual nanoislands. As shown in the x-ray absorption spectrum in figure 6.6, no oxide peak can be observed indicating that no significant oxidation layer is present at the surface of the nanostructures [24]. Even though we cannot exclude some residual oxidation at the nanoislands edges, we believe that the reduction of M_s needed in the simulations is caused by an underestimated strain value due to approximating the local strain with a macroscopically-averaged strain gauge value.

Figure 6.5a shows the evolution of the simulated magnetic configuration from $0\,\mathrm{MV\,m^{-1}}$ applied electric field to $0.15\,\mathrm{MV\,m^{-1}}$, $0.27\,\mathrm{MV\,m^{-1}}$ and then back to $0\,\mathrm{MV\,m^{-1}}$ for an ellipse grown on an out-of-plane FE domain. The simulation confirms the experimentally observed 90° uniform magnetisation rotation that occurs at $0.15\,\mathrm{MV\,m^{-1}}$ from the shape anisotropy-induced easy axis to the one induced by the strain-mediated magnetoelectric interaction. The magnetisation at $0.27\,\mathrm{MV\,m^{-1}}$ reverts back towards the

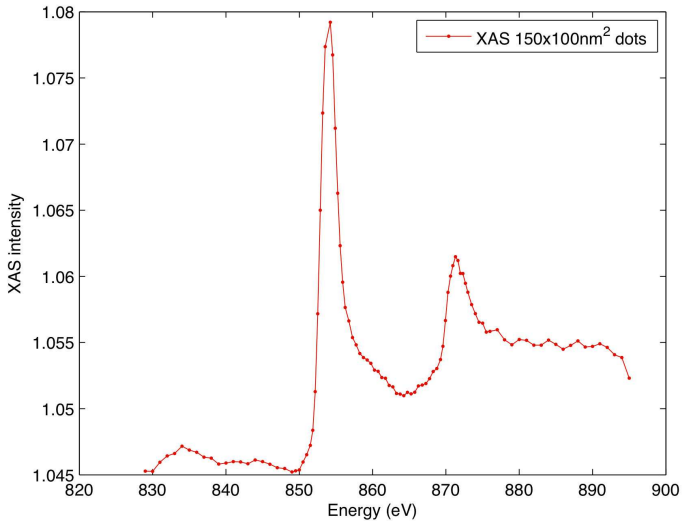

Figure 6.6: XAS spectrum on a single nanoisland at the Ni $L_{2,3}$ edges showing no oxidation.

original direction but the angular change is only $\approx 7°$ which is within the noise of our XMCD experiment. The change in applied electric field from 0.15 MV m^{-1} to 0.27 MV m^{-1} reduces the strain to a minimum (Fig. 6.3c), and, at this point, any variation in the strain behaviour, caused for example by the presence of a FE domain wall or defect, could cause the magnetisation to relax back completely to the shape anisotropy-dictated easy axis. Finally, when the field is brought back to 0 MV m^{-1} the magnetisation relaxes back to the original configuration. Figure 6.5b shows the results of the simulation for a nanoisland grown on an in-plane FE domain. In this case, the only effect of the magnetoelastic interaction is to further stabilise the already easy direction induced by the shape anisotropy. As a consequence, no magnetic reorientation takes place.

The effective magnetoelectric coefficient obtained by the full rotation of the magnetisation in the nanostructure can be calculated as:

$$\alpha_e = \mu_0 \frac{\Delta M}{\Delta E} \tag{6.2}$$

where ΔM is the change of magnetisation induced by a change of the applied electric field ΔE. Substituting the values for this experiment, $\Delta M = 2.63 \times 10^5$ A m^{-1} and $\Delta E = 1.5 \times 10^5$ V m^{-1} one obtains $\alpha_e = 2.2\,\mu$s m^{-1}, approximately 5 orders of magnitude higher than Cr_2O_3 and among the highest magnetoelectric coefficients reported so far [25].

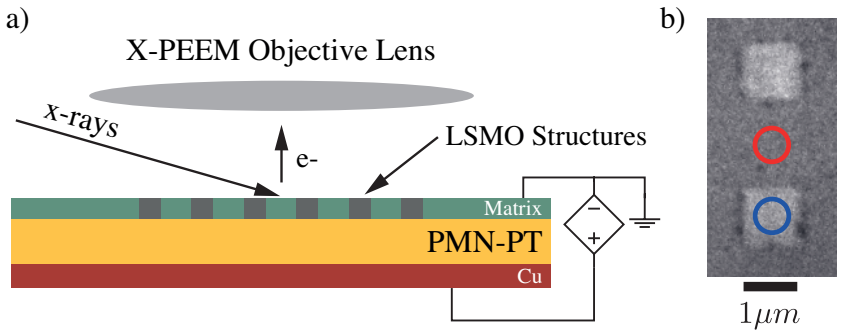

Figure 6.7: (a) Schematic of the experiment (b) Mn L_3 elemental contrast image of an array of two LSMO 1 µm squares.

6.4 LSMO/PMN-PT artificial multiferroic microstructures

Following the procedure employed in the previous experiment, we have performed investigations with no electric field applied to the sample in order to assess the as-grown magnetic configuration of the LSMO microstructures. As anticipated in chapter 4 the patterning process results in LSMO epitaxial structures within an amorphous LSMO matrix. Figure 6.7 shows (a) a schematic of the experiment, and (b) a Mn L_3 elemental contrast image of an array of LSMO 1 µm squares. The quality of the patterning is satisfactory with some leftover Cr clusters that appear as black agglomerates at the edges of the structures. However, no magnetic contrast could be observed in the XMCD image even at a reduced sample temperature of 250 K.

To investigate the possible cause for the absence of magnetic contrast in the 1 µm squares, x-ray spectro-microscopy was performed on the amorphous matrix and on the inner part of the squares in order to assess the correct valence state of the LSMO layer. Figure 6.8 shows the x-ray absorption spectrum for the inside of the microstructure (blue curve) and the amorphous matrix (red curve). As described in chapter 4, LSMO should contain only Mn^{3+} and Mn^{4+}, however both spectra show the presence of a sharp peak, highlighted with an arrow in figure 6.7, that can be attributed to Mn^{2+}. This suggests the presence of oxygen deficiency that may have arisen either during the Ar ion irradiation used for the patterning, or during the growth process. Oxygen deficiency is known to strongly affect the electronic and magnetic properties of LSMO, thus we can speculate that this is likely to be the cause of the absence of a magnetic contrast in these structures.

However, larger structures showed magnetic contrast. Figure 6.9 shows a series of XMCD images acquired at three different applied electric fields 0 MV/m, 0.15MV/m, 0.27MV/m for three different LSMO microwires (a, b, c). The XMCD sequence was recorded with no applied magnetic field after poling the ferroelectric at $-0.5\,\mathrm{MV\,m^{-1}}$ and

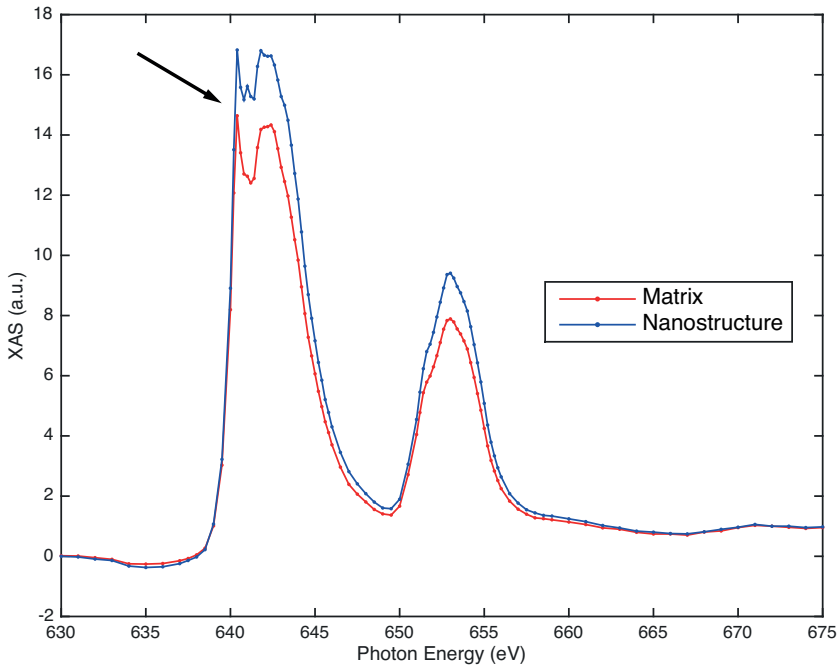

Figure 6.8: XAS spectrum of an LSMO 1 µm square (blue) compared with the matrix (red). The spectra are obtained from the area of interests defined in figure 6.7b.

applying a 15 mT magnetic field pulse along the x-ray propagation direction. Firstly, the magnetic domain configuration at 0 MV m^{-1} applied field for the wires in figure 6.9a, b is considered. The wire segments extending along the [100] direction show a uniform black XMCD contrast indicating that they are uniformly magnetised. The traces of smaller magnetic domains can be observed in the segments extending along the [01$\bar{1}$] direction. This suggests that when the ferroelectric polarisation of the PMN-PT crystal lies out of the (011) plane, the [100] axis is an easy magnetisation axis while the [01$\bar{1}$] is a harder one. When the electric field is increased to 0.15 MV m^{-1}, the PMN-PT induces an anisotropic strain, as described above, and the wire segments oriented along [01$\bar{1}$] also acquire a uniform black contrast suggesting that both the [100] and [01$\bar{1}$] directions are now easy magnetisation directions. However, that the wire in figure 6.9c shows the opposite behaviour. In zero applied electric field, the [100] and [01$\bar{1}$] crystallographic axes are both easy magnetisation directions, while the [01$\bar{1}$] direction becomes a hard magnetisation direction when the field is increased to 0.15 MV m^{-1}. No further changes for all the wires are observed when the applied electric field is increased to 0.27 MV m^{-1}.

In contrast to what has been presented in the previous section for the Ni nanostructures on PMN-PT, the LSMO layer is epitaxial to the PMN-PT and the deposition of the

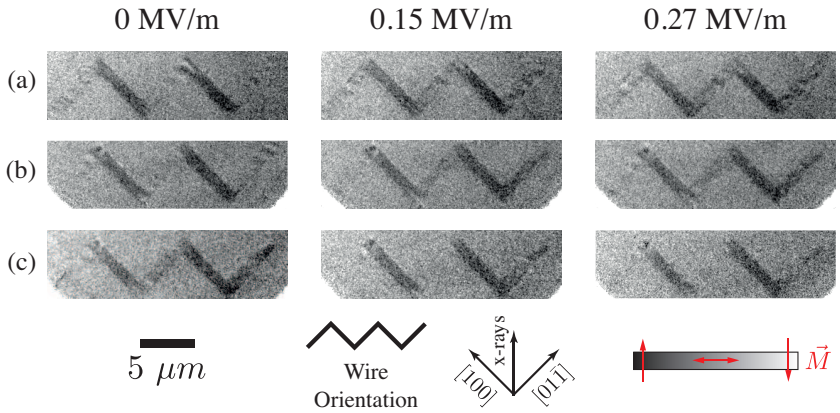

Figure 6.9: XMCD images for three different LSMO microwires at three different applied electric fields 0 MV/m, 0.15MV/m, 0.27MV/m. Adapted from [2]

LSMO is performed at an elevated temperature in which PMN-PT is paraelectric. We can therefore exclude the presence of different strain dynamics due to the ferroelectric domain structure at the deposition time. It is possible that the backscattering of the Ar ion by the substrate was strong enough to cause localised damage also in the Cr masked areas, thus inducing local modifications of the magnetic properties in the LSMO layer. To overcome this problem, a less aggressive patterning could be achieved by using a subtractive etching technique as recently shown in [26].

6.5 Timescales in artificial multiferroics

In the perspective of applications in data recording, it is important to investigate the ultimate operation speed of artificial multiferroic heterostructures. In these systems one relies on the switching of the ferroelectric component to induce changes in the ferromagnetic layer as shown above. After considering what limits the ultimate speed at which each component of an artificial multiferroic can be manipulated, a preliminary experiment to determine the switching speed of a patterned ferroelectric capacitor is presented.

In artificial multiferroics the time scale of the induced magnetoelectric coupling is ultimately defined, on the one hand, by the speed at which both the ferroelectric and ferromagnetic components can be manipulated, and on the other, by the origin of the coupling mechanism between the two. Ferromagnetic switching happens either by (i) a uniform rotation of the magnetisation, or by (ii) the nucleation of reversed domains and propagation of domain walls. The first process is typical in nanostructures that are in a single domain state. In this case, as the magnetisation rotates coherently, the switching time scale is determined by precessional motions and varies between 0.1 ns to 1 ns [27]. The second pro-

cess is favoured in extended systems such as continuous thin films where multi domain configurations are favoured. In this case the switching process is slower and is limited by the domain wall velocity which for soft materials varies between 100 m s^{-1} to 600 m s^{-1}, like in $Ni_{0.8}Fe_{0.2}$ [27]. For ferroelectrics the switching mechanisms are more complex since the polarisation reversal involves structural changes, requiring the minimisation of both the electrostatic and elastic energy. Also, ferroelectric domain walls tend to be strongly pinned and the switching speed is normally limited by their slow propagation. Typical propagation speeds for these walls are below 100 m s^{-1} as confirmed by time resolved x-ray diffraction experiments [28]. In relaxor ferroelectrics, dielectric relaxation phenomena can be responsible for very slow responses of the ferroelectric material to applied electric fields, as recently shown for PMN-PT [29][3].

The origin of the coupling between the ferroelectric and the ferromagnetic constituents also has an important role in determining the ultimate time scale related to magnetoelectric coupling. In case of strain mediated artificial multiferroics the distortions generated by the ferroelectric have to propagate to the ferromagnetic layer. This is analogous to the propagation of a sound wave in the materials, so it is expected to be limited by the speed of sound in solids $\approx$1 km s^{-1}. In the case of charge and exchange mediated artificial multiferroics the coupling can be faster. In the former case it is determined by the dielectric relaxation time in the ferromagnetic constituent which is $\approx$ 1 ps. In the latter, the coupling is limited by how fast the ferromagnetic constituent follows the reorientation of the antiferromagnetic ferroelectric. Recent experiments have shown that partial reorientations in ferromagnetic layers coupled to antiferromagnets can occur at an ultrafast pace ($\approx$ 100 ps) [30].

When the electric field is applied via electrodes connected to a pulsed voltage source, the RC time constant of the multiferroic device also limits its response speed. Typically, planar electrodes are deposited on the opposite faces of the ferroelectric, thus one can easily calculate the capacitance C of the multiferroic device as:

$$C = \epsilon_0 \epsilon_r \frac{A}{t} \tag{6.3}$$

where ϵ_0 is the permittivity of free space, ϵ_r is the dielectric constant of the ferroelectric, A is the surface of the contacts and t the thickness of the ferroelectric constituent. In the case of the experiment presented in section 6.3, $\epsilon_r \approx 3000$ [4], $A = 10 \times 10$ mm^2, $t = 0.5$ mm giving a capacitance $C = 6$ nF. To prevent damages to the ferroelectric crystal while switching its polarisation, the electric field is applied with a resistor R =100 kΩ. The RC time constant is in this case $\approx$ 600 µs, well above the limitations dictated by the ferromagnetic switching but still below the typical relaxation times in relaxor ferroelectrics.

Substituting the ferroelectric single crystal with a thin ferroelectric layer relaxes the

[3]This paragraph follows from the description given in [25]

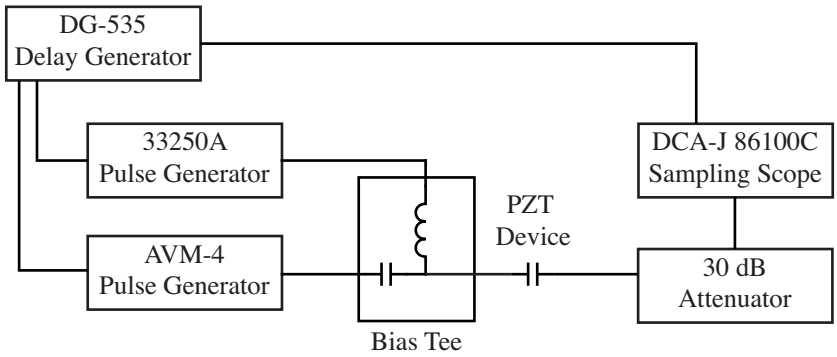

Figure 6.10: Schematic of the experiment for measuring the fast switching behaviuor of a PZT capacitor.

requirements on the series resistor, allowing to maintain R around a value of 50 Ω. By laterally confining the area of the multiferroic device and by employing a non-relaxor ferroelectric with a lower dielectric constant, one can significantly reduce the RC product and the dielectric relaxation time to below the ferroelectric switching time. For example, $PbZr_{0.2}Ti_{0.8}O_3$ (PZT) thin films show a sub-100 ps dielectric relaxation time with $\epsilon_r \approx 250$ [31]. For $A = 20 \times 20\,\mu m^2$, $t = 0.26\,\mu m$ one obtains a capacitance $C = 3.5$ pF and a time constant $RC = 175$ ps. This value is well below the ferroelectric switching time of PZT thin layers, which is estimated to be sub-100 ns as observed by time-resolved piezoresponse force microscopy measurements [32].

Figure 6.10 shows the schematic of an experiment aiming at observing the fast switching behaviour of a commercial 260 nm thick PZT device with $20 \times 20\,\mu m^2$ lateral dimensions. Details about the sample structure are reported elsewhere [33]. Similar to what was implemented in [34], an Agilent DCA-J 86100C sampling scope is used to monitor the polarisation switching response, allowing a time resolution up to 50 ps. A DG-535 delay generator from Stanford Research System is used to trigger the sampling scope, as well as the two pulse generators used for the polarisation switching at a 10 Hz repetition rate. An Avtec AVM-4 high speed pulse generator generates the switching pulse, while a delayed 10ms long reset pulse is generated by an Agilent HP-33250A waveform generator. The ferroelectric capacitor is terminated on one side via a 30dB, 50 ohm attenuator to the input of the sampling scope while the other side is connected to a bias tee. The purpose of the bias tee is to electrically separate the two pulse generators. In this setup, the signal measured by the sampling scope is directly the displacement current. The paraelectric contributions, proportional to $C(dV/dt)$, were disentangled from the ferroelectric switching signal by recording two different time traces. In the first trace ($i_{\text{no-switching}}$) the reset pulse has the same polarity as the switching pulse (i.e. no ferroelectric polarisation switching happens),

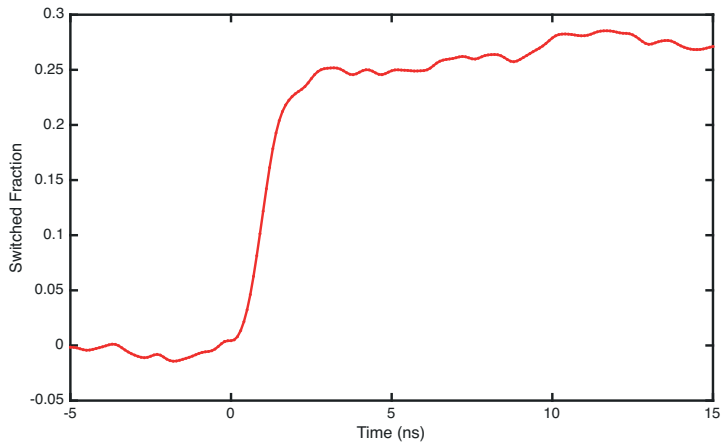

Figure 6.11: Evolution of the switched fraction of the ferroelectric polarisation in the patterned PZT device.

while in the second trace ($i_{\text{switching}}$) the two pulses have opposite polarity. The saturation polarisation of this PZT device was $\approx 40\,\mu\text{C}\,\text{cm}^{-2}$ with a coercive field of $80\,\text{kV}\,\text{cm}^{-1}$ as measured with a low frequency PUND measurement [33].

Figure 6.11 shows the evolution of the switched fraction of the ferroelectric polarisation of the patterned PZT device upon the application of a $400\,\text{kV}\,\text{cm}^{-1}$ electric field pulse with a FWHM duration of 500 ps. The change in the electric polarisation of the ferroelectric at the time t is obtained as follows:

$$\Delta P(t) = \int_{-\infty}^{t} i_{\text{switching}}(t') - i_{\text{no-switching}}(t')\,\mathrm{d}t' \tag{6.4}$$

where $i_{\text{switching}}$ and $i_{\text{no-switching}}$ are the time traces acquired as defined above. The switched fraction is defined as the ratio between the detected change in polarisation $\Delta P(t)$, and the saturation polarisation of the PZT device measured at low frequency. It is interesting to note that although the response of ferroelectric capacitor is relatively fast (a risetime of $\approx$ 1.5 ns can be extracted by the time trace), only $\approx$25% of the PZT device has switched, suggesting that a significantly longer pulse is needed to achieve full ferroelectric switching as previously reported [32].

6.6 Conclusions and outlook

The first experiment has demonstrated the possibility of inducing a 90° uniform magnetisation rotation by the application of an electric field in Ni strain coupled artificial mul-

tiferroic nanostructures, resulting in one of the highest magnetoelectric coupling coefficient measured so far. We have found that the complex domain structure of the ferroelectric single crystal exerts a strong influence on the strain mediated magnetoelectric coupling, suggesting the importance of optimised and reliable patterning techniques for complex ferroelectric and ferromagnetic oxides in order to realise the full magnetoelectric stack at the nanoscale [1]. The second experiment aimed at exploring how the magnetic anisotropy of strain-coupled LSMO microwires can be modified by the application of electric fields [2]. Despite the issues with the patterning process, it was possible to observe a change of the magnetic anisotropy from two-fold to four-fold. In both cases, thanks to the hysteretic strain dynamics of the FE material [17], the effect can be non volatile and reversible, constituting an important step towards the realisation of a magnetoelectric MRAM cell.

As discussed in section 6.5 ferroelectric switching in displacive ferroelectrics appears to be slower than magnetisation switching in ferromagnets. One could tailor the ferromagnetic nanostructure so that the switching between different magnetisation states can be obtained by short strain pulses. These strain pulses can be generated by relying only on the linear piezostrain arising as the ferroelectric is excited with an electric field pulse. This may allow for the realisation of faster devices where no propagation of ferroelectric domain walls is involved.

References

[1] M. Buzzi, R. V. Chopdekar, J. L. Hockel, A. Bur, T. Wu, N. Pilet, P. Warnicke, G. P. Carman, L. J. Heyderman, and F. Nolting. Single domain spin manipulation by electric fields in strain coupled artificial multiferroic nanostructures. *Phys. Rev. Lett.*, 111: 027204, 2013.

[2] M. Buzzi, C. A. F. Vaz, J. Raabe, and F. Nolting. Electric field stimulation set-up for photoemission electron microscopes. *Rev. Sci. Inst.*, 86(083702), 2015.

[3] N. A. Hill. Why are there so few magnetic ferroelectrics? *The Journal of Physical Chemistry B*, 104(29):6694–6709, 2000.

[4] T. Wu, P. Zhao, M. Bao, A. Bur, J. L. Hockel, K. Wong, K. P. Mohanchandra, C. S. Lynch, and G. P. Carman. Domain engineered switchable strain states in ferroelectric (011) $(1-x)$PbMg$_{1/3}$Nb$_{2/3}$O$_3$–(x)PbTiO$_3$ (PMN-PT, $x \approx 0.32$) single crystals. *Journal of Applied Physics*, 109(12):124101, 2011.

[5] D. Pesquera, G. Herranz, A. Barla, E. Pellegrin, F. Bondino, E. Magnano, F. Sánchez, and J. Fontcuberta. Surface symmetry-breaking and strain effects on orbital occupancy in transition metal perovskite epitaxial films. *Nat. Commun.*, 3:1189, 2012.

[6] P. Perna, C. Rodrigo, E. Jiménez, F. J. Teran, N. Mikuszeit, L. Méchin, J. Camarero, and R. Miranda. Tailoring magnetic anisotropy in epitaxial half metallic $La_{0.7}Sr_{0.3}MnO_3$ thin films. *Journal of Applied Physics*, 110(1):013919, 2011.

[7] Y. Yang, M. Meng Yang, Z. L. Luo, H. Huang, H. Wang, J. Bao, C. Hu, G. Pan, Y. Yao, Y. Liu, X. G. Li, S. Zhang, Y. G. Zhao, and C. Gao. Large anisotropic remnant magnetization tunability in (011) $La_{0.33}Sr_{0.66}MnO_3$/0.7Pb($Mg_{0.66}Nb_{0.33}$)O_3-0.3$PbTiO_3$ multiferroic epitaxial heterostructures. *Applied Physics Letters*, 100:043506, 2012.

[8] M. Liu, O. Obi, J. Lou, Y. Chen, Z. Cai, S. Stoute, M. Espanol, M. Lew, X. Situ, K. S. Ziemer, V. G. Harris, and N. X. Sun. Giant electric field tuning of magnetic properties in multiferroic ferrite/ferroelectric heterostructures. *Advanced Functional Materials*, 19(11):1826–1831, 2009.

[9] T. Wu, A. Bur, P. Zhao, K. P. Mohanchandra, K. Wong, K. L. Wang, C. S. Lynch, and G. P. Carman. Giant electric-field-induced reversible and permanent magnetization reorientation on magnetoelectric Ni / (011) $PbMg_{1/3}Nb_{2/3}O_3$-$PbTiO_3$ heterostructure. *Applied Physics Letters*, 98(1):012504, 2011.

[10] S. Zhang, Y. G. Zhao, P. S. Li, J. J. Yang, S. Rizwan, J. X. Zhang, J. Seidel, T. L. Qu, Y. J. Yang, Z. L. Luo, Q. He, T. Zou, Q. P. Chen, J. W. Wang, L. F. Yang, Y. Sun, Y. Z. Wu, X. Xiao, X. F. Jin, J. Huang, C. Gao, X. F. Han, and R. Ramesh. Electric-field control of nonvolatile magnetization in $Co_{40}Fe_{40}B_{20}$ / 0.3$PbMg_{1/3}Nb_{2/3}O_3$-0.7$PbTiO_3$ structure at room temperature. *Phys. Rev. Lett.*, 108:137203, 2012.

[11] M. Bibes and A. Barthelemy. Multiferroics: Towards a magnetoelectric memory. *Nat. Mater.*, 7(6):425–426, 2008.

[12] J.-M. Hu and C. W. Nan. Electric-field-induced magnetic easy-axis reorientation in ferromagnetic/ferroelectric layered heterostructures. *Phys. Rev. B*, 80:224416, 2009.

[13] J. Akerman. Toward a universal memory. *Science*, 308(5721):508–510, 2005.

[14] S. Ikeda, J. Hayakawa, Young Min Lee, F. Matsukura, Y. Ohno, T. Hanyu, and H. Ohno. Magnetic tunnel junctions for spintronic memories and beyond. *Electron Devices, IEEE Transactions on*, 54(5):991 –1002, 2007.

[15] J. T. Heron, M. Trassin, K. Ashraf, M. Gajek, Q. He, S. Y. Yang, D. E. Nikonov, Y-H. Chu, S. Salahuddin, and R. Ramesh. Electric-field-induced magnetization reversal in a ferromagnet-multiferroic heterostructure. *Phys. Rev. Lett.*, 107:217202, 2011.

[16] Y.-H. Chu, L. W. Martin, M. B. Holcomb, M. Gajek, S.-J. Han, Q. He, N. Balke, C.-H. Yang, D. Lee, W. Hu, Q. Zhan, P.-L. Yang, A. Fraile-Rodriguez, A. Scholl, S. X. Wang, and

R. Ramesh. Electric-field control of local ferromagnetism using a magnetoelectric multiferroic. *Nat. Mater.*, 7(8):678–678, 2008.

[17] T. Wu, A. Bur, K. Wong, P. Zhao, C. S. Lynch, P. Khalili Amiri, K. L. Wang, and G. P. Carman. Electrical control of reversible and permanent magnetization reorientation for magnetoelectric memory devices. *Applied Physics Letters*, 98(26):262504, 2011.

[18] S.W. Choi, T.R. Shrout, S.J. Jang, and A.S. Bhalla. Morphotropic phase boundary in $PbMg_{1/3}Nb_{2/3}O_3$-$PbTiO_3$ system. *Materials Letters*, 8(6):253 – 255, 1989.

[19] U. Flechsig, F. Nolting, A. Fraile Rodriguez, J. Krempasky, C. Quitmann, T. Schmidt, S. Spielmann, and D. Zimoch. Performance measurements at the sls sim beamline. *AIP Conference Proceedings*, 1234(1):319–322, 2010.

[20] N. Pilet, J. Raabe, S. E. Stevenson, S. Romer, L. Bernard, C. R. McNeill, R. H. Fink, H. J. Hug, and C. Quitmann. Nanostructure characterization by a combined x-ray absorption/scanning force microscopy system. *Nanotechnology*, 23(47):475708, 2012.

[21] S. Chikazumi. *Physics of Ferromagnetism*. Oxford University Press, 1997.

[22] R. Farraro and R. B. Mclellan. Temperature dependence of the young's modulus and shear modulus of pure nickel, platinum, and molybdenum. *Metallurgical Transactions A*, 8(10):1563–1565, 1977.

[23] T. Fischbacher, M. Franchin, G. Bordignon, and H. Fangohr. A systematic approach to multiphysics extensions of finite-element-based micromagnetic simulations: Nmag. *Magnetics, IEEE Transactions on*, 43(6):2896 –2898, 2007.

[24] T. J. Regan, H. Ohldag, C. Stamm, F. Nolting, J. Lüning, J. Stöhr, and R. L. White. Chemical effects at metal/oxide interfaces studied by x-ray-absorption spectroscopy. *Phys. Rev. B*, 64:214422, 2001.

[25] C. A. F. Vaz. Electric field control of magnetism in multiferroic heterostructures. *Journal of Physics: Condensed Matter*, 24(33), 2012.

[26] N. Banerjee, M. Huijben, G. Koster, and G. Rijnders. Direct patterning of functional interfaces in oxide heterostructures. *Applied Physics Letters*, 100(4):041601, 2012.

[27] B. Hillebrands and K. Ounadjela, editors. *Spin Dynamics in Confined Magnetic Structures II*. Springer-Verlag Berlin Heidelberg, 2003.

[28] A. Grigoriev, D.-H. Do, D. M. Kim, C.-B. Eom, B. Adams, E. M. Dufresne, and P. G. Evans. Nanosecond domain wall dynamics in ferroelectric $PbZrTiO_3$ thin films. *Phys. Rev. Lett.*, 96:187601, 2006.

[29] Y. Chen, T. Fitchorov, A. L. Geiler, J. Gao, C. Vittoria, and V. G. Harris. Dynamic response of converse magnetoelectric effect in a pmn-pt-based multiferroic heterostructure. *Applied Physics A*, 100(4):1149–1155, 2010.

[30] L. Le Guyader, A. Kleibert, F. Nolting, L. Joly, P. M. Derlet, R. V. Pisarev, A. Kirilyuk, Th. Rasing, and A. V. Kimel. Dynamics of laser-induced spin reorientation in co/smfeo$_3$ heterostructure. *Phys. Rev. B*, 87:054437, 2013.

[31] E. Defaÿ, T. Lacrevaz, T. T. Vo, V. Sbrugnera, C. Bermond, M. Aïd, and B. Fléchet. Ferroelectric properties of Pb(Zr, Ti)O_3 thin films until 40 ghz. *Applied Physics Letters*, 94 (5):052901, 2009.

[32] A. Gruverman, D. Wu, and J. F. Scott. Piezoresponse force microscopy studies of switching behavior of ferroelectric capacitors on a 100-ns time scale. *Phys. Rev. Lett.*, 100:097601, 2008.

[33] Ferrodevices Ltd. Typical performance of packaged “ab” capacitors. Website, May 2015.

[34] J. Li, B. Nagaraj, H. Liang, W. Cao, Chi. H. Lee, and R. Ramesh. Ultrafast polarization switching in thin-film ferroelectrics. *Applied Physics Letters*, 84(7):1174–1176, 2004.

CHAPTER 7

Laser induced magnetisation reversal in GdFeCo nanostructures

This chapter describes the observation of magnetisation switching using a single femtosecond laser pulse for out-of-plane domains with sizes down to 200 nm in GdFeCo nanostructures. The magnetic domain structure of the GdFeCo magnetic elements through the laser induced magnetisation switching events is investigated using X-PEEM with in-situ femtosecond laser pulses. The experimental findings reveal that a complex domain structure is induced by the structuring process but it does not influence the efficiency of the laser induced magnetisation switching.[1]

7.1 Introduction

In order to further increase the recording density of magnetic hard drives, novel solutions to the magnetic recording trilemma arising from the competing requirements between readability, writeability and stability have to be found [2]. One promising solution is heat assisted magnetic recording (HAMR) where a laser pulse is used to heat up briefly the magnetic bit to be recorded in order to lower its coercivity to a value compatible with the magnetic field produced by the recording head [3]. Recent numerical atomistic scale modelling simulations of the spin dynamics in a Heisenberg Gd–Fe ferrimagnet demonstrated that the rapid transfer of energy into the spin system leads to switching of

[1] This chapter is adapted from L. Le Guyader, S. El Moussaoui, M. Buzzi, R. V. Chopdekar, L. J. Heyderman, A. Tsukamoto, A. Itoh, A. Kirilyuk, T. Rasing, A. V. Kimel and F. Nolting. *Appl. Phys. Lett.* **101** 022410 [1].

the magnetisation within a few picoseconds without the need of applying any magnetic field. The prediction was confirmed experimentally in GdFeCo ferrimagnetic alloys in which the ultrafast heating was realised with the help of a linearly polarised femtosecond laser pulse [4]. This switching via a *heat pulse only* occurs in a ferrimagnet consisting of 3d and 4f metals when the femtosecond laser pulse heats up the free electrons and thus excites the magnet on the time scale of the exchange interaction. This brings the system into a transient strongly non-equilibrium state due to the different demagnetisation time scales of the Gd and Fe sublattices [5] which relax deterministically into the reversed state [6]. More recently, all-optical switching has been observed in an increasing number of rare earth-transition metal alloys [7, 8], ferri- and ferromagnetic multilayers [9, 10].

These discoveries suggest that a new and possibly simpler solution to the magnetic recording trilemma can be proposed, involving only a laser heat pulse instead of the currently used magnetic recording head, and displaying tremendous recording speed. It is left to be verified, however, how such switching works in nanostructures, where the initial magnetisation states may be strongly modified by magnetostatic fields or by the manufacturing process itself, and where the relaxation from the transient strongly non-equilibrium state could be altered.

In the following, we demonstrate the magnetisation reversal in GdFeCo nanostructures for domains as small as 200 nm after applying a single, linearly polarised femtosecond laser pulse and without applying any magnetic field, i.e.by a *heat pulse only*. The three components of the magnetisation vector in the structures were determined with a photoemission electron microscope (PEEM) by performing an azimuthal dependent measurement of the x-ray magnetic circular dichroism (XMCD) at the Fe L_3 edge. The azimuthal study showed that the rims of the structures display an in-plane magnetic anisotropy, which seems to be the result of the thinning of the GdFeCo layer at the edge resulting from the fabrication process. Moreover, the in-plane rims are found to play no significant role in the reversal of the central out-of-plane domain.

7.2 Experimental Details

The sample consisted of a patterned thin multilayer of composition Si_3N_4(3 nm) / $Gd_{24.5}Fe_{66.1}Co_{9.4}$(20 nm) / Si_3N_4(5 nm) / AlTi(10 nm) deposited on a silicon substrate. Details on the growth and patterning process were given in chapter 4. The patterning resulted in isolated squares and discs with sizes ranging from 2×2 μm^2 down to 100×100 nm^2. The magnetic properties of the $Gd_{24.5}Fe_{66.1}Co_{9.4}$ film were characterised before structuring. The magnetisation compensation temperature was determined to be 370 K with a square out-of-plane hysteresis loop. The coercive field at room temperature was found to be 28 kA/m.

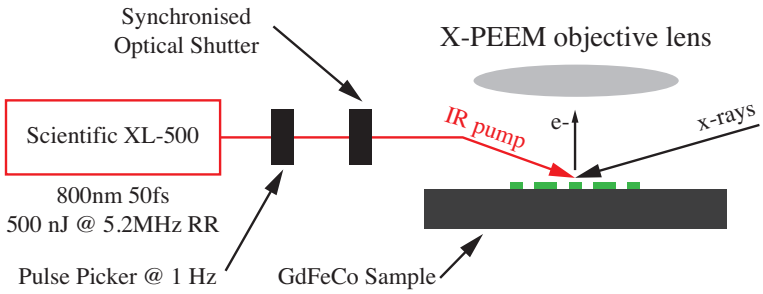

Figure 7.1: Schematic of the experiment.

Images of the magnetic domain states in these structures were obtained using the X-PEEM endstation at the Surface/Interface: Microscopy (SIM) beamline [11] at the Swiss Light Source. Imaging of the magnetic state of the nanostructures was performed employing X-ray magnetic circular dichroism (XMCD) tuning the incoming photon energy to the Fe-L_3 edge. The sample was excited with 50 fs long, 800 nm centre wavelength pulses produced by a Scientific XL-500 laser oscillator from Femtolasers Produtkions GmbH. Single laser pulses were selected using a pulse picker in combination with an optical shutter. The laser spot at the sample position had a full width at half maximum (FWHM) of 30 $\times$ 105 μm^2. Figure 7.1 shows a schematic of the experiment.

As defined in chapter 5, the contrast in the XMCD image is proportional to the dot product $\vec{M}(\vec{r})\cdot\vec{k}$, where $\vec{k}$ is the propagation vector of the incoming x-rays. In this experiment the x-ray impinge on the sample with a incidence angle $\theta = 74°$ giving sensitivity to both in-plane and out-of-plane magnetisation. By acquiring three different XMCD images of the same region at three different incoming x-ray azimuthal angles $\phi_{i=1..3} = (0°, 90°, 180°)$ it is possible to extract the single components of the magnetisation vector. In each of the XMCD images the pixel contrast will be proportional to:

$$\begin{aligned} XMCD_i = \vec{M}\cdot\vec{k} &= M_x k_x^i + M_y k_y^i + M_z k_z^i \\ &= M_x \sin\theta\cos\phi_i + M_y \sin\theta\sin\phi_i + M_z\cos\theta \end{aligned} \tag{7.1}$$

This leads to a linear system of three equations in three unknowns that can be resolved pixelwise to derive magnetisation images of the in-plane M_{in} and out-of-plane M_{out} magnetisation components [12, 13]. It is important to note that since the three different azimuthal angles are obtained by rotating the sample holder, the microscope aberrations are different in the three images. To mitigate this problem the images are registered with respect to each other using a combination of elastic transformations and sub-pixel drift correction prior to performing the pixelwise solution of the linear system [14].

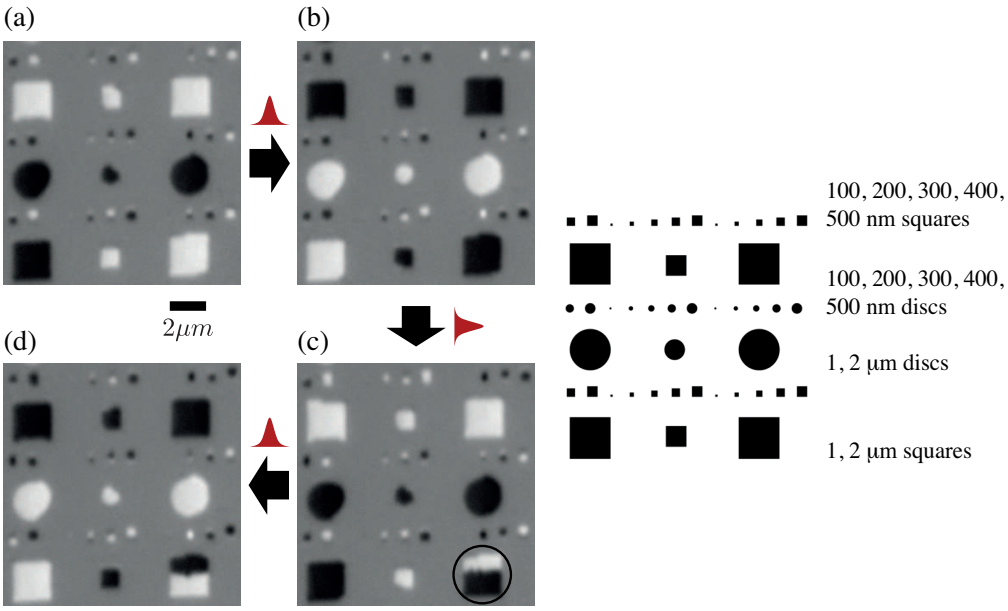

Figure 7.2: Sequence of successive XMCD images recorded at the Fe L_3 edge from the same region. The arrows indicate the order in which the images were recorded, while a single linearly polarised laser pulse was applied to the sample in between each of them. The circle indicates the case for which the switching is not complete. Adapted from [1]

7.3 Results and Discussion

A sequence of XMCD images, each recorded after excitation by a single linearly polarised laser pulse, is shown in figure 7.2b-e and illustrates the efficiency of the laser induced magnetisation switching in these structures. For the 2 and 1 μm wide structures, the reversal of the magnetisation is easily identified as a change from black to white or vice versa with an efficiency approaching 100%. In this specific example, out of the 9 largest structures visible and out of the 3 laser pulses, only one case (circled in figure 7.2d) does not result in a complete switching, giving a total switching efficiency of 96%. The behaviour of the smaller structures that are 500, 400 and 300 nm wide, is however not as evident as for the larger ones. Here, most of them seem to have stable multi-domain states with both black and white contrast in the same structure, in contrast to the larger structures which look mono-domain. These small structures show an apparently random switching behaviour. As will be shown later, this is due to the structures having in-plane as well as out-of-plane domains which cannot be distinguished in these images and which will be shown to behave differently.

In order to better understand their magnetic configurations and their laser induced

switching behaviour, an azimuthal dependent study was carried out, revealing the spatially resolved magnetisation vector components. The derived M_{in} and M_{out} magnetisation components from the azimuthal XMCD study of the initial state are shown in figure 7.3b,c respectively. In these images, the colour gives the component direction while the brightness gives its magnitude according to the colour wheel for the in-plane component and the colour double-headed arrow for the out-of-plane component. The azimuthal study was then repeated on the same structures after excitation by a single linearly polarised laser pulse and the result is shown in figure 7.3d and figure 7.3e. Comparing the out-of-plane magnetisation before and after the laser pulse in figure 7.3c and figure 7.3e clearly shows that the 2 μm square and disc as well as the smaller 500 and 400 nm squares have switched their central out-of-plane magnetisation, e.g. from red to blue or vice versa. The size of the out-of-plane domain in the 400 nm square is found to be 200 nm. For the smaller 300 and 100 nm wide structures, their out-of-plane central domain could not be imaged reliably. The limit here arises from a combination of the instrument spatial resolution, the electric field distortion from the structure edges and errors in the overlay of the three images recorded in different conditions [15]. At the same time, this azimuthal study reveals that all of the structures show an in-plane magnetised region of constant width at their edges. These in-plane magnetised rims explain the apparent multi-domain nature of the smaller structures observed in figure 7.2b-e, where the contrast is dominated by the in-plane magnetised domains. It is important to note that these in-plane rims do not play a role in the switching behaviour of the structures. This can be seen by comparing figure 7.3b and figure 7.3d where, while the out-of-plane domains of the 500 and 400 nm structures switch, their in-plane rims remain the same. This illustrates experimentally the strength of the drive by which this laser induced switching occurs. Indeed, simulations have shown that magnetic fields as high as 40 T are not sufficient to prevent the formation of the transient ferromagnetic-like state which leads to the magnetisation reversal [4]. This shows the insensitivity of the switched domains to their surroundings, a property which might be exploited to reach a very high recording density.

There are cases where the in-plane magnetisation changes after the laser excitation but without influencing the switching of the out-of-plane core, as can be seen for example at the edges of the 2 μm square in figure 7.3. Although the switching of the out-of-plane core is reproducible, the switching of the in-plane outer rim appears to be more complex. This might be related to thinning, oxidation, and/or modified anisotropy at the edge of the structures. Furthermore, the laser intensity distribution is not homogeneous inside the structure due to laser interference within it [16]. This difference in behaviour of the edge and the core of the structures explains the apparently random switching of the small structures in figure 7.2b-e. In these images, the contrast of the small structures is dominated by the in-plane magnetisation of the outer rim, and our azimuthal dependent study

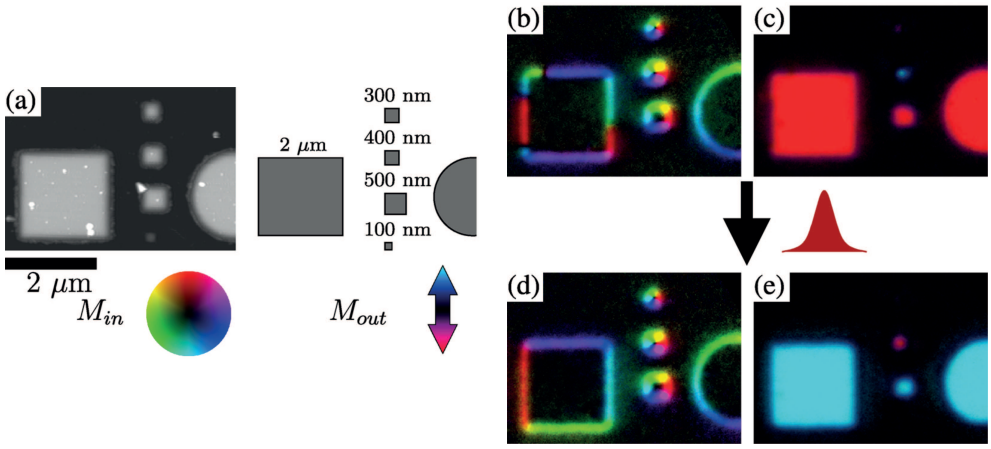

Figure 7.3: (a) Atomic force microscopy image of the sample showing the 2 μm square and disc and the 500, 400, 300 and 100 nm squares. In-plane M_{in} and out-of-plane M_{out} magnetisation images of the sample in its initial state (b) and (c) and after applying a single femtosecond laser pulse resulting in a slight change in the in-plane magnetisation (d) while the out-of-plane magnetisation reverses its direction, e.g. from down (red) to up (blue) magnetisation direction (e). Adapted from [1]

has allowed us to disentangle the switching behaviour of the core and the outer rim.

Despite the insensitivity of the switching process of the out-of-plane magnetisation to the surrounding magnetic configuration, it is nevertheless desirable to obtain mono-domain nanostructures for real device applications. It is thus important to understand the origin of the formation of the in-plane magnetised rims. To investigate possible oxidation of the structures, spectromicroscopy was performed at the Fe $L_{3,2}$ edges, for the centre part and the outer edge of the structures. The resulting X-ray absorption spectrum (XAS) for a 400 nm wide disc is shown in figure 7.4a. The spectrum obtained for the outer edge shows an additional shoulder, indicated by an arrow in figure 7.4a, that can be correlated with the presence of a certain level of Fe^{3+} oxidation [17]. By computing the pixel-wise difference between the Fe^{3+} and the Fe metal peak images, a map of the oxidation is obtained and shown in figure 7.4b. It shows that the oxidation is significantly inhomogeneous, and is concentrated at certain positions around the structure edges, which appear as bright spots in figure 7.4b. This observation does not correlate well with the presence of the in-plane magnetised rims of constant width around the perimeter of the structures, suggesting that oxidation is not the main cause. From the atomic force microscopy (AFM) image in figure 7.3a, line profiles for each of the structures are extracted and are shown in figure 7.4c. These line profiles reveal that a thinning of all the structures occurs at the edges over a distance of 150 nm. The lift-off process, which involves deposition of the magnetic layers on a structured polymer resist, results in thinner edges due to shadowing from the resist during film deposition. As the size of the structure becomes smaller

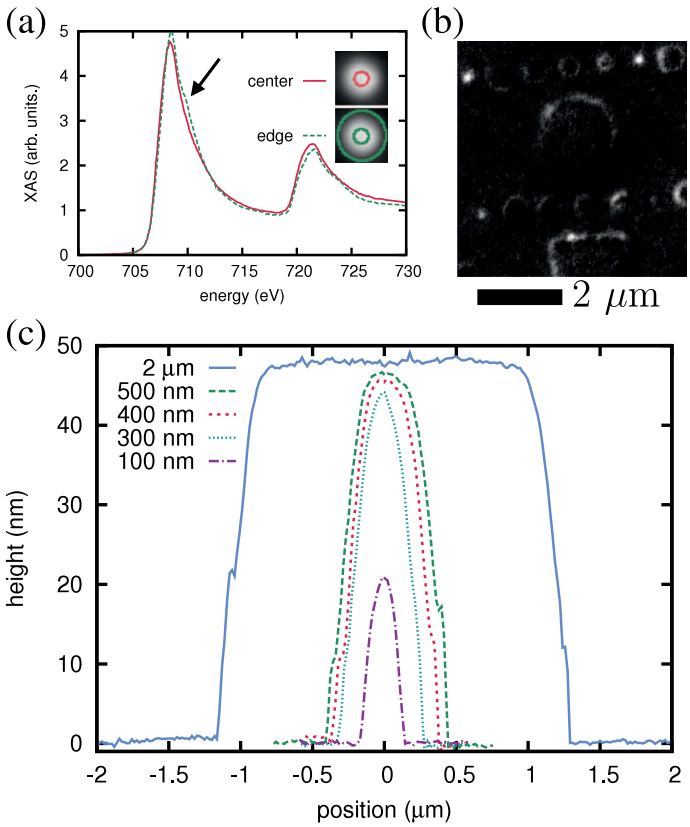

Figure 7.4: (a) XAS spectrum obtained from the central and edge regions of a 400 nm wide disk, with the inset indicating the regions of interest. The arrow indicates the position of the Fe^{3+} oxide peak. (b) Oxidation image obtained by computing the pixel-by-pixel difference between the Fe oxide and metal peaks images. (c) AFM line profiles for the different structures. Adapted from [1]

than the shadow, this effect becomes stronger to the point that it reduces the thickness of the 100 nm structures by a factor of 2. A reduced thickness of the GdFeCo film at the edges leads to a modified magnetic anisotropy of the material. Since this edge thinning is occurring for all the structures, it correlates better with the in-plane magnetised rims than the inhomogeneous oxidation from the edges. In addition, this thinning of the edge over 150 nm would explain why the 300 nm wide and smaller structures have no central out-of-plane magnetised region, as shown in figure 7.3. This means that in lieu of the lift-off process used in this work, a subtractive etch process such as ion milling through a hard mask producing top-hat thickness profile should result in mono-domain nanostructures better suited for high density recording applications. Moreover, this edge thinning implies that the size of the central region of the 400 nm wide square is consistent with the 200 nm domain size derived from the M_{out} component in figure 7.3c. This demonstrates

the potential of the *heat pulse only* switching in structured recording media for future applications.

7.4 Conclusion

We have demonstrated laser induced magnetisation switching in a 200 nm out-of-plane domain located in the centre of a 400 nm wide nanostructure. The in-plane edge domains are found to play no particular role in the efficiency of the switching thanks to the strength of the drive by which the switching occurs and are likely the result of a thinning of the magnetic film due to the fabrication method employed. This specific limitation can be lifted with an improved nanofabrication and optimised material properties. This work constitutes an important step towards the combination of laser induced magnetisation switching with bit patterned media for real device applications.

References

[1] L. Le Guyader, S. El Moussaoui, M. Buzzi, R. V. Chopdekar, L. J. Heyderman, A. Tsukamoto, A. Itoh, A. Kirilyuk, Th. Rasing, A. V. Kimel, and F. Nolting. Demonstration of laser induced magnetization reversal in gdfeco nanostructures. *Applied Physics Letters*, 101(2):022410, 2012.

[2] O. Heinonen and K.Z. Gao. Extensions of perpendicular recording. *Journal of Magnetism and Magnetic Materials*, 320(22):2885 – 2888, 2008.

[3] B. C. Stipe, T. C. Strand, C. C. Poon, H. Balamane, T. D. Boone, J. A. Katine, J.-L. Li, V. Rawat, H. Nemoto, A. Hirotsune, O. Hellwig, R. Ruiz, E. Dobisz, D. S. Kercher, N. Robertson, T. R. Albrecht, and B. D. Terris. Magnetic recording at 1.5 pb m^{-2} using an integrated plasmonic antenna. *Nat Photon*, 4(7):484–488, 2010.

[4] T. A. Ostler, J. Barker, R. F. L. Evans, R. W. Chantrell, U. Atxitia, O. Chubykalo-Fesenko, S. El Moussaoui, L. Le Guyader, E. Mengotti, L. J. Heyderman, F. Nolting, A. Tsukamoto, A. Itoh, D. Afanasiev, B. A. Ivanov, A. M. Kalashnikova, K. Vahaplar, J. Mentink, A. Kirilyuk, Th. Rasing, and A. V. Kimel. Ultrafast heating as a sufficient stimulus for magnetization reversal in a ferrimagnet. *Nat Commun*, 3:666, 2012.

[5] I. Radu, K. Vahaplar, C. Stamm, T. Kachel, N. Pontius, H. A. Durr, T. A. Ostler, J. Barker, R. F. L. Evans, R. W. Chantrell, A. Tsukamoto, A. Itoh, A. Kirilyuk, Th. Rasing, and A. V. Kimel. Transient ferromagnetic-like state mediating ultrafast reversal of antiferromagnetically coupled spins. *Nature*, 472(7342):205–208, 2011.

[6] J. H. Mentink, J. Hellsvik, D. V. Afanasiev, B. A. Ivanov, A. Kirilyuk, A. V. Kimel, O. Eriksson, M. I. Katsnelson, and Th. Rasing. Ultrafast spin dynamics in multisublattice magnets. *Phys. Rev. Lett.*, 108:057202, 2012.

[7] S. Alebrand, M. Gottwald, M. Hehn, D. Steil, M. Cinchetti, D. Lacour, E. E. Fullerton, M. Aeschlimann, and S. Mangin. Light-induced magnetization reversal of high-anisotropy tbco alloy films. *Applied Physics Letters*, 101(16):162408, 2012.

[8] A. Hassdenteufel, B. Hebler, C. Schubert, A. Liebig, M. Teich, M. Helm, M. Aeschlimann, M. Albrecht, and R. Bratschitsch. Thermally assisted all-optical helicity dependent magnetic switching in amorphous fe100–xtbx alloy films. *Advanced Materials*, 25(22):3122–3128, 2013.

[9] S. Mangin, M. Gottwald, C-H. Lambert, D. Steil, V. Uhlíř, L. Pang, M. Hehn, S. Alebrand, M. Cinchetti, G. Malinowski, Y. Fainman, M. Aeschlimann, and E. E. Fullerton. Engineered materials for all-optical helicity-dependent magnetic switching. *Nat Mater*, 13(3):286–292, 2014.

[10] C-H. Lambert, S. Mangin, B. S. D. Ch. S. Varaprasad, Y. K. Takahashi, M. Hehn, M. Cinchetti, G. Malinowski, K. Hono, Y. Fainman, M. Aeschlimann, and E. E. Fullerton. All-optical control of ferromagnetic thin films and nanostructures. *Science*, 345 (6202):1337–1340, 2014.

[11] U. Flechsig, F. Nolting, A. Fraile Rodríguez, J. Krempaský, C. Quitmann, T. Schmidt, S. Spielmann, and D. Zimoch. Performance measurements at the sls sim beamline. *AIP Conference Proceedings*, 1234(1):319–322, 2010.

[12] A. Scholl, H. Ohldag, F. Nolting, J. Stöhr, and H. A. Padmore. X-ray photoemission electron microscopy, a tool for the investigation of complex magnetic structures (invited). *Review of Scientific Instruments*, 73(3):1362–1366, 2002.

[13] V. Chakarian, Y. U. Idzerda, G. Meigs, E. E. Chaban, J.H. Park, and C. T. Chen. Element-specific vector magnetometry with magnetic circular dichroism. *Applied Physics Letters*, 66(24):3368–3370, 1995.

[14] L. Le Guyader, A. Kleibert, A. Fraile-Rodriguez, S. El Moussaoui, A. Balan, M. Buzzi, J. Raabe, and F. Nolting. Studying nanomagnets and magnetic heterostructures with x-ray peem at the swiss light source. *Journal of Electron Spectroscopy and Related Phenomena*, 185(10):371 – 380, 2012.

[15] F. Nolting. *Magnetic imaging with x-rays*, volume 133, pages 345–366. Springer Berlin Heidelberg, 2010.

[16] L. Le Guyader, M. Savoini, S. El Moussaoui, M. Buzzi, A. Tsukamoto, A. Itoh, A. Kirilyuk, T. Rasing, A. V. Kimel, and F. Nolting. Nanoscale sub-100 picosecond all-optical magnetization switching in gdfeco microstructures. *Nat Commun*, 6(5839), 2015.

[17] T. J. Regan, H. Ohldag, C. Stamm, F. Nolting, J. Lüning, J. Stöhr, and R. L. White. Chemical effects at metal/oxide interfaces studied by x-ray-absorption spectroscopy. *Phys. Rev. B*, 64:214422, 2001.

CHAPTER 8

Single shot measurements of Ultrafast Demagnetisation

This chapter starts with an introduction to the commonly employed methods used for probing ultrafast magnetisation processes, followed by the description of a new concept that makes possible single-pulse measurements employing spatial encoding using an off-axis zone plate. The development of the instrument and its implementation at the free electron laser FLASH are then described. Lastly, results from single pulse demagnetisation measurements of ferromagnetic thin films are presented. [1]

8.1 Introduction

As described in chapter 3, when a ferromagnet is excited with a strong, ultra-short laser pulse its magnetisation quenches rapidly. After almost two decades of intense research since its first discovery, ultrafast demagnetisation still presents unsolved puzzles regarding the underlying mechanisms governing the dynamics at the sub-picosecond time scale. Femtosecond laser pulses excite magnetic materials on a time scale which is comparable to the exchange interaction. In systems with more than one magnetic species, the different magnetic sublattices can then be pushed out of equilibrium in respect to each other yielding novel and intriguing behaviours such as the different demagnetisation time scales observed in NiFe alloys [1], as well as the all-optical magnetisation switching observed first in GdFeCo and then in other magnetic alloys and multilayers [2, 3, 4].

[1] Parts of this chapter are adapted from: M. Buzzi, M. Makita, L. Howald, A. Kleibert, B. Vodungbo, J. Raabe, N. Jaouen, K. Tiedtke, N. Schirmel, H. Redlin, C. David, F. Nolting, and J. Lüning, in preparation (2015)

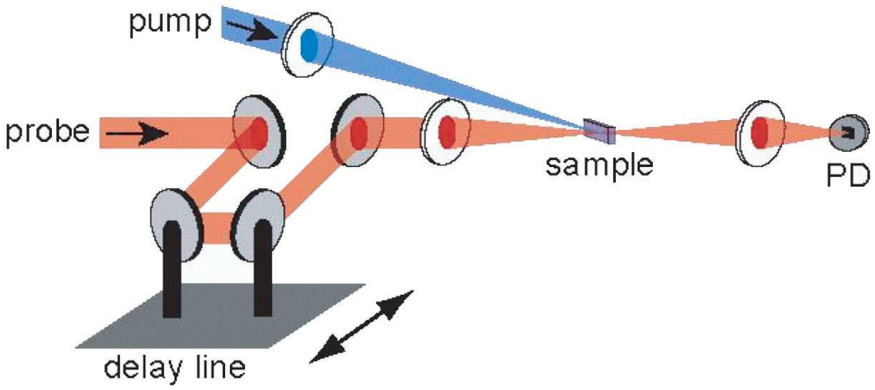

Figure 8.1: Schematic of a typical pump-probe setup for the measurement of ultrafast phenomena. Adapted from [5].

Up to now, measurements of magnetisation dynamics have been performed in the so-called pump-probe scheme in which an ultrashort laser pulse (pump) is used to excite the sample, and the subsequent relaxation process is reconstructed by the application of a second pulse (probe) after a certain time delay. Figure 8.1 shows a schematic representation of a pump-probe experiment. The time at which the sample magnetisation is sampled is defined by the arrival time difference of the probe and pump pulse at the sample surface. In order to reconstruct the full relaxation process, the arrival time delay is scanned by varying the position of the delay line. Typically, for each time delay setting the measurement is repeated multiple times and averaged in order to attain a sufficient signal to noise ratio. It is then clear that in this measurement scheme only the reproducible part of the induced dynamic process can be retrieved.

All the models for ultrafast demagnetisation that have been developed up to date are based on experimental measurements performed using stroboscopic pump-probe techniques. Due to this technical limitation it is still an open question whether ultrafast demagnetisation is governed only by reproducible processes, or if stochastic processes have to be considered for a proper interpretation of the results.

Although different schemes for single shot ultrafast spectroscopy using visible lasers have been presented and successfully employed in ultrafast chemistry [6], at visible wavelengths the contrast level of magneto-optic signals such as Kerr or Faraday effect is too low to allow for single-shot, time-resolved magnetisation measurements. The availability of intense, ultrashort x-ray pulses from free electron lasers opened the possibility of employing resonantly enhanced effects such as x-ray magnetic circular dichroism or transverse magneto-optic Kerr effect (T-MOKE) in the extreme ultraviolet. However, the conventional single-shot methods developed for visible light are not directly applicable

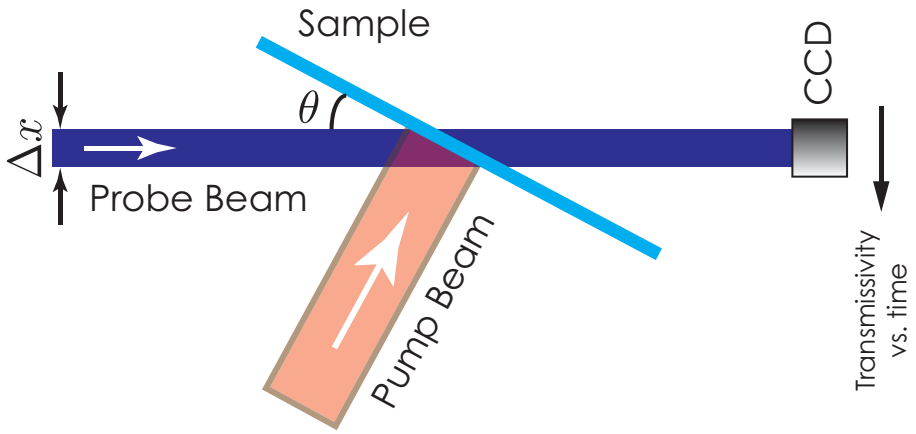

Figure 8.2: Schematic of a spatial encoding setup using non-collinear pump and probe beams.

in the soft x-ray regime.

In the following, we present a novel experimental development that overcomes this limitation. Our technique is based on an off-axis Fresnel zone plate to tilt the XUV pulse front in order to obtain a real-time measurement of the transient XUV reflectivity of a sample with sub-100fs time resolution. We successfully employed this setup to retrieve, in a single pump-probe event, the ultrafast demagnetisation dynamics of a cobalt thin layer, giving the first experimental proof of spatial encoding over a time window of 1500 fs. The magnetisation of the ferromagnetic sample was probed with ultrashort XUV pulses from the free electron laser FLASH using resonantly enhanced T-MOKE. Finally, by comparing demagnetisation curves from subsequent pump-probe events, we prove for the first time that no significant effect of stochastic phenomena are present.

8.2 Experimental Details

8.2.1 Concept of the experiment

Typically, single shot time resolved measurements rely on spatial encoding. The key of this technique is encoding the time delay between pump and the probe pulses in one of the beam spatial coordinates. At visible wavelengths this can be obtained using different methods such as (i) tilting the propagation direction of the probe beam with respect to the pump beam, or (ii) by tilting the probe pulse front with a diffraction grating [6]. The first option, shown in figure 8.2, is the simplest since it does not require special optical elements. While this is beneficial for applications involving x-rays, this scheme has intrinsic shortcomings. This example employs a grazing incidence geometry for the probe beam

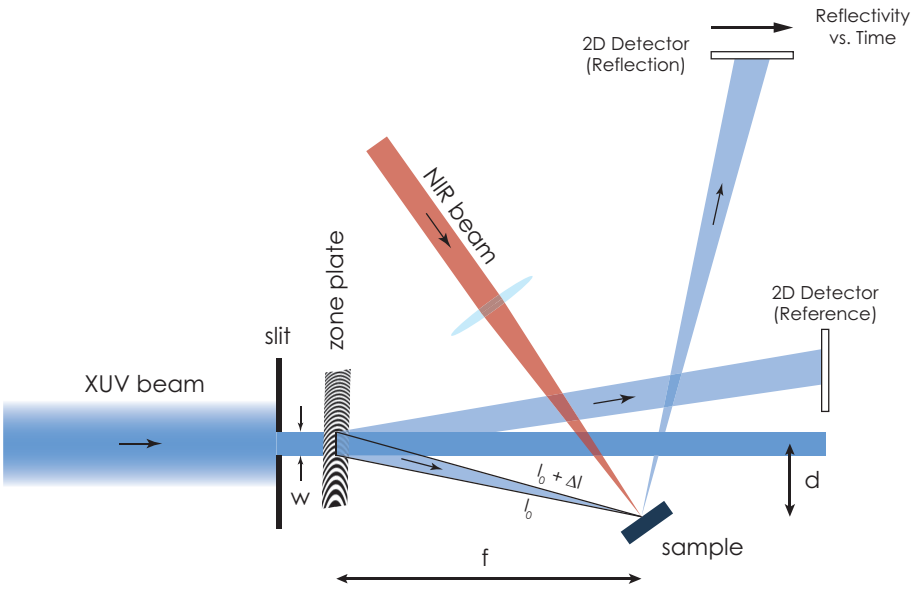

Figure 8.3: Simplified schematic of the novel development proposed here, employing an off-axis Fresnel zone plate for single-shot time-resolved magnetisation measurements.

and a normal incidence geometry for the pump beam. As a consequence, the delay time between the arrival of the pump and the probe pulse at the sample surface varies continuously along the x coordinate. A 2D detector is used to collect the probe beam transmitted through the sample and the transmissivity of the sample is probed over an extended time delay range Δt. This value is strictly linked to the geometry of the experiment and can be calculated as:

$$\Delta t = \Delta x \frac{\cos\theta}{c} \tag{8.1}$$

where Δx is the probe beam width, c is the speed of light, and θ is the grazing angle. Substituting typical values like $\Delta x \approx 100\,\mu$m and $\theta = 15°$ one obtains a time window $\Delta t \approx 330$ fs. Unfortunately, this time window is too small for studying the early time period of ultrafast demagnetisation that extends up to 2 ps. In addition, since most free electron lasers only deliver linearly polarised pulses, the ideal magnetic contrast mechanism is T-MOKE, which however gives very poor sensitivity at grazing incidence.

To circumvent these problems we decided to follow the more complicated pulse front tilting route. Figure 8.3 shows the conceptual drawing of the set-up proposed in this work. It relies on the fact that the optical path length of the rays propagating from a Fresnel zone plate to its focal point varies with their distance to the zone plate optical axis. As a consequence, when using off-axis illumination, the zone plate can be used to introduce a

pulse front tilt as well as to focus the incoming beam. The sample is positioned in the first order focus of the zone plate and is excited by a near infrared pulse at normal incidence. The time delay between the pump and the probe pulse is encoded in a spatial coordinate of the reflected beam. The total time window probed in a single pump-probe event is given by:

$$\Delta t = \frac{1}{c}\left(\sqrt{f^2-\left(d+\frac{w}{2}\right)}-\sqrt{f^2-\left(d-\frac{w}{2}\right)}\right) \tag{8.2}$$

where f is the focal length of the zone plate, d is the off-axis distance, and w the incoming beam diameter. For values of $f = 80$mm, $d = 8$mm, and $w = 5$mm one obtains $\Delta t \approx 1.6$ps, a much better suited time span for ultrafast magnetisation measurements. The magnetisation of the sample is probed using T-MOKE at the $M_{2,3}$ resonances of 3d metals (52 eV - 66 eV). As will be explained later, T-MOKE generates a change in reflectivity when the magnetisation of the sample changes, so the first detector, positioned in the reflected beam, records directly the time-resolved demagnetisation curve. To normalise shot-to-shot fluctuations of the beam profile and intensity, an identical detector is positioned in the negative first diffraction order of the zone plate.

8.2.2 Transverse magneto-optic Kerr effect in the extreme ultraviolet[2]

Generally, the magneto-optic Kerr effect (MOKE) refers to the interaction of linearly polarised light with a magnetised surface. Depending on the scattering geometry chosen for the experiment, the polarisation state of the light reflected from the sample or the sample reflectivity itself is affected by the magnetisation state of the sample. In the following we focus on the transverse magneto-optic Kerr effect (T-MOKE), while more general details about MOKE can be found in [8].

Figure 8.4 shows the scattering geometry for T-MOKE experiments. In this configuration, changes in the in-plane magnetisation perpendicular to the scattering plane induce a change in the sample reflectivity. It is possible to calculate the reflected intensity from a magnetised surface for incident light with p-polarisation [9]:

$$I_{\pm}^{P} = I_0\left|\frac{n\cos\theta-\cos\chi}{n\cos\theta+\cos\chi}\pm\epsilon_{xy}\frac{2\sin\theta\cos\theta}{n(n\cos\theta+\cos\chi)^2}\right|^2 \tag{8.3}$$

and for incident light with s-polarisation:

$$I_{\pm}^{S} = I_0\left|\frac{\cos\theta-n\cos\chi}{\cos\theta+n\cos\chi}\right|^2 \tag{8.4}$$

[2]This section follows the description given in [7]

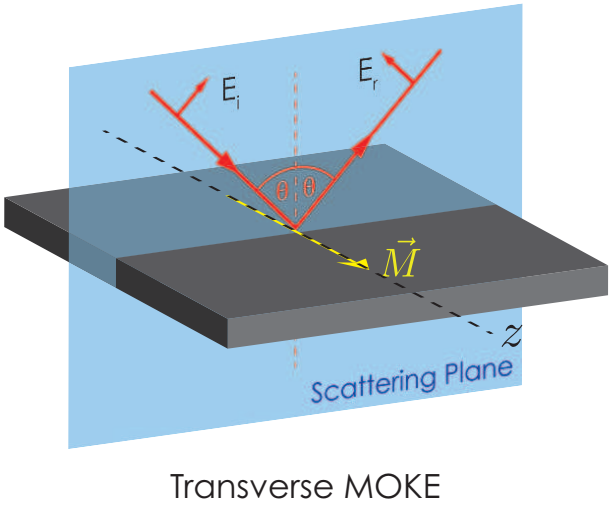

Figure 8.4: Scattering geometry in T-MOKE experiments.

Here, I_0 is the incident light intensity, n the refractive index of the material, θ the angle of incidence, $\chi = \sin^{-1}(\sin\theta/n)$ the refractive angle and ϵ_{xy} is the magnetisation dependent, off-diagonal element of the dielectric tensor. The plus-minus sign depends on the magnetisation orientation being parallel or antiparallel to the scattering plane normal.

We observe that the reflected intensity in the case of s-polarised light does not depend on the sample magnetisation. In the case of p-polarised light, one finds that the second part of the equation is magnetisation dependent through ϵ_{xy} which is linearly proportional to the sample magnetisation along the z axis. Also, ϵ_{xy} is generally small ($\approx 10^{-3}$) allowing us to neglect second order contributions to the reflected intensity. In other words, the reflected intensity for p-polarised light is linearly proportional to the sample magnetisation [10].

The particular advantage of T-MOKE is that it does not require polarisation analysis to recover the magneto-optic signal from the sample. This is particularly advantageous for experiments using soft x-rays where the measurement of the polarisation state of the reflected light requires the development of purpose made multilayers. Furthermore, in the XUV regime, it is possible to tune the energy to be at resonance with the $M_{2,3}$ edges of the 3d magnetic element under investigation and obtain a resonant enhancement of ϵ_{xy}. This not only makes T-MOKE element selective, as in the case of XMCD, but also causes an increase of the magnetic signal from below 1% in the visible range to few tens of percent in the XUV. The origin of this resonant enhancement is found in the large spin-orbit coupling and exchange splitting of the 3p core states.

Similarly to the case of XMCD, the magnetic signal can be enhanced measuring the

sample reflectivity for two opposite magnetisation directions (parallel I_+^P, and antiparallel I_-^P to the z-axis) and calculating the asymmetry parameter. One can explicitly formulate the T-MOKE asymmetry as:

$$\text{T-MOKE} = \frac{I_+^P - I_-^P}{I_+^P + I_-^P} \tag{8.5}$$

$$\simeq \frac{\sin 2\theta}{1-2\cos^2\theta} \frac{\delta \Re[\epsilon_{xy}] + \beta \Im[\epsilon_{xy}]}{\delta^2 + \beta^2}$$

Equation 8.5 was obtained substituting 8.3 for $I_\pm^P$ and $n = 1-\delta+i\beta$, in the approximation of small δ and β. This relation gives two important sets of information about the T-MOKE effect in the extreme ultraviolet. Firstly, it suggests that the sensitivity of T-MOKE is maximum at an incident angle $\theta \approx 45°$.[3] Secondly, the energy dependence of the T-MOKE signal enters both via ϵ_{xy} and via δ and β. It is important to note that, due to rather large line width of the $M_{2,3}$ transitions, the magnetic signal from a single element might extend over few eV and care must be taken when measuring magnetic samples containing multiple magnetic species that no overlapping resonance lines are present.

8.2.3 Requirements for the probe pulse

The $M_{2,3}$ edges of Fe, Co, and Ni fall in the energy range between 52 eV and 66 eV. Spatial encoding techniques do not achieve sub pulse length resolution as opposed to streak cameras. Therefore, to attain ultrafast magnetisation measurements with sub-100fs time resolution, the probe pulse should be intense enough to allow for single shot measurement, have sub-100fs duration, and a central wavelength in the XUV range to match the $M_{2,3}$ of the elements we plan to study. For this reason, the experiments presented here were performed at the free electron laser FLASH in Hamburg, Germany using the direct SASE beam from BL2. A detailed description of how ultrashort XUV pulses are generated at FLASH alongside with the capabilities of the facility is given in appendix A.

8.2.4 Optics design and fabrication

Since the off-axis Fresnel zone plate employed in the optical set-up is used in transmission, the support structure of the zone plate should be as transparent as possible in the 50 eV to 70 eV energy range. For this purpose, silicon turned out to be the ideal candidate. The focal length and the off-axis distance were defined in order to obtain the largest time

[3] More generally, it can be shown that the maximum sensitivity is obtained at the Brewster angle. At XUV wavelengths there is no large refractive index mismatch at the interface with vacuum and this angle is $\approx 45°$

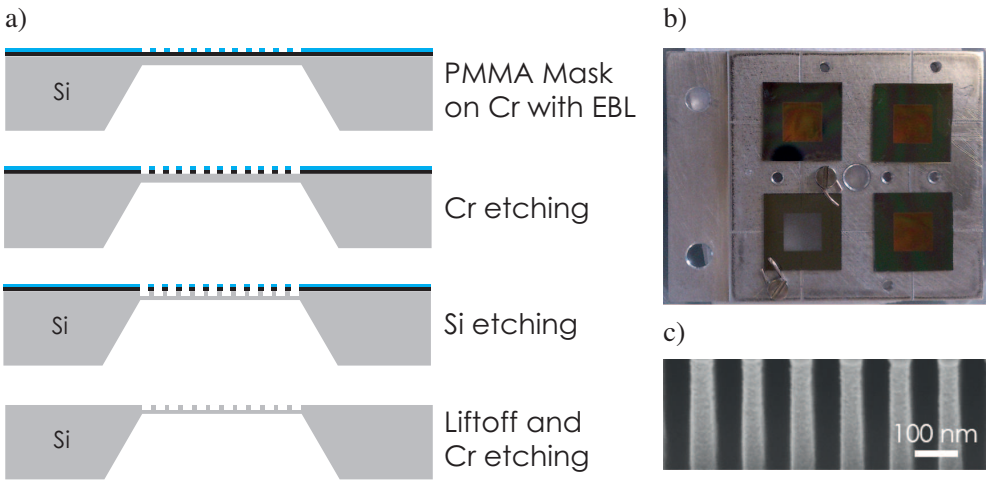

Figure 8.5: (a) Fabrication steps of the Fresnel zone plate. (b) Zone plates mounted on the zone plate mount. (c) SEM micrograph of the zone plate structure.

window Δt while maintaining the fabrication requirements attainable. The focal length of the zone plate was set to f=80 mm, with an off-axis distance w=7.9 mm for an incoming photon energy of 60 eV. To simplify the alignment procedure of the whole set-up, the alignment can be performed using an alignment HeNe laser available at the FLASH beamlines. For this reason, zone plates with the same optical properties at 1.96 eV were also produced.

Figure 8.5 shows (a) the fabrication process of the zone plate, (b) the zone plates mounted on their holder and (c) an SEM micrograph of the zone plate structure. The zone plates are fabricated starting from $4.8 \times 4.8\,\mathrm{mm}^2$ wide, 1 µm thick single crystalline Si membranes. As a first step, a chromium mask layer is defined with a combination of traditional electron beam lithography and chromium etching techniques. The grating is then etched into the silicon membrane using reactive ion etching. The following lift-off process and removal of the chromium mask results in the final zone plate structure. The fabrication process was carried out by Dr. M. Makita and Dr. C. David at the Laboratory for micro- and nanotechnology of the Paul Scherrer Institut, Villigen, Switzerland.

8.2.5 The experimental set-up

The complete schematic of the experimental setup is shown in figure 8.6(a). The XUV beam first propagates to the zone plate and is diffracted off in two beams (i) the negative first diffraction order which propagates to the reference detector and (ii) the first diffraction order which is focused on the sample. The sample is positioned in the first order focus

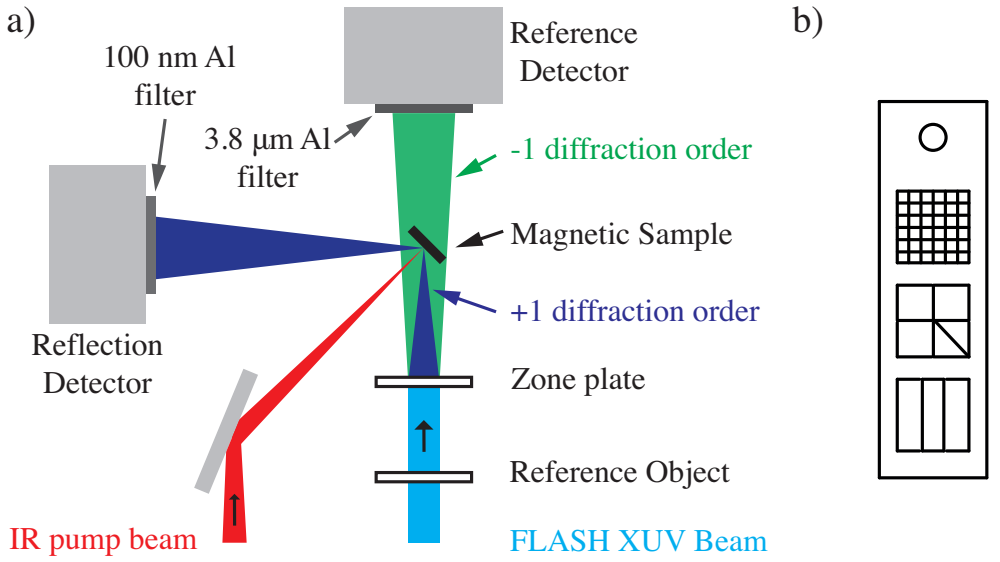

Figure 8.6: (a) Schematic of the XUV optical set-up (top view). (b) Schematic of the reference objects.

of the zone plate at an incidence angle of $\approx 45°$ to maximise the T-MOKE sensitivity and a second area detector collects the specular reflectivity from the sample. A 100 nm thick aluminium filter is placed in front of the reflection detector to screen eventual scattered light from the pump beam while a 3.8 µm thick aluminium filter was placed in front of the reference camera in order to protect it from infrared photons and to attenuate the negative first order beam by a factor 10^{-3} so that the intensity reaching this detector is comparable to the one reaching the reflection detector. Both aluminium filters were manufactured by Luxel Corp., USA and were delivered on a TF114 mount. The expected transmission of the filter was calculated based on [11] including a 5 nm oxidation layer for each exposed surface. Finally, a reference object can be inserted in the beam to project a known image on the reference and reflection detectors in order to calculate the transformation matrix correlating the images acquired by the two detectors. Figure 8.6b shows the schematic of the three available reference objects, which are a 0.3 mm pitch copper mesh, a cross, and a set of two 0.1 mm thick straight wires.

Since most of the optical setup involves propagation of beams in the extreme ultraviolet it has to be enclosed in a vacuum chamber. For this purpose, a rectangular vacuum chamber (main chamber) was designed and hogged out of a solid block of aluminium by VA-TEC GmbH, Germany. Figure 8.7 shows the mobile endstation that was built in order to perform this experiment. To obtain the maximum flexibility in the positioning of the XUV optical components, the main chamber contains an aluminium breadboard to which the

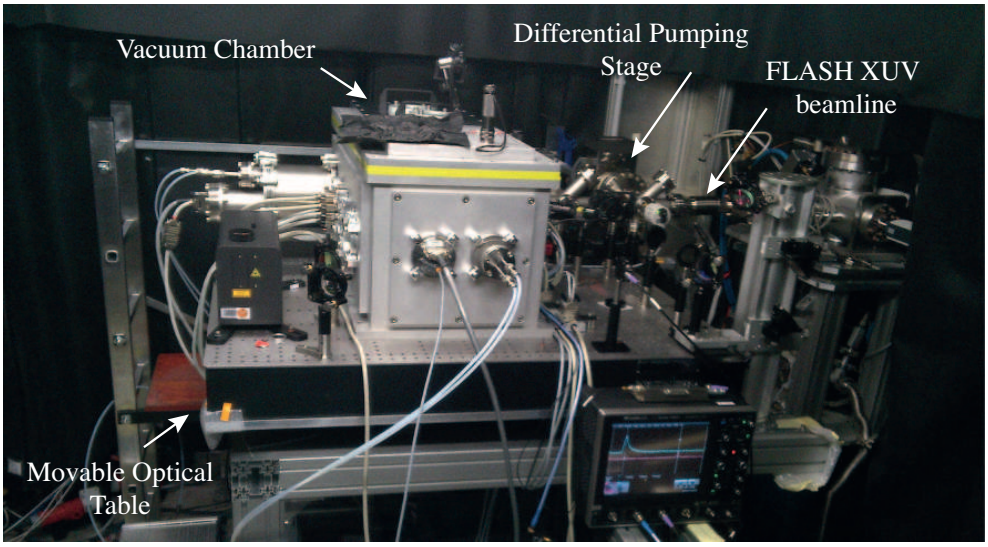

Figure 8.7: Picture of the experimental setup at the free electron laser in Hamburg FLASH.

optical elements can be fixed. The main chamber is pumped by a 400 ls^{-1} turbo molecular pump and achieves a base pressure of $\approx 1 \times 10^{-6}$ mbar. A differential pumping stage realised with a combination of a 60 ls^{-1} turbo molecular pump and an ion getter pump allows us to keep the pressure at the beam line connection in the 10^{-8} mbar range. A gate valve with a sapphire window separates the main chamber from the differential pumping stage. In this way, the HeNe alignment laser beam can propagate to the main chamber while keeping the beamline connection part in vacuum even when the main chamber is vented.

The vacuum chamber is mounted directly on a honeycomb optical breadboard that allows for the positioning of the remaining infrared optic needed for the experiment. The breadboard positioning with respect to the beam direction can be adjusted by lead screw operated mechanisms. The height of the whole end station can be adjusted using rubber feet with adjustable length. This mobile endstation has been successfully employed at the VUV beamline of the Swiss Light Source in Villigen, Switzerland and at the free electron laser FLASH in Hamburg, Germany.

Figure 8.8 shows the inside of the vacuum chamber. Although the preliminary alignment is performed when the vacuum chamber is vented using the HeNe alignment laser from the FLASH beamlines, its collinearity with the XUV beam is not perfect and the alignment often requires tweaking when switching to the XUV beam. For this reason, most of the components are mounted on in-vacuum positioners.

The reference object stage (partially seen in the picture) allows for moving the refer-

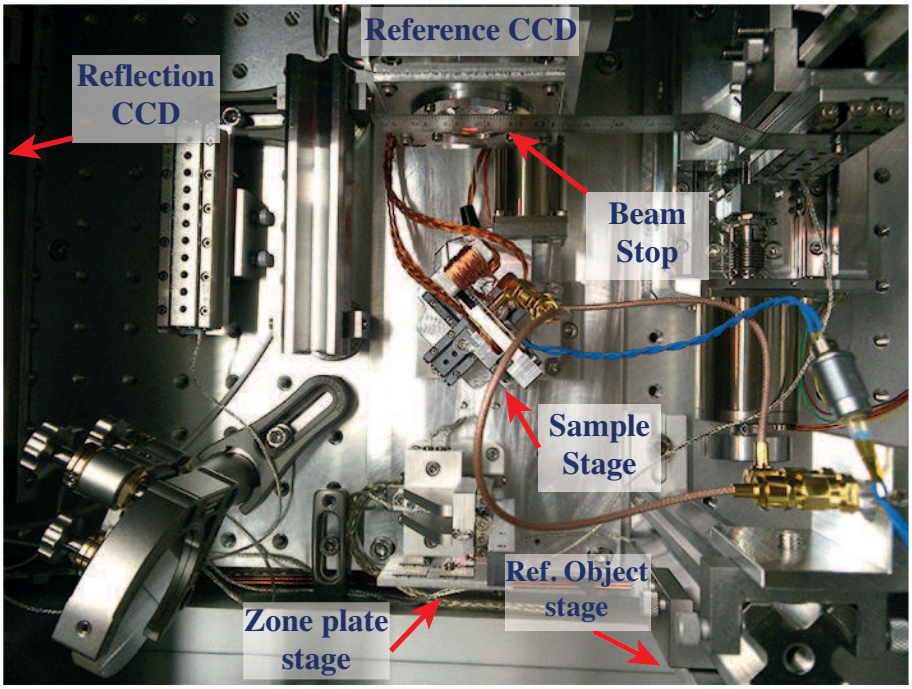

Figure 8.8: Picture of the in-vacuum optical setup (top view).

ence object in and out of the XUV beam. A set of three XUV zone plates, plus one HeNe alignment zone plate can be moved with respect to the beam using a SmarAct SLC-2445 xyz manipulator. The sample stage combines a rotation stage to adjust the incidence angle θ and a SmarAct SLC-1750 xyz manipulator to adjust the position of the sample under the beam. A beam dump fabricated out of a stainless steel ruler can be positioned in the zero order beam transmitted through the zone plate. The reference CCD is mounted on a linear translation stage that allows for moving the detector along the beam propagation direction. In order to enable θ-2θ scans, the reflection CCD has two linear translations: one in the propagation direction of the reflected beam and one orthogonal to it. To achieve high-vacuum, all the mounts are made of stainless steel or bare aluminium and have proper venting holes. The wiring is performed with high-vacuum compatible cables. The CCD detectors are two identical PI-MTE 2048 in vacuum CCD from Princeton Instruments with a sensitive area of 2048x2048 pixels having a size of 13.5 µm[4].

Figure 8.9 shows a detailed view of the aluminium sample holder used in the experiment. A custom built electromagnet is wound on an ARMCO pure iron yoke and generates magnetic field pulses up to 60 mT with a duration varying between 300 µs and 300 ms. It is

[4]The two CCD detectors were borrowed from the Laboratoire d'Optique Appliquée and Synchrotron Soleil in Paris, France

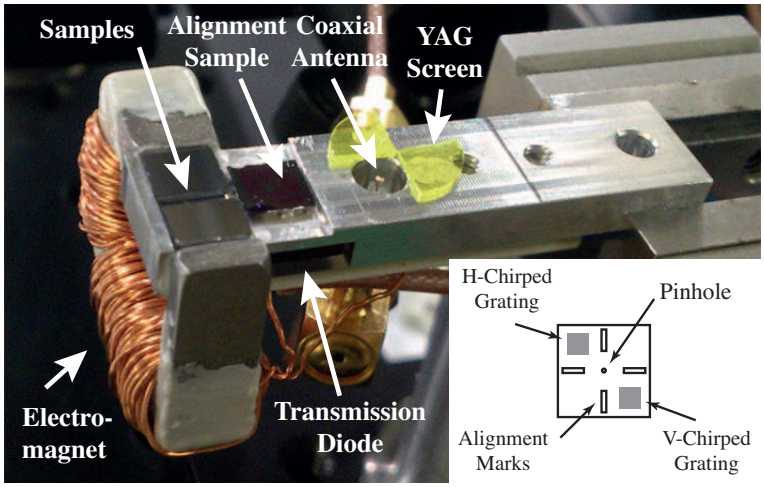

Figure 8.9: Picture of the sample holder. A detailed view of the alignment sample is shown in inset.

glued with a UHV compatible epoxy (Epotek T-7110) to the main structure of the sample holder. The magnetic samples are mounted directly in the magnet gap. An alignment sample is mounted next to the magnetic samples and its structure is shown in the inset of figure 8.9. It carries a patterned pinhole, a vertical, and a horizontal chirped linear gratings for beam profiling purposes. An XUV sensitive photodiode is mounted on the back of the sample holder and collects the beam transmitted by the alignment sample. To visualise the position of the XUV beam using an external camera, a YAG screen is glued to the sample holder. Finally, a so called "coaxial antenna" is installed on the sample holder in order to achieve the rough time overlap between the infrared and XUV lasers as will be explained later. Since the pump and probe beams are propagating in a non collinear geometry, one has to make sure that the surfaces of the magnetic samples and the alignment sample coincide. This was achieved by gluing the samples only along the edges while resting them on the surface of the sample holder. The flatness of the sample mounting surface was checked with a micrometer resolution indicator.

The data acquisition system is based on the integration of the FLASH DAQ system DOOCS, used to retrieve shot-to-shot beam parameters, and of an EPICS based system that controls the CCD detectors. Fast digitisers provided by FLASH operate synchronously to the free electron laser and are used to sample signals from the fast transmission photodiode. The measurement sequencing and motion control is performed using a purposely modified version of the Scanning Transmission X-ray Microscope control software used at the Swiss Light Source.[5]

[5]I am greatly indebted to Dr. Jörg Raabe for including in the STXM software the measurement sequencing procedures required for this experiment.

8.2.6 Alignment and measurement protocols

Before starting the time-resolved measurements it is important to ensure both a good spatial and temporal overlap of the pump and probe beams. Due to the extended bandwidth of the SASE pulses, the probe beam is elliptical with a typical focused size of $40 \times 100\,\mu m^2$. To ensure homogeneous pumping in the probed area, the pump beam focus diameter was set to 500 µm. To start, the pump and the probe beam are brought as close as possible on the YAG crystal with the aid of an out-of-vacuum camera looking at the sample. To refine the spatial overlap, a 30 µm diameter pinhole is available on the alignment sample (Fig. 8.9) and can be scanned in each of the pump or probe beams to record their spatial profile. The position of the out-of-vacuum infrared focusing lens is adjusted until the centre of the spatial profiles of the pump and the probe beam coincide.

Once the spatial overlap of the XUV and the near infrared beam is achieved, one has to find the temporal overlap. The coarse temporal alignment is achieved with the "coaxial antenna" approach. This device consists of a high frequency rigid coaxial cable whose end has been stripped to expose the core wire for a length of approximately 2 mm. When the XUV or IR laser pulse hit the wire, photoelectrons are created and a current pulse is generated. This signal is amplified with a wide-band amplifier (Kuhne Electronics KU LNA BB 0180 A-SMA) and fed to an oscilloscope with 2 GHz bandwidth. The oscilloscope is triggered using the signal from a photodiode positioned in the leakage of one of the IR mirrors. As a first step, the IR beam is blocked and a time trace using the beam from the X-FEL is acquired and stored as reference. Then, time traces using only the beam from the IR laser are acquired and the electronic delay of the pump-probe laser is adjusted until the signal from the IR pulse overlaps with the signal from the XUV pulse. In this way the time overlap can be found with a precision of ±30 ps. The fine adjustment of the time overlap is performed during the experiment itself.

Due to the long read out time (≈ 4 s) of the PI-MTE CCD detectors, FLASH was operated in single bunch mode and the beamline fast shutter was used to select single pulses. In the experiments that are described in the following, the machine was operated in low bunch charge mode, delivering a pulse duration of approximately 50 fs with an energy bandwidth of 1%. The energy per pulse delivered by the free electron laser was $80 \pm 10 \mu J$ at a wavelength of 20.8 nm for the experiments on Co films, and a wavelength of 18.7 nm for the measurements on Co (0.2 nm) / Ni (0.2 nm) multilayers. The infrared pump laser delivered 100 µJ, 70 fs pulses with a central wavelength of 810 nm.

An automatic shutter in the IR pump path was employed and used to avoid continuous exposure of the sample to the pump beam during the CCD readout. The PI-MTE CCD detectors were run in continuous clean mode, at a temperature of 230 K. To minimise eventual dead times, a TTL trigger line was used to start the exposure. To avoid overheating of the electromagnet, the magnetic field was pulsed synchronously with the acquisition

time of the CCD cameras.

During the experiment we observed that the dark field image of each CCD detector showed changes approximately every two to three exposures. To minimise eventual artefacts due to this behaviour, a dark field image was acquired right after any exposure with the XUV pulse. This process was implemented in an automated measurement cycle in which a set of 4 images is acquired:

Pumped image: The sample is illuminated with both the XUV and the IR pulse and the transient reflectivity is recorded. It is indicated as I_p.

Pumped image background: The sample is illuminated only with the IR pulse and the dark field for the pumped image is recorded. It is indicated as: I_p^{dark}.

Unpumped image: The sample is illuminated only with the XUV and the static reflectivity of the sample is recorded. It is indicated as: I_u.

Unpumped image background: The sample is not illuminated with either of the pulse and the dark field for the unpumped image is recorded. It is indicated as: I_u^{dark}.

The acquired images are corrected for the corresponding dark field images, and in order to normalise out fluctuations of the incoming beam intensity profile, each image recorded by the reflection CCD detector is normalised by the image acquired by the reference CCD detector. After this process, the normalised pumped image I_p^{norm} and the normalised unpumped image I_u^{norm} are obtained.

The basic measurement cycle listed above can be nested in more complex sequences, for example for the measurement of the T-MOKE asymmetry (the sequence is repeated for two different polarities of the magnetic field), or in pump-probe delay scans (the sequence is repeated for different delay settings of the pump-probe laser). This last option allows for automatically collecting a series of images at different time delay, which is particularly useful when optimising the temporal overlap. In the case of single shot measurements, the XUV and the IR shutter open synchronously and illuminate the sample a single time. Instead, in the case of multiple shot measurements the IR shutter is left open for the whole duration of the measurement since it cannot withstand opening and closing at 10 Hz repetition rate.

In the following we will refer to the T-MOKE image as the image obtained by the pixel-wise calculation of:

$$\text{T-MOKE image} = \frac{I_p^{\text{norm}}(+M) - I_p^{\text{norm}}(-M)}{I_p^{\text{norm}}(+M) + I_p^{\text{norm}}(-M)} \tag{8.6}$$

where M indicates the sample magnetisation. In a similar manner we will refer to a transient reflectivity image or TR-image as the contrast map obtained by the pixel-wise calcula-

tion of:

$$\text{TR-image} = \frac{I_p^{\text{norm}}(+M) - I_u^{\text{norm}}(+M)}{I_u^{\text{norm}}(+M)} \tag{8.7}$$

While in the T-MOKE case two pump-probe measurements with opposite magnetisation directions are required to isolate the magnetic signal, the TR-image recovers the magnetic signal with the combination of a pump-probe image and an unpumped image allowing for a true single shot measurement of the ultrafast demagnetisation process. In both images the contrast is proportional to the sample magnetisation change at a certain time delay given by the spatial coordinates in the image.

8.3 Simulation of the experiment

As a preliminary step we calculated, using a geometrical ray optics approach, how the time delay varies as a function of the two spatial coordinates in the reflected beam image. Figure 8.10a shows the result of the calculation in the approximation of a perfectly planar wavefront. The time delay varies as a function of the radial distance from the zone plate optical axis giving rise to circular isochronous lines and making the time delay a quadratic function of the pixel coordinates in the image as shown in figure 8.10b. For this reason, the extraction of accurate time resolved data from the TR-image requires, as an ansatz, the simulated time delay map. In first approximation, for the optical arrangement used in this experiment (Fig. 8.6), the time delay varies mainly in the y-coordinate of the reflected beam image while the x-coordinate can be related mainly to a change in the incidence angle $\theta \approx \pm 1.5°$.

It is also possible to simulate the real image acquired by the detector in the reflected beam by mapping on the calculated time delay map (Fig. 8.10a), the change in reflectivity due to the ultrafast demagnetisation process in a 3d metal (Fig. 8.10c). The result, plotted in figure 8.10d, shows the onset of a clear drop in reflectivity due to the demagnetisation process at the isochronous line corresponding to the pump-probe time overlap. One can observe that due to its definition, the TR-image does not carry information about eventual angular dependences of the reflectivity by the incidence angle, making it possible to average through the x-coordinate and increase the signal-to-noise ratio of the measurement.

8.4 Results and Analysis

In this section the experimental results obtained with the presented set-up are discussed. The measurements were performed on a Co (20 nm) thin film and a [Co (0.2 nm) / Ni (0.2 nm)]$_{20}$ multilayer. The sample layer stack and fabrication techniques used to prepare the samples are described in chapter 4.

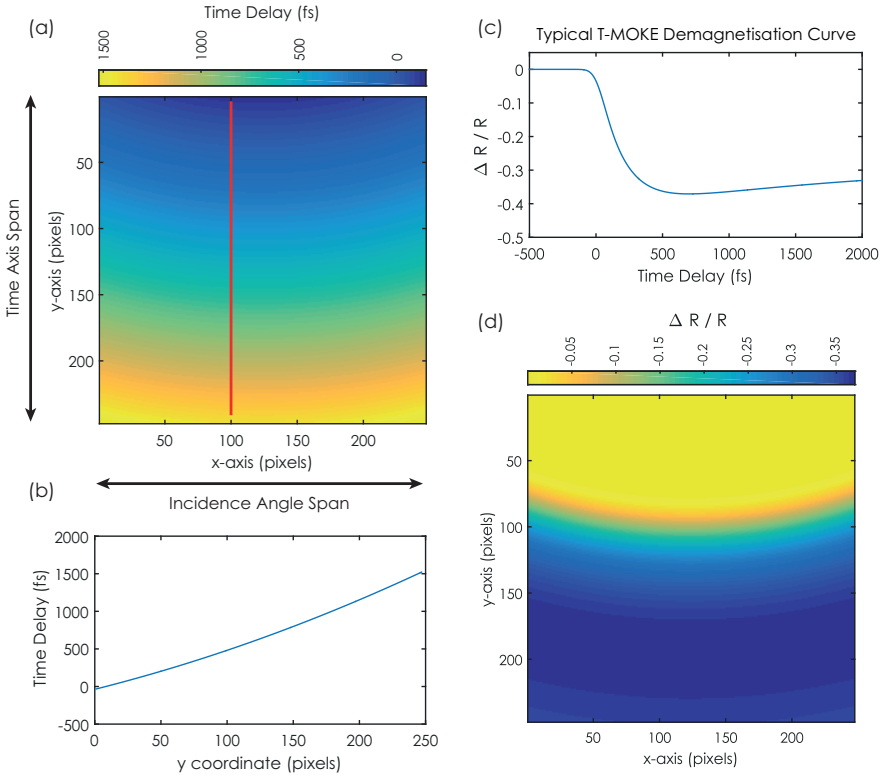

Figure 8.10: (a) Simulated map of the arrival time delay as a function of the pixel coordinates in the image acquired by the reference CCD detector. (b) Line profile taken from the time delay map along the red line. (c) Typical demagnetisation curve for a 3d metal. (d) Simulated image acquired by the reference CCD detector.

8.4.1 From raw images to time-resolved data

As mentioned earlier in section 8.2.6, each pump-probe event produces a set of two images, which are recorded by the reference CCD detector and the reflection CCD detector respectively. In the following I will describe the procedure to recover from the raw CCD images the single-shot pump-probe trace.

Figure 8.11 shows the raw images acquired by the CCD detectors both with the IR pump beam open (pumped) and closed (un-pumped). The effect of the laser-induced demagnetisation becomes clear once each raw image from the reflection CCD is normalised by the corresponding image from the reference CCD and the TR-image is computed (Fig. 8.11c). The comparison of the shape of isochronous lines in figure 8.11c to the one of those in the simulated TR-image shown in figure 8.10d reveals clear differences in the curvature. Such differences in shape can be explained by taking into account slight misalignments of the

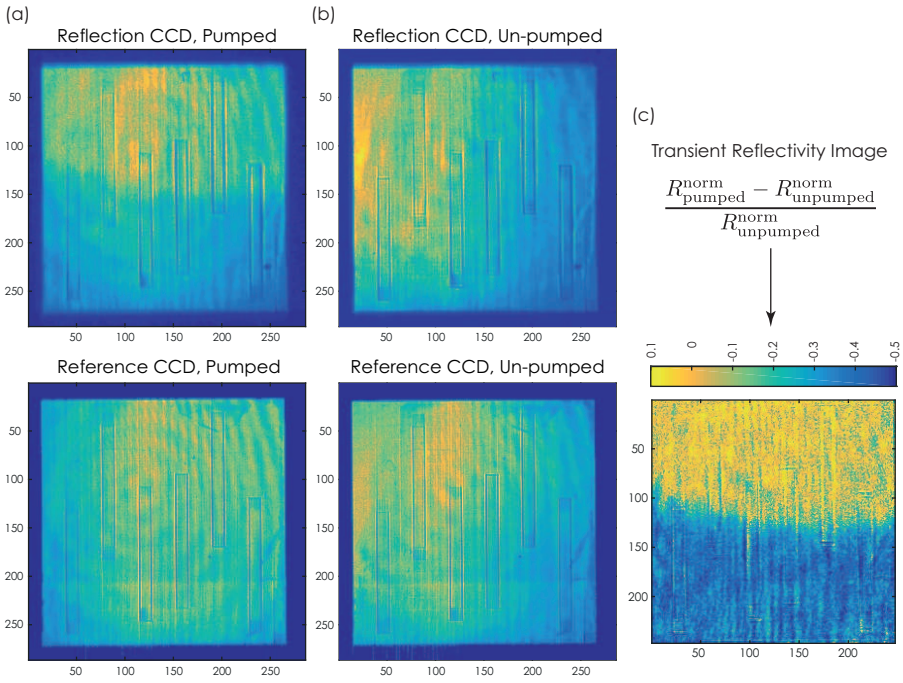

Figure 8.11: (a, b) Raw images from the CCD detectors for the pumped and un-pumped case respectively. (c) TR-image as calculated according to the definition above.

grating with respect to the incoming beam. When the incoming beam and the grating surface are not perpendicular to each other, as shown in figure 8.12a, additional time delays can be created due to differences in path length between the two outermost rays of the incoming beam. To reconstruct the time delay map of the experiment, the simulation of the TR-image is repeated for different values of the zone plate pitch and yaw angles until a satisfying agreement between the simulated TR-image and the measured TR-image is achieved. It was found that a 0.6° pitch and 0.3° yaw angle gives a good agreement (Fig. 8.12b,c).

After identifying the time delay window common to each column in the measured TR-image (red lines in figure 8.12b), the calculated time delay map is used to interpolate the measured TR-image and create the final TR-image in which the time delay varies linearly in the y-coordinate. It can be observed that due to the linear relation between the pixel coordinate and the time delay the isochronous line is now straight. Based on the time delay map simulation, the total time span along the final TR-image (termed unwarped TR-image in the following) is 1.47 ps leading to a calibration constant of $\approx$ 6 fs/pixel.

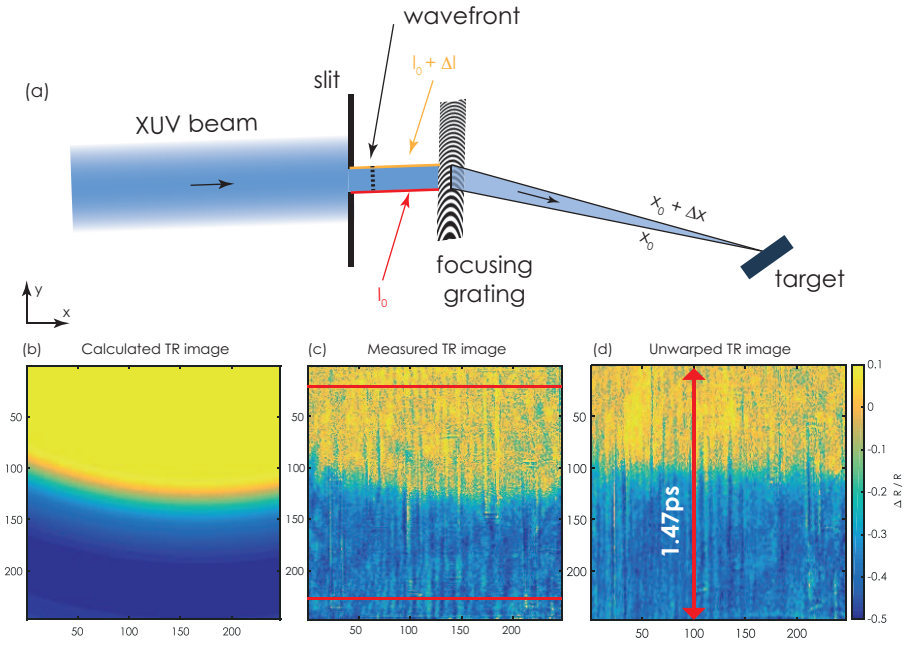

Figure 8.12: (a) Schematic showing how additional delay is created when the grating is not perfectly aligned with the incoming beam. (b) Simulated TR-image with 0.6° pitch and 0.3° yaw angles. (c) Measured TR-image. (d) Final TR-image in which the time delay varies only in the y-coordinate.

8.4.2 Accuracy of the time window calibration

To determine the accuracy with which the calibration constant was determined, we acquired a set of TR-images scanning the XUV-IR time delay in steps of 150 fs around the time overlap and tracked the movement of the time overlap isochronous line in the unwarped TR-image. To mitigate the effects of the XUV to IR laser jitter, the data was sorted according to the time stamp data generated by the beam arrival monitor BAM2 (see appendix A). The measured time window total width was 1500 ± 100 fs leading to a calibration constant value of 6±0.4 fs/pixel, which is in good agreement with the value obtained by the ray optics calculation.

8.4.3 Single shot measurements on cobalt continuous layers

To investigate the role of eventual non reproducible processes in ultrafast demagnetisation we acquired a series of 200 single-shot real-time measurements on a 20 nm thick cobalt film at an IR pump fluence $\mathfrak{F}$ =12 mJ cm^{-2}. All the measurements were performed in an applied magnetic field of 60 mT. For each pump-probe event a time resolved reflectivity curve was obtained from the unwarped TR-image by averaging through the x-

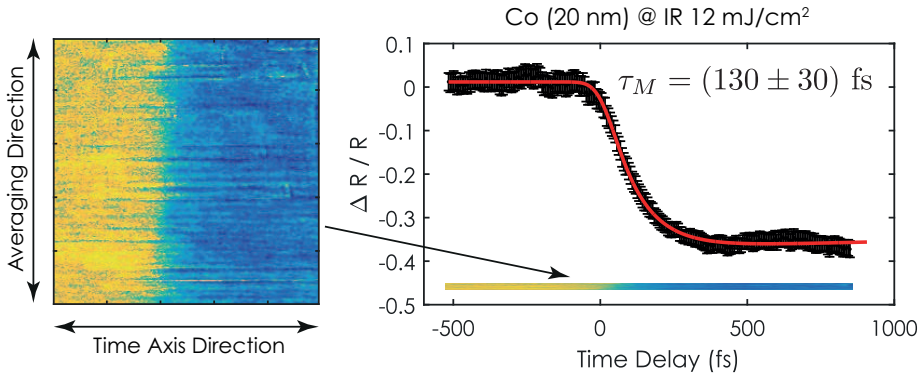

Figure 8.13: Typical agreement of the measured demagnetisation curve with the fitting using a double exponential decay phenomenological model.

coordinate as shown in figure 8.13.

To gain further insight, each time resolved trace was fitted with a double exponential decay phenomenological model and the demagnetisation time was extracted. The model used for fitting is:

$$\frac{\Delta R(t)}{R_0} = G(t) * \Theta(t)\left[A\left(1-e^{-\frac{t}{\tau_M}}\right)+B\left(1-e^{-\frac{t}{\tau_r}}\right)\right]+C \tag{8.8}$$

where G(t) is a gaussian function with a full width half maximum of 90 fs to account for the time resolution of the experiment, $\Theta(t)$ is the Heaviside function, τ_M and τ_r are the time constants related respectively to the ultrafast drop of the magnetisation and its subsequent relaxation process. A, B, and C are constants. The width of the time window probed in our measurements is too narrow to obtain a proper fitting of the recovery time constant τ_r. For this reason its value has been set to 5000 fs in accordance to literature measurements [12] and only the parameters A, B, C, and τ_M have been extracted from the fitting to the experimental data. Figure 8.13 shows the typical agreement of one of the 200 time resolved traces with the fitting according to this model.

Figure 8.14 shows the comparison of 16 subsequent single pump-probe events. No significant changes are observed between the different pump-probe events. For a more quantitative analysis we can consider the statistical distribution of the demagnetisation time τ_M, obtained by fitting 200 single-shot real-time measurements (Fig. 8.15). As described in chapter 3 the mechanisms for ultrafast demagnetisation are still not completely understood, and one could speculate the existence of two or more demagnetisation paths having different time constants that are stochastically chosen by the system in different pump-probe events. This would generate a distribution of demagnetisation times peaking at more than one value. Our measurements show that the distribution of the measured

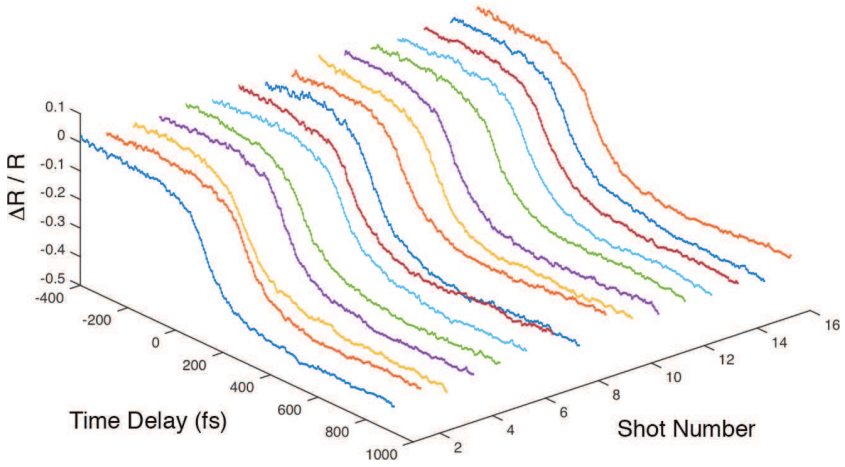

Figure 8.14: Comparison of 16 subsequent real time measurements of the first 900 femtoseconds of the ultrafast demagnetisation process of a continuous 20 nm thick cobalt film at a fluence of 12 mJ cm^{-2}.

demagnetisation time is centred along a single value and allow us to exclude, within our time resolution of 90 fs, the presence of more than one competing path. This result constitutes a direct proof that ultrafast demagnetisation can be explained taking into account only reproducible dynamics as discussed previously in chapter 3, confirming the soundness of the models employed so far. The distribution of the experimental values for τ_M can be fitted with a Gaussian curve leading to an average demagnetisation time value of 130 ± 30 fs which is in good agreement with what is reported in literature for cobalt continuous layers (see table 3.1 in chapter 3).

8.4.4 Preliminary measurements on Co/Ni multilayers

In the following we present preliminary measurements that were performed on [Co (0.2 nm) / Ni (0.2 nm)]$_{20}$ multilayers. Although these multilayer systems normally show perpendicular magnetic anisotropy, at this thickness ratio the magnetisation is in-plane and the system can be probed using resonant T-MOKE. The particular interest in studying systems with more than one magnetic component is that the coupling mechanism between the different constituents can lead to more complex dynamics. The measurements presented here are acquired at the Ni $M_{2,3}$ edge. Since the Curie temperature of Co/Ni multilayers ($\approx$ 900K) is significantly lower than the one of pure cobalt ($\approx$ 1400K), it is important to make sure that the XUV probe pulse does not modify the magnetisation state of the sample. For this reason we have acquired different T-MOKE images at different XUV intensities with no IR pump.

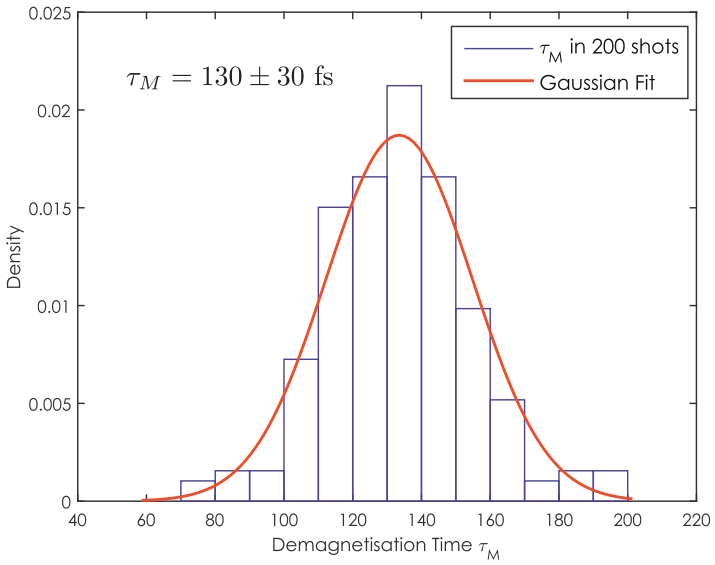

Figure 8.15: Statistical distribution of the demagnetisation time of a 20 nm thick cobalt film.

Figure 8.16 shows three line profiles extracted from T-MOKE images for three different XUV intensities varying from 2.2×10^9 W cm^{-2} to 1.4×10^{11} W cm^{-2}. As the T-MOKE signal is proportional to the magnetisation, the line profiles are a real time measurement of the sample magnetisation. Firstly, we can observe that the T-MOKE asymmetry at $t = 0$ decreases with increasing fluence of the incoming XUV pulse, suggesting that XUV induced demagnetisation effects are present. Furthermore the T-MOKE asymmetry decreases steadily with time in all three traces, indicating that XUV induced effects are still present even at the lowest possible XUV fluence.

All the attenuators available at the beamline were used to achieve the highest possible attenuation of the FEL beam. In order to decrease the XUV fluence further the only remaining option was to move the sample out of the zone plate focus. However, ray optics simulations showed that when the sample surface is out of the zone plate focus, the bandwidth of the incoming XUV beam induces too strong a degradation of the temporal resolution. Furthermore, due to the very weak reflectivity of the sample measured in this experiment, at 2.2×10^9 W cm^{-2} the signal to noise ratio on the reflection CCD was too weak to perform single-shot measurements of ultrafast demagnetisation. Figure 8.17 shows a measurement performed averaging over 10 consecutive pump-probe events. The line profile from the T-MOKE image is a combination of a constant slope, visible in the part before the time overlap due the effect of the XUV pulse, and an exponential decay due to the ultrafast quenching of the magnetisation induced by the IR pulse. For a complete under-

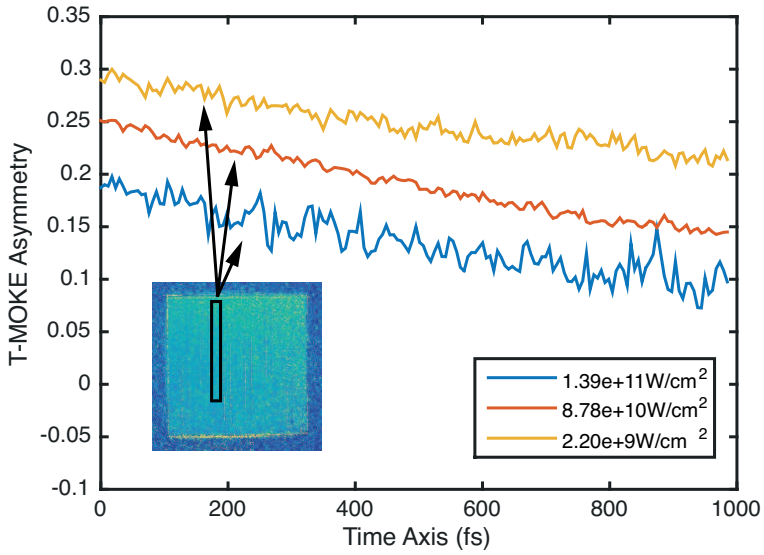

Figure 8.16: T-MOKE asymmetry time evolution without infrared pumping. The three line scans are acquired at three different x-ray intensities varying from 2.2×10^9 W cm^{-2} to 1.4×10^{11} W cm^{-2}. The inset shows one of the three T-MOKE images from which the time traces are extracted.

standing of the observed behaviour one could think of integrating numerically the three coupled differential equations of the three temperature model (see chapter 3) in the presence of two external excitations: a first one caused by the IR pulse, and a second, more complex one caused XUV pulse with a tilted pulse front.

8.5 Conclusions

In this chapter we have presented a novel experimental set-up that enables the real-time measurement of the transient XUV reflectivity of a sample with sub-100fs time resolution. Typically, spatial encoding techniques in the XUV regime allow for probing a total time period of less than 500 fs. By employing an off-axis Fresnel zone plate, we give the first experimental proof of spatial encoding over a time window of 1500 fs.

We have successfully applied this set-up to measure in real time the early time period of the ultrafast demagnetisation of a cobalt thin layer. The measurement correlates well with what reported previously in literature for cobalt films confirming the high time resolution of our technique. By analysing the statistical distribution of the demagnetisation time obtained from 200 subsequent pump-probe events, we have proven that no stochastic contributions are present in the early time period of the demagnetisation process. In the case of Co/Ni multilayers even the lowest achievable XUV fluence was high enough to alter

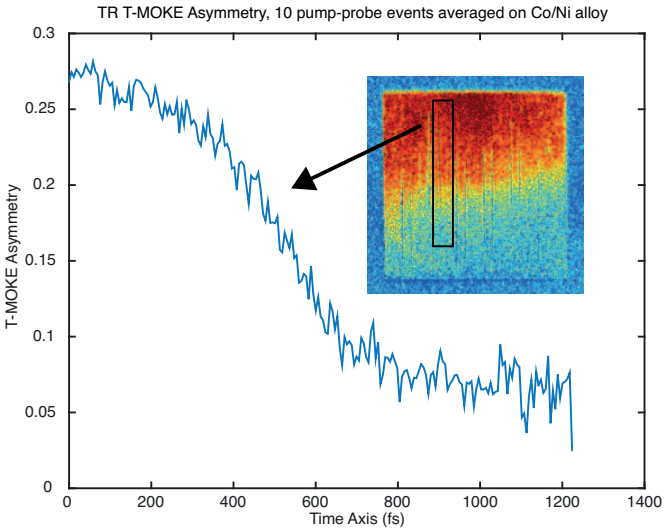

Figure 8.17: T-MOKE image and corresponding line profile acquired using 10 pump-probe events at the lowest possible XUV fluence of 2.2×10^9 W cm^{-2} with IR pumping at 12 mJ cm^{-2}.

the sample magnetisation state making it particularly difficult to disentangle the separate contributions of the XUV pulse and of the IR pulse to the demagnetisation process.

In future, one could think of a different set-up where the XUV fluence is significantly reduced by the use of a line focusing zone plate, and the spatial encoding is achieved by tilting the infrared pump pulse front with a plane grating. The use of a plane grating in the pump beam would also have the advantage of extending the available time window up to a few tens of picosecond.

References

[1] S. Mathias, C. La-O-Vorakiat, P. Grychtol, P. Granitzka, E. Turgut, J. M. Shaw, R. Adam, H. T. Nembach, M. E. Siemens, S. Eich, C. M. Schneider, T. J. Silva, M. Aeschlimann, M. M. Murnane, and H. C. Kapteyn. Probing the timescale of the exchange interaction in a ferromagnetic alloy. *Proceedings of the National Academy of Sciences*, 109(13): 4792–4797, 2012.

[2] I. Radu, K. Vahaplar, C. Stamm, T. Kachel, N. Pontius, H. A. Durr, T. A. Ostler, J. Barker, R. F. L. Evans, R. W. Chantrell, A. Tsukamoto, A. Itoh, A. Kirilyuk, Th. Rasing, and A. V. Kimel. Transient ferromagnetic-like state mediating ultrafast reversal of antiferromagnetically coupled spins. *Nature*, 472(7342):205–208, 2011.

[3] S. Mangin, M. Gottwald, C-H. Lambert, D. Steil, V. Uhlíř, L. Pang, M. Hehn, S. Aleb-

rand, M. Cinchetti, G. Malinowski, Y. Fainman, M. Aeschlimann, and E. E. Fullerton. Engineered materials for all-optical helicity-dependent magnetic switching. *Nat. Mater.*, 13(3):286–292, 2014.

[4] C-H. Lambert, S. Mangin, B. S. D. Ch. S. Varaprasad, Y. K. Takahashi, M. Hehn, M. Cinchetti, G. Malinowski, K. Hono, Y. Fainman, M. Aeschlimann, and E. E. Fullerton. All-optical control of ferromagnetic thin films and nanostructures. *Science*, 345 (6202):1337–1340, 2014.

[5] P. R. Poulin and K. A. Nelson. Irreversible organic crystalline chemistry monitored in real time. *Science*, 313(5794):1756–1760, 2006.

[6] John T. F., Lisa D., Keith A. N., and Rick T. Spatially encoded, single-shot ultrafast spectroscopies. *J. Opt. Soc. Am. B*, 12(1):155–165, 1995.

[7] S. Mathias, C. La o vorakiat, J. M. Shaw, E. Turgut, P. Grychtol, R. Adam, D. Rudolf, H. T. Nembach, T. J. Silva, M. Aeschlimann, C. M. Schneider, H. C. Kapteyn, and M. M. Murnane. Ultrafast element-specific magnetization dynamics of complex magnetic materials on a table-top. *Journal of Electron Spectroscopy and Related Phenomena*, 189(0):164 – 170, 2013.

[8] U. Tiwari, R. Ghosh, and P. Sen. Theory of magneto-optic kerr effects. *Phys. Rev. B*, 49: 2159–2162, 1994.

[9] H. Höchst, D. Rioux, D. Zhao, and D. L. Huber. Magnetic linear dichroism effects in reflection spectroscopy: A case study at the Fe $m_{2,3}$ edge. *Journal of Applied Physics*, 81(11):7584–7588, 1997.

[10] P. M. Oppeneer. *Magneto-optical kerr spectra*, volume 13 of *Handbook of Magnetic Materials*, chapter 3, pages 229 – 422. Elsevier, 2001.

[11] B. L. Henke, E. M. Gullikson, and J. C. Davis. X-ray interactions: Photoabsorption, scattering, transmission, and reflection at e = 50-30,000 ev, z = 1-92. *Atomic Data and Nuclear Data Tables*, 54(2):181–342, 1993.

[12] B. Vodungbo, J. Gautier, G. Lambert, A. B. Sardinha, M. Lozano, S. Sebban, M. Ducousso, W. Boutu, K. Li, B. Tudu, M. Tortarolo, R. Hawaldar, R. Delaunay, V. López-Flores, J. Arabski, C. Boeglin, H. Merdji, P. Zeitoun, and J. Lüning. Laser-induced ultrafast demagnetization in the presence of a nanoscale magnetic domain network. *Nat. Commun.*, 3:999, 2012.

Summary and Outlook

In the last twenty years the continuously increasing demand for storing information has encouraged researchers to look for novel and more effective solutions to achieve higher storage densities, higher speed and lower power consumption. Manipulating magnetisation by exploiting magnetoelectric coupling is expected to lead to memory devices with significantly lower power consumption. Similarly, laser-induced magnetisation processes are expected to improve the speed at which information is manipulated by up to two orders of magnitude. The work presented in this thesis delivered new insights into the magnetoelectric coupling in strain mediated artificial multiferroics, and into laser-induced magnetisation processes in ferromagnetic and ferrimagnetic materials. The results can be divided in two parts. The work presented in chapter 6 and 7 focuses on the observation of magnetisation switching under electric field and laser stimuli. The work presented in chapter 8 focuses more on the ultimate mechanisms that govern the interaction of magnetic materials with laser pulses.

In the experiments described in chapter 6 we have investigated magnetoelectric coupling in Ni nanopatterned islands deposited on a PMN-PT ferroelectric single crystal. Our results constitute the first experimental proof of a 90° uniform magnetisation rotation by the application of an electric field. Since the rotation of the magnetisation is complete, the corresponding magnetoelectric coupling coefficient is among of the highest measured so far. We have found that the multidomain structure of the ferroelectric single crystal leads to a complex strain-mediated magnetoelectric coupling. This suggests that realising the full magnetoelectric stack at the nanoscale, in order to achieve a single domain configuration in the ferroelectric as well as in the ferromagnet, is of primary importance not only to fulfil large scale integration requirements but also to achieve a reliable magnetisation manipulation by an electric field. The observed electric field induced reorientation is related to the strain generated in the ferroelectric as the polarisation switches, and therefore the ultimate speed of the observed magnetisation reorientation process is limited by the propagation of ferroelectric domain walls which is significantly slower than ferromagnetic

switching. It would be interesting to employ the ferroelectric in its linear piezoelectric regime (i.e. without triggering a ferroelectric polarisation switching) to generate short strain pulses that could induce precessional switching in a properly tailored ferromagnetic nanostructure.

In chapter 7 we have investigated laser induced magnetisation switching in nanopatterned GdFeCo nanostructures. Heat pulse induced switching was observed in nanostructures at different length scales down to a 200 nm out-of-plane domain located in the centre of a 400 nm wide nanostructure. Due to the structuring process, all nanostructures had in-plane edge domains that are found to play no particular role in the efficiency of the switching thanks to the strength of the driving force by which the switching occurs. Shrinking the size of the switched area to below the diffraction limit of the laser beam triggering the switching is one of the main challenges for laser induced magnetisation switching. Indeed, it would be of great interest for future studies to verify the reliability of the switching down to areas of few tens of nanometers with the use of near field enhancement nanoantennas.

In chapter 8 we presented a novel experimental set-up that allows one to obtain a real time measurement of the transient magnetisation state induced by the excitation of the magnetic sample with an ultrashort infrared (IR) pulse. Our approach relies on ultrashort extreme ultraviolet (XUV) pulses from the free electron laser FLASH and an off-axis Fresnel zone plate to obtain a spatial encoding of the XUV-IR delay over a time window of 1500 fs. Using a single pump-probe event, we succeeded in capturing the ultrafast demagnetisation process of a cobalt thin layer with a time resolution comparable to laser based repetitive pump-probe experiments. The analysis of the statistical distribution of the demagnetisation time obtained from subsequent shots, suggests that no stochastic contribution are present in the early time period of the demagnetisation process. In the case of the measurements performed with Co/Ni multilayers, the XUV fluence of the probe beam was high enough to alter the sample magnetisation state even with the lowest possible XUV intensity. In future, one could think of different set-ups where spatial encoding is achieved not by tilting the time front of the XUV pulse but by tilting the IR pump pulse front with a plane grating. This would allow on one hand to significantly reduce the XUV fluence by positioning the sample out of focus and on the other hand to extend the available time window up to a few tens of picosecond.

The results presented in this thesis stress the importance of further investigating magnetisation processes at nanometer length scales and in femtosecond time scales. Although this two aspects may seems apparently unrelated, the velocity of electrons in an itinerant ferromagnet is approximately 1 nm/fs. In this regard, further novel and exciting results are expected from experiments combining reciprocal space imaging with ultrashort pulses from free electron lasers in the soft x-ray regime.

APPENDIX A

Generation of ultrashort XUV pulses at FLASH

The $M_{2,3}$ resonances of 3d transition metals fall in the XUV energy range. To measure laser induced ultrafast demagnetisation employing resonantly enhanced T-MOKE, one needs ultrashort pulses in the XUV energy range. The generation of light pulses having a centre wavelength of 120 nm to 10 nm, cannot be achieved with the traditional solid state laser technology where an active medium is pumped by an external source. At this wavelengths, no active medium has low enough absorption to sustain lasing and also there are no available mirrors having a high enough reflectivity to create a multi pass optical resonator.[1]

X-ray free electron lasers (X-FEL) are large scale facilities that circumvent these problems. In a X-FEL both the lasing medium and the pump source are substituted with a relativistic electron beam. Similarly to what happens in synchrotrons, light is generated by letting a relativistic electron beam travel through an undulator. In an undulator a periodic array of magnets creates a sinusoidal magnetic field in order to make an electron beam move in a sinusoidal pattern. When an electron beam travels through the undulator it starts oscillating as well as emitting light, identified as spontaneous undulator radiation, with a centre wavelength λ_0 defined as:

$$\lambda_0 = \frac{\lambda_u}{2\gamma^2}\left(1 + \frac{e^2 B_0^2 \lambda_u^2}{8\pi^2 m_0^2 c^2}\right) \tag{A.1}$$

where $\gamma = E/m_0c^2$, λ_u is the undulator period, B_0 is the peak magnetic field in the undu-

[1] This section follows the description given in: [1]

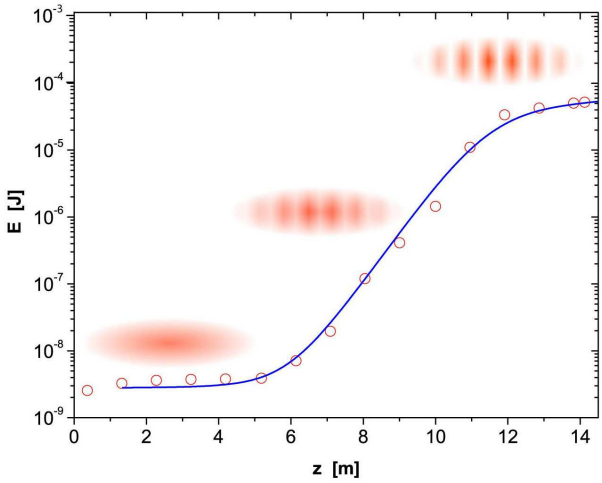

Figure A.1: Typical X-FEL pulse energy behaviour as a function of the length traveled in the undulator. Reprinted from [1].

lator, e the electron charge, c the speed of light and m_0 the electron rest mass [2].

X-FELs produce light pulses which are several orders of magnitude stronger than those produced at synchrotrons because most of the electrons radiate coherently. Please note that not only the pulses are stronger but their duration is normally below 100 fs, significantly shorter than what is produced at storage rings and well suited for studying ultrafast phenomena with high time resolution.

Lasing in X-FELs happens thanks to the SASE process, i.e. an amplification of the spontaneous radiation generated in the first part of the undulator. When the undulator is sufficiently long and the bunch peak current sufficiently high, electrons can lose their energy by producing undulator radiation as well as efficiently gaining energy from the undulator radiation. However, the electrons that have lost energy will oscillate on a different trajectory than those that have gained energy from the photon field and a longitudinal modulation of the electron beam velocity is generated. As a result, the electrons in the bunch start to organise in micro-bunches that are shorter than the wavelength λ_0 and start to emit coherent radiation. The increase in the photon field when the micro-bunching starts, favours it even further producing an exponential growth of the pulse energy in the undulator, leading to lasing. To sustain efficiently the SASE process the peak current of the electron bunch must be very high, in the order of several kA. This is normally achieved by compressing the relativistic electron bunches to sub-100fs duration. As a result the XUV pulse generated in the undulator also has a sub-100fs duration.

Figure A.1 shows the typical energy profile of a pulse propagating inside an X-FEL undulator. In the first part of the undulator the energy is constant and only spontaneous

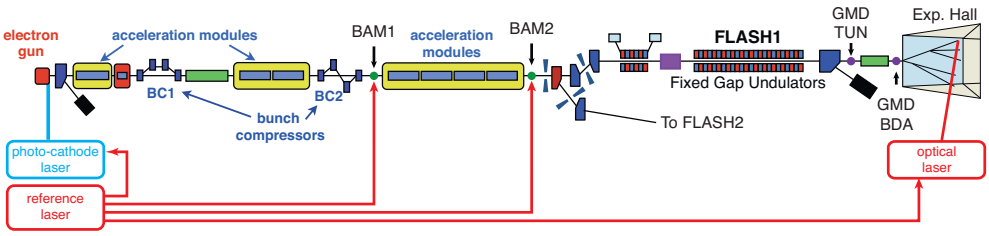

Figure A.2: Schematic of the free electron laser FLASH. Adapted from [3].

undulator radiation is produced. At a certain length the photon field is strong enough to induce micro-bunching and the pulse energy starts to grow exponentially. When no electrons from the original bunch are left, it is not possible to increase the population of the micro-bunches further and the pulse energy of the X-FEL stays constant.

Figure A.2 shows a schematic of the X-FEL FLASH in Hamburg. An electron bunch with an integrated charge varying between 0.1 nC to 0.5 nC is generated in the electron gun using a 10 ps UV laser pulse focused onto a photo-cathode. The electrons are then accelerated in the acceleration modules up to an energy of 1.25 GeV. After two compression chicanes (BC1 and BC2) the beam travels through the undulator. The undulator at FLASH-1 is 27 m long, with a period $\lambda_u = 27.3$ mm and has a fixed gap generating a peak magnetic field $B_0 = 0.48$ T [3]. After the undulator, the XUV radiation travels to the experimental hall and the dipole magnet deflects the electron beam to a beam dump, generating dipole radiation which is used for diagnostic purposes.

It is important to note that the high peak current needed for the X-FEL operation cannot be achieved directly at the photocathode using UV pulses with femtosecond duration. The charge density in the electron bunch would be too high and space charge forces would destroy the bunch profile. Therefore, to maintain the quality of the electron bunches, they are created with modest peak currents of ≈ 30 A and are accelerated to relativistic energies as quickly as possible by the first cavity running at 1.3 GHz. At relativistic energies, the reciprocal distance of the electrons in the rest frame is increased and the space charge forces are significantly lowered making it possible to compress the electron bunch to a peak current of few kA.

In order to excite the sample under investigation, at FLASH a Ti:Sapphire amplified laser system (identified as optical laser in figure A.2) delivers infrared pulses at 810 nm centre wavelength with a pulse duration of about 60 fs. The infrared pulses produced by this laser system are synchronised to the free electron laser via a feedback mechanism. As conventional radio frequency (RF) signals do not guarantee femtosecond stability over long distances, at FLASH a low noise optical master clock is synchronised to the 1.3 GHz RF frequency running the first cavity and distributed through the accelerator down to the optical laser hutch via length-stabilised glass fibre links. The optical laser can be phase

locked to the optical master clock with an average jitter smaller than 30 fs RMS [4]. The delay between the IR pump and the XUV probe pulse can be deliberately modified by modifying the optical path of the IR pulse using a retro-reflector based delay line positioned in the optical laser hutch.

The photo-cathode laser that generates the initial electron bunch is also synchronised to the optical master clock. However, fluctuations in the amplitude of the accelerating fields in the first acceleration module can cause fluctuations in the time-of-flight through the first bunch compressor BC1 and, as a result, the time at which the electron bunch reaches the undulator may jitter up to few hundred femtoseconds. To overcome this problem a time-stamping system is implemented based on two beam arrival monitors (BAM1 and BAM2) that measure the arrival time of the electron beam with an accuracy better than 10 fs. For each XUV pulse the timing informations are stored and the data can be time-sorted reducing significantly the effect of the time arrival jitter. More details about how the BAMs are implemented can be found at [5].

As free electron lasers are long accelerators, temperature drifts normally cause drifts in the timing between different parts of the accelerator. The long term drift of the FEL with respect to the optical laser is monitored by means of a commercial streak camera. A small fraction of the optical laser pulse is picked before the delay line and sent to the streak camera as a marker for the arrival time of the IR pulse at the experiment. The time reference for the arrival of the XUV pulse is obtained sending to the streak camera a part of the dipole radiation produced by the electron beam when it is directed to the final beam dump. In this way, long term drifts between the optical laser and the FEL can be quantified with a precision of approximately 50 fs [6].

As the SASE process essentially starts from noise fluctuations, one should expect changes in the intensity and spectral shape of the produced XUV radiation on a pulse to pulse basis. For this reason, additional photon diagnostic tools in the experimental hall operate independently from the experiment and allow to characterise each XUV pulse. Two gas monitor devices, indicated as GMD-TUN and GMD-BDA in figure A.2, allow to measure the pulse intensity as well as the beam position. A variable line spacing spectrometer (VLS) monitors the XUV spectrum of each pulse. More details about how the photon diagnostic works can be found at [7].

References

[1] *FLASH: The Free-Electron Laser in Hamburg*. Deutsches Elektronen-Synchrotron DESY, 2007.

[2] P. Schmüser, M. Dohlus, J. Rossbach, and C. Behrens. *Undulator Radiation*, volume

258 of *Springer Tracts in Modern Physics*, chapter 2, pages 11–23. Springer Berlin Heidelberg, 1 edition, 2014.

[3] P. Schmüser, M. Dohlus, J. Rossbach, and C. Behrens. *The EUV and Soft X-Ray FEL in Hamburg*, volume 258 of *Springer Tracts in Modern Physics*, chapter 8, pages 133–163. Springer Berlin Heidelberg, 1 edition, 2014.

[4] DESY. Timing the Laser and the fel. Website, April 2015.

[5] F. Löhl, V. Arsov, M. Felber, K. Hacker, W. Jalmuzna, B. Lorbeer, F. Ludwig, K.-H. Matthiesen, H. Schlarb, B. Schmidt, P. Schmüser, S. Schulz, J. Szewinski, A. Winter, and J. Zemella. Electron bunch timing with femtosecond precision in a superconducting free-electron laser. *Phys. Rev. Lett.*, 104:144801, 2010.

[6] H. Redlin, A. Al-Shemmary, A. Azima, N. Stojanovic, F. Tavella, I. Will, and S. Düsterer. The FLASH pump–probe laser system: Setup, characterization and optical beamlines. *Nuclear Instruments and Methods in Physics Research Section A: Accelerators, Spectrometers, Detectors and Associated Equipment*, 635(1, Supplement):S88 – S93, 2011.

[7] K Tiedtke, A Azima, N von Bargen, L Bittner, S Bonfigt, S Düsterer, B Faatz, U Frühling, M Gensch, Ch Gerth, N Guerassimova, U Hahn, T Hans, M Hesse, K Honkavaar, U Jastrow, P Juranic, S Kapitzki, B Keitel, T Kracht, M Kuhlmann, W B Li, M Martins, T Núñez, E Plönjes, H Redlin, E L Saldin, E A Schneidmiller, J R Schneider, S Schreiber, N Stojanovic, F Tavella, S Toleikis, R Treusch, H Weigelt, M Wellhöfer, H Wabnitz, M V Yurkov, and J Feldhaus. The soft x-ray free-electron laser FLASH at DESY: beamlines, diagnostics and end-stations. *New Journal of Physics*, 11(2):023029, 2009.

Acknowledgements

I would like to thank all the people that contributed in one way or another to the success of my work as a PhD student in the Microscopy and Magnetism group at the Swiss Light Source. In particular...

...**Frithjof Nolting** for giving me the opportunity of completing a very stimulating PhD project under his direct supervision. Apart from being a great physicist, from whom I learned a lot, he has been a great supervisor, leaving me freedom to explore research in multiferroics and ultrafast science and being always encouraging and supportive.

...**Jan Lüning** for giving me the opportunity of leading the experiment at FLASH, for the long and insightful discussions on Skype, and also for showing me that often you should approach technical problems during experiments with a smile, no matter how bad things are. I'm not sure I'm fully succeeding in this last thing but I'm getting better at it.

...**Christian David** not only for insightful discussions and for introducing me in the world of x-ray diffractive optics, but also for sharing the breath-holding experience of mounting ultra-thin aluminium filters during the first FLASH beamtime.

...**Loïc Le Guyader** not only for sharing his knowledge on how to squeeze the last tens of nanometers of resolution out of the PEEM and for guiding me through the wonders of ultrafast optics, but also for being a friend and a great beamtime companion.

...**Carlos Antonio Fernandes Vaz** for help and advice on numerous things. From valuable insights on sample preparations to proofreading many of my manuscripts (including this thesis).

...**Rajesh Chopdekar** for being a great multiferroic PEEM beamtime companion fighting charging and sample-breaking discharges in the PEEM.

...**Armin Kleibert** for pleasant and provoking discussions on magnetism, magneto-optics and nature of single photon events.

...**Urs Staub** for pleasant and stimulating discussions on multiferroics and ultrafast science.

...**Ludovic Howald** for the help in setting up the experiments at FLASH and the time spent together resuscitating the laser setup at SIM every now and then.

...**Yoav William Windsor and Sebastian Grübel** for being great friends and great colleagues. Yoav, having you as a desk-mate cheered up every moment I spent in the office with cool scientific and non-scientific chats and great writing music. Sebastian, I enjoyed the time we spent in the laser lab where you shared your knowledge in THz generation and EO sampling measurements, and out of the lab when we had fun altogether (I guess I shall call you the grill master from now on!). Also since you two are next in line for defending your PhD, I wish you the best of luck!

...**Mikako Makita** for producing zoneplates with Japanese precision (well...not so Japanese, they still have those horrible stitching errors...isn't it Mikako?), finding out an early mistake that would have made the experiment useless, and being a great X-FEL beamtime companion. On top of this she has been and is a loving and VERY patient partner, who supported/whipped me while writing this thesis. It is also thanks to your help if I succeeded in writing this thesis in less than two months. So THANK YOU!

Lastly, I would like to thank my parents for supporting and understanding my decisions. When I look back, I clearly remember when my dad would bring me to work with him. At his work place I had the chance to learn different programming languages and to work in the summer on few projects that taught me the importance of good planning and scheduling. He keeps an analog electronic lab at home and I should thank him for planting in me the seed of analog electronic design. His knowledge and patience also made me fluent in analog circuit design. Part of the scientific success of the experiments described in this thesis benefitted from what I learned from him. Thanks!

List of publications

1. **M. Buzzi**, M. Makita, L. Howald, A. Kleibert, B. Vodungbo, J. Raabe, N. Jaouen K. Tiedtke, N. Schirmel, H. Redlin, C. David, F. Nolting, and J. Luning, in preparation (2015)

2. **M. Buzzi**, C. A. F. Vaz, J. Raabe, F. Nolting. Electric Field Stimulation Set-up for Photoemission Electron Microscopes. *Rev. Sci. Inst.* **86** 083702 (2015).

3. **M. Buzzi**, R. V. Chopdekar, J. L. Hockel, A. Bur, N. Pilet, P. Warnicke, G. Carman, L. J. Heyderman, and F. Nolting. Single domain spin manipulation by electric fields in strain coupled artificial multiferroic nanostructures. *Phys. Rev. Lett.* **111** 027204 (2013)

4. L. Le Guyader, M. Savoini, S. El Moussaoui, **M. Buzzi**, A. Tsukamoto, A. Itoh, A. Kirilyuk, T. Rasing, A. V. Kimel and F. Nolting. Nanoscale sub-100 picosecond all-optical magnetization switching in GdFeCo nanostructures. *Nature Communications* **6** 5839 (2015)

5. J. Heidler, C. Piamonteze, R. V. Chopdekar, M. A. Uribe-Laverde, A. Alberca, **M. Buzzi**, A. Uldry, B. Delley, C. Bernhard and F. Nolting. Manipulating magnetism in La0.7Sr0.3MnO3 via piezostrain. *Phys. Rev. B* **91** 024406 (2015)

6. C. Mix, S. Finizio, **M. Buzzi**, F. Kronast, F. Nolting, G. Jakob and M. Klaeui. Direct observation of temperature dependent magnetic domain structure of the multiferroic $La_{0.66}Sr_{0.34}MnO_3/BiFeO_3$ bilayer system by x-ray linear dichroism- and x-ray magnetic circular dichroism-photoemission electron microscopy. *J. Appl. Phys.* **115** 193901 (2014)

7. S. Finizio, M. Foerster, **M. Buzzi**, B. Krueger, M. Jourdan, C. A. F. Vaz, J. Hockel, T. Miyawaki, A. Tkach, S. Valencia, F. Kronast, G. P. Carman, F. Nolting and M. Klaeui.

Magnetic Anisotropy Engineering in Thin Film Ni Nanostructures by Magnetoelastic Coupling. *Phys. Rev. Applied* **1** 021001 (2014)

8. J. Girovsky, **M. Buzzi**, C. Waeckerlin, D. Siewert, J. Nowakowski, P. M. Oppeneer, F. Nolting, T. A. Jung, N. Ballav and A. Kleibert. Chemically Sensitive Imaging of Magneto-Chemical Molecule-Surface Interactions by X-ray Photo-Emission Electron Microscopy *Chem. Commun.*, 2014 **50** 5190 (2014)

9. S. Finizio, M. Foerster, C. A. F. Vaz, C. Mix, M. Mawass, A. Tkach, M. Klaeui, **M. Buzzi**, F. Nolting, T. Miyawaki, J. Hockel, G. P. Carman, S. Valencia, and F. Kronast. Electrical-field control of magnetism mediated by strain in Ni nanostructures fabricated on pre-poled PMN-PT(011). *SPIN* **3:1340008** (2013)

10. G. Porcari, **M. Buzzi**, F. Cugini, R. Pellicelli, C. Pernechele and M. Solzi. Direct magnetocaloric characterization and simulation of thermomagnetic cycles. *Rev. Sci. Instr.* **84** 073907 (2013)

11. C. A. F. Vaz, C. Moutafis, **M. Buzzi**, and J. Raabe. X-ray excited optical luminescence of metal oxide single crystals. *J. Electron Spectrosc. and Rel. Phenom.* **189** 1 (2013)

12. S. O. Mariager, L. Le Guyader, **M. Buzzi**, G. Ingold, C. Quitmann, Imaging the antiferromagnetic to ferromagnetic first order phase transition of FeRh. arXiv:1301.4164 (2012)

13. G. Porcari, F. Cugini, S. Fabbrici, C. Pernechele, F. Albertini, **M. Buzzi**, M. Mangia, and M. Solzi. Convergence of direct and indirect methods in the magnetocaloric study of first order transformations: The case of Ni-Co-Mn-Ga Heusler alloys, *Phys. Rev. B* **86** 104432 (2012)

14. L. Le Guyader, A. Kleibert, A. Fraile Rodríguez, S. El Moussaoui, A. Balan, **M. Buzzi**, J. Raabe, and F. Nolting. Studying nanomagnets and magnetic heterostructures with X-ray PEEM at the Swiss Light Source, *J. Electron Spectrosc. Relat. Phenom.* **105(10)** 371-380 (2012)

15. L. Le Guyader, S. El Moussaoui, **M. Buzzi**, R. V. Chopdekar, L. J. Heyderman, A. Tsukamoto, A. Itoh, A. Kirilyuk, Th. Rasing, A. V. Kimel, and F. Nolting. Demonstration of laser induced magnetization reversal in GdFeCo nanostructures, *Appl. Phys. Lett.* **101** 022410 (2012)

16. G. Porcari, S. Fabbrici, C. Pernechele, F. Albertini, **M. Buzzi**, A. Paoluzi, J. Kamarad, Z. Arnold, and M. Solzi. Reverse magnetostructural transformation and adiabatic temperature change in Co- and In-substituted Ni-Mn-Ga alloys, *Phys. Rev. B* **85** 024414 (2012)

17. F. Mezzadri, G. Calestani, C. Pernechele, M. Solzi, G. Spina, L. Cianchi, F. Del Giallo, M. Lantieri, **M. Buzzi**, and E. Gilioli. Magnetic and Mössbauer characterization of the multiferroic fluoride $K_3Fe_5F_{15}$, *Phys. Rev. B* **84** 104418 (2011)

18. F. Mezzadri, **M. Buzzi**, C. Pernechele, G. Calestani, M. Solzi, A. Migliori, and E. Gilioli. Polymorphism and Multiferroicity in $BiMn_7O_{12}$, *Chem. Mater.* **2011** 23(16) 3628 (2011)